Study of Density Fluctuations and Particle Transport at the Edge of I-Mode Plasmas

by

Arturo Dominguez

Submitted to the Department of Physics
in partial fulfillment of the requirements for the degree of

Doctor of Philosophy

at the

MASSACHUSETTS INSTITUTE OF TECHNOLOGY

July 2012

Author .....
Department of Physics
July 25, 2012

Certified by .....
Earl S. Marmar
Senior Scientist
Thesis Supervisor

Accepted by .....
Krishna Rajagopal
Professor of Physics, Associate Department Head for Education

Study of Density Fluctuations and Particle Transport at the Edge of I-Mode Plasmas

by

Arturo Dominguez

Submitted to the Department of Physics
on July 25, 2012, in partial fulfillment of the
requirements for the degree of
Doctor of Philosophy

Abstract

The wide range of plasma parameters available on Alcator C-Mod has led to the accessibility of many regimes of operation. Since its commissioning, C-Mod has accessed the Linear ohmic confinement, Saturated ohmic confinement, L-Mode and ELM-free, ELMy and Enhanced D_α H-Mode regimes. Recently, another novel regime, the I-Mode, has been identified[1][2][3][4]. I-modes feature the presence of steep H-Mode-like electron and ion temperature gradients at the edge of the plasma with L-Mode-like density profiles. The I-Mode, in contrast to the H-mode, shows very weak degradation of energy confinement with increased input power, and routinely reaches $H_{98} > 1$ while operating at low edge collisionalities ($\nu^*_{ped} \sim 0.1$), making it a good candidate for reactor relevant tokamaks. Also relevant for reactors, this regime can be sustained in steady state for more than $\sim$15 energy confinement times without the need for ELMs to regulate particle and impurity confinement. Changes in edge density, temperature and magnetic field fluctuations accompany the L-mode to I-mode transition, with reduction of fluctuations in the 50-150kHz range as well as the appearance of a Weakly Coherent Mode (WCM) in the 200-300kHz range, analogous to the Quasi-Coherent Mode (QCM) characteristic of the Enhanced D_α H-mode. Previous work[4] has established a connection between the midrange fluctuation suppression and reduction in the effective thermal diffusivity, χ_{eff}, in the pedestal region. The mechanism in I-mode for maintaining sufficient particle transport to avoid impurity accumulation and instabilities has been unclear. The O-mode reflectometry system has been extensively used for the characterization and detection of the I-mode and the WCM, in part, enhanced by upgrades to the system which enabled the baseband detection of density fluctuations at an array of cutoff locations at the edge of the plasma[5][6][7]. Using a novel model, the autopower signals of reflectometry channels detecting the density fluctuations have been decomposed into a broadband component and a WCM component. The latter is then used to estimate the intensity of the WCM. In parallel, the particle transport across the LCFS in I-mode plasmas has been estimated using a volume integrated particle transport model, where ionization source measurements are acquired using D_α profiles measured near the outboard midplane. This model

takes into account the anisotropic ionization source density around the periphery of the plasma by introducing an asymmetry factor, σ, which is then estimated using a study of I-Mode to H-Mode transitions. The results imply that measurements at the outboard midplane overestimate the surface-averaged influx. Finally, a comparison has been made between the particle flux across the LCFS of the I-mode and the intensity of the WCM, which shows a generally positive correlation between the two. This is supporting evidence that the WCM is, in fact, responsible for maintaining particle and impurity transport across the edge of the I-mode energy transport barrier.

Thesis Supervisor: Earl S. Marmar
Title: Senior Scientist

Acknowledgments

Last month, President Obama made a *gaffe* when he was talking about people starting their own businesses. He said that they don't do it alone, that they need the help of many people. He said *"If you start a business...you didn't build that."*
Now, I agree with his opponent, Mitt Romney: I wrote my thesis alone, without anybody's help?[1]
Well, other than...
My advisor, Earl Marmar. As the director of the C-Mod program, Earl has a million things on his plate, yet that never stopped me from being at his door almost every day, especially in this last year; and he's been constantly there for me, giving me the support I've needed to get to this point I'm at now. His door has always been open to my incessant questions, which always seem to arrive in bulk and close to a deadline; and he always opens up some time in his packed schedule to show me where I'm right and where I've gone wrong, but to always show me the way forward. During these last few months, he's been marching side by side next to me, giving me his valuable feedback on both, the thesis research and the dissertation, even, once, through iPhone pictures from Vermont. Thanks Earl, for everything.
Gerrit Kramer, who's taught me about 5 times more than what I currently know about reflectometry, thanks for picking up the phone all of those countless times that I've called you to talk about the research. You've been there, always available, for the last 8 years, and don't think it's over, you've still got lots to teach me, and I'll make sure you do ;)
Nils Basse, the man who got me going in the research and who first suggested the upgrade that ultimately led to my dissertation. We shared too few moments here, but in the few months we did share, you really put me on the right track. Thanks.
To the thesis readers, Miklos Porkolab and Rick Temkin, thank you for your help in this process. Knowing that you will be two of the few people that will actually read this document in its entirety, I hope it wasn't too boring of a read.

[1] `http://en.wikipedia.org/wiki/Irony_mark#Irony_mark`

Other than Earl and Gerrit, I'd really like to give a special "thank you" to: Jim Terry, Brian LaBombard, Amanda Hubbard, Anne White, Jerry Hughes and Martin Greenwald for all of the help you've given me in all stages of this research. I'd hate to calculate how many hours I've spent just trying to extract every ounce of knowledge from your all-you-can-eat-Indian-style-buffet brains. And, what's more, you always had time (or made time) for my endless questions.

As a rule of thumb, if you're a scientist at the PSFC, I've gone looking for you at some point: Dennis Whyte, Ron Parker, Paul Bonoli, Bruce Lipschultz, John Rice, Ian Hutchinson, Steve Wolfe, Peter Catto, Abhay Ram, Darin Ernst, Catherine Fiore, Jim Irby, Jan Egedal, Jeff Freidberg, Peter Koert, Atma Kanojia, Yijun Lin, Luis Delgado-Aparicio, Bob Granetz, Steve Scott, Syun'ichi Shiraiwa...I've been lucky to study in a place with so many great minds, and friendly people.

To my fellow PSFC grad students, most of which are now distinguished doctors: The ones that saw my PSFC infancy: Brock, Noah, Liang, Eric, Jason, Andrea, Rachael, Aaron, Matt, Kenny, Balint, Will, Matt, Antoine and Greg. You guys have seen the growth (mostly horizontal) of this Colombian and I hope our paths will intertwine like a fancy horse's tail.

Then there's Nathan and Istvan with whom I shared many a-mini basketball (maybe too many). You two will unfortunately have to hear much more from me after I graduate. Then my rock-outs with Matt which kept me going even in the late night sessions (especially those of the never-ending work hours of Matt), and in this last year, sharing an office with the ever angry and bad-tempered Seung Gyou, "The Fury of Korea"?. Thanks for putting up with me as an officemate...you all have racked up some serious karma points.

To the later grads: Mario, Dan, Nareg, Bob, Geoff, Mike, Dan, Miguelito, Chi, John Walk, Yunxing, Peng, Jungpyo, Naoto, Cornwall, Choongki, Peng, Jen, Yuri, Zach, Orso, Mark, Fautian, Danny, Christian, Ralph, Roman, Evan (plus all that I can't think of right now), you guys are an impressive generation of scientists and I definitely hope I don't have to compete with you for a job...cause I'll be in trouble. Most of you are pretty cool too ;)

To the outreachers, Val, Paul and Paul, thanks for setting the example. I'm sure you guys have single handedly pushed many kids off the fence and into science....I hope to follow that example.

To the computer guys, Josh, Felix, Brandon, Mark and Lee, you guys have always been there with IDL answers, software discs, monitor adaptors and socialist propaganda....thanks :)

To all of the technicians and support staff, especially Ed, Mark and Bill Parkin, who have helped me build a million things, many of them research related, you guys are the backbone of the PSFC.

To Jessica and Corrinne, you guys have not only kept PSFC's trains running on time, but have both given the PSFC an energy that only you two have been able to. You're both awesome (each with your special, quirky kind of awesome) and I hope to keep your friendships for a while longer (not too long though?).

Before I finish the PSFC acknowledgements, I'd like to say a special word about Happy Paradise. I've always said that my greatest contribution to plasma has been convincing Felix to try to get a job at the PSFC, and the more time passes, the more I'm convinced of it. Felix, the turbulence whisperer, is not only a beast in what he does, but has a heart of gold and I'm proud to call him one of my best friends.

(Wow, this is going to be longer than my Chapter 4)

To all my UT and non-PSFC MIT (and beyond) friends along the way: Juajua, Andy, Angela, Lyrica, Chieze, Jared, Ben, Natalie, Tamer, Nancy, Michael Murrell, Puckett, Heather, Gregory, Nick, (plus all of you I'm missing), you've seen me in situations that could probably get me in trouble if public, so I thank you for staying quiet ;) and also for being my friends throughout these 56 dog years.

Nuribuggy, Gooy and Robyna...I've been informed that "Grab-donkey Rodriguez" loves you, whatever that means.

A few words about the people who helped me get to MIT and particularly, plasma physics: Ken Gentle, Roger Bengtson and Mel Oaks. Your v_0 has gotten me all the way to this $x(t)$.

Finalmente, un gran agradecimiento a mis compatriotas (y Mexicanos y Chicanos y

Españoles) con quien he compartido este tortuoso trayecto: A Charlie Henry, Felo y la Homera, que poco me ayudaron con la tesis pero no obstante los quiero mucho.
A los Sanyoryianos, UnNachos, Austinianos y MITianos: Cherry, Cata, Guillo, El Primo, Garton, Robin, Nancy, Mauricio, Abuelo, Mendoza, Esti, Iker, Ariana, Kika, Maria, Cesal, Juan Manuel, Violeta, Copete, Alejo, Andres, Aleja, Pedro, Laura, Claudia, Natalia, Angelique, Mariana, Daniel, Nida, Francisco, Heidi, Mario, Rago, Malexa, Luis, Kate, Chobis, Ana, Santiago y Caitlin...gracias por aguantarme lo que, aveces, son cantidades ultra-humanas. Los quiero mucho.
A Guio, Lucho y la tia Negra, gracias por el el amor y el apoyo de familia. A Yayi y Ferchanda, gracias porque de lejos siempre han estando pendientes de este Dominguecito aqui en Boston; sufriendo mis derrotas y celebrando mis victorias. Nestor, Paty y Sega, mi familia, gracias por todo el apoyo y el amor que siempre me dan y por recibirme con los brazos abiertos a la familia Pabon-Escobar; los quiero mucho. Y al Sandicito y Amelie mi hermano y sobrina franchutes: ou sont les cles, et merci.
Pax, gracias por siempre darme el carinio que me das. Siempre has sido un modelo a seguir, y me encanta hacerte sentir orgulloso de este hijito tuyo que tanto se parece a ti. Gracias por ser el pax eterno :)
Finalmente, como hace 8 años, el mayor agradecimiento de todos va a mis 4 mujeres, por siempre darme el amor y el apoyo que no se merece nadie pero que nunca paro de pedirles. Gracias por siempre estar a mi lado, asi sea desde Memphis, Austin, Tucson y NY, siempre estan aqui:
Titurria, toda la vida has estado pendiente de este sobrino consentido. Me diste vivienda y familia en Austin cuando recien llegue y siempre has estado ahi. Espero que esto marque el momento donde las mareas se tornan y te podamos dar todo el apoyo que te mereces, por ser como una segunda madre. Gracias titurria.
Chanchina, la proveedora del tough love menos tough en la historia. Mas que una amiga usted ha sido como una hermana para mi, y ademas tambien tiene el mismo sentido del humor....debe ser que lo sacamos del hogar que compartimos asi sea con un par de años de separacion. La quiero mucho y gracias por siempre confiar en su

hermanito.

Mi proyeneitor, que ha estado detras mio en todo este camino, desde las malas calificaciones en prekinder, las ulceras de los dias de notas en el San George, las lecturas que nunca hacia (como "Cuentos de Tomas Carrasquilla"). Tu has sido la que me ha guiado en esta vida, la que me ha enseñado el valor del saber. Pero tambien me has enseñado a ser transparente con mis emociones y me has mostrado que el amor no se esconde, que se muestra con orgullo, porque tu siempre lo has hecho con Francina y conmigo. Se que estas orgullosa de tu hijo...yo siempre he estado orgulloso de mi mama.

Mi luna, mi princesa, no es facil encontrar las palabras que expresen lo que has sido para mi durante la mitad de vida que hemos compartido. Desde la corona de flores al lado del gimnasio, las tocadas de guitarra en los pasillos del departamento de fisica de la Nacho, yo te he convertido en lo que eres y tu me has convertido en lo que soy, estamos indeleblemente impregnados el uno del otro. Este lazo que nos une ha sido atacado por la distancia, primero cuando me fui a Austin, y ahora este ultimo año, pero, no solo nos mantuvo unidos, sino que se ha vuelto mas fuerte, nutrido de todos los sacrificios que hemos hecho, solo para esos momentos en que nos volvemos a ver, a abrazar y a besar...los momentos en que volvemos a estar como sabemos que debemos estar, juntos. Durante este doctorado nos casamos en una ceremonia indudablemente nuestra, y comenzamos nuestra vida juntos en Eastgate. Ambos ansiosos de lo que nos depararia estas personalidades tan distintas viviendo la rutina diaria. Y creo que ambos quedamos sorprendidos al ver nuestra completa compatibilidad...nuestra vida junta, nos dimos cuenta, es como nuestras bailadas de salsa: usualmente estamos coordinados, pero cuando no, nos entendemos perfectamente y volvemos a nuestro ritmo, y siempre con sabrosuuuuuuraaa. Desde que llegaste a Boston, me has empujado para lograr mis metas, para salir adelante, aun cuando te tocaba sobarme la espalda a las 4 de la mañana cuando me despertaba sudando de la frustracion de la investigacion. Te tuviste que mamar todos los momentos mas duros, y estuviste ahi, abrazandome y confiando en que, con tu apoyo, lo lograriamos. Y lo hice, lo hicimos, gracias.

Y ahora, la princesa y el doctor, a donde nos lleve esta vida, pero bien agarraditos de la mano.

Contents

List of Figures

List of Tables

Chapter 1

Introduction

1.1 Nuclear fusion and magnetic confinement

1.1.1 Fusion as an energy source

Following the development of nuclear technology for defense purposes in the 1940s and 50s, a push began towards the development of fission and fusion technology for peaceful purposes. Advances in fission technology quickly led to the development of the fission nuclear power plant[28]. Parallel efforts focused on the advancement of fusion technology were undertaken.

The basic physics behind fusion as an energy source relies on the exothermic reactions involving hydrogen and helium isotopes:

$$D + D \rightarrow He^3 + n + 3.27MeV \tag{1.1}$$

$$D + D \rightarrow T + p + 4.03MeV \tag{1.2}$$

$$D + He^3 \rightarrow He^4 + p + 18.3MeV \tag{1.3}$$

$$D + T \rightarrow He^4 + n + 17.6MeV \tag{1.4}$$

Due to the abundance and ease of handling of deuterium, the first two reactions might be the preferable choice in a hypothetical reactor. However, as can be observed in Figure 1-1, the D-D reactions suffer from low reaction rates at the temperatures

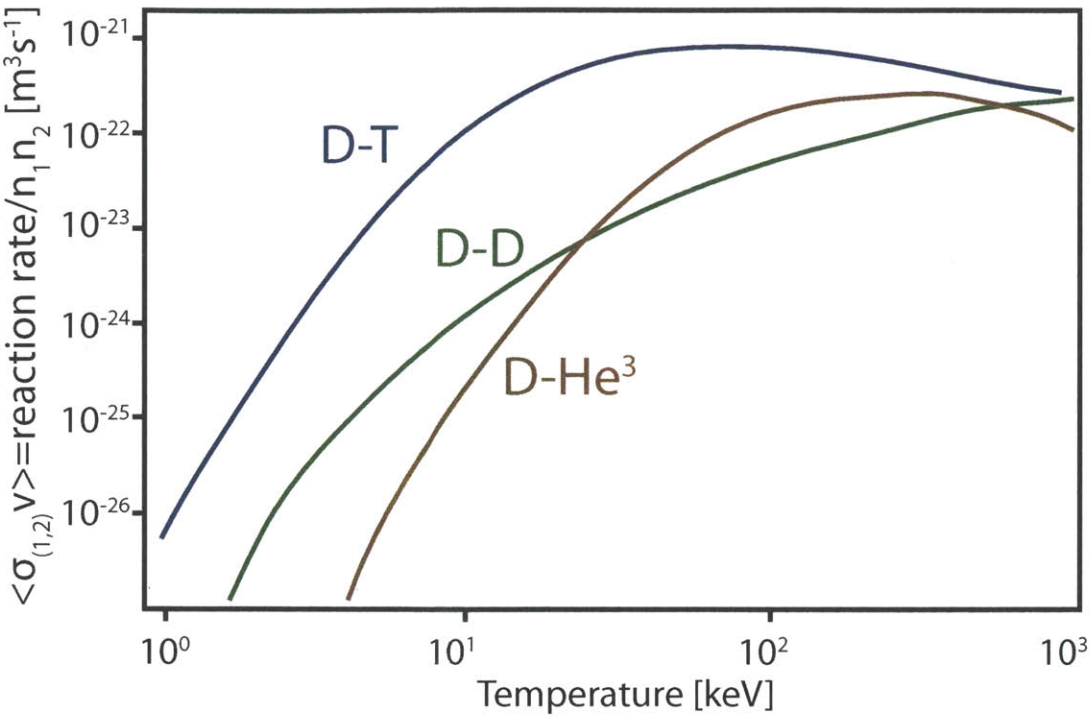

Figure 1-1: The reaction rates for the fusion relevant reactions are shown. The rate with the highest cross section is the Deuterium-Tritium reaction. This is the reaction on which the fusion community is focused for future reactors.

realistically accessible in laboratory plasmas (< 40keV). The $D - He^3$ would also be a desirable reaction to exploit due to its impressive energetic yield and to the fact that the reaction products are charged particles which can be contained by the magnetic fields and would reduce the wall damage due to very energetic neutrons. The main disadvantages of this reaction are, again, its low rates at reactor temperatures and the fact that He^3 is very rare on earth.

The remaining reaction, D-T has the disadvantage of requiring tritium which, itself, is rare and radioactive and of having energetic neutrons as one of its byproducts. The proposed use of Li blankets surrounding the nuclear reactor could tackle the tritium supply problem by utilizing the neutron output[29]. By using Li^6 enriched blankets, the tritium can be produced in the following reaction:

$$Li^6 + n_{slow} \rightarrow He^4 + T + 4.8MeV \tag{1.5}$$

from which it would be extracted as well as the excess heat which would be used to generate electricity through a power cycle. The tritium would then be used in the main fusion reaction. Several steps, including neutron multiplication and neutron moderation would also be needed for a working reactor.

The fusion reaction rate, as a function of the reaction cross sections, σ, can be written as $f = n_D n_T \langle \sigma_{DT} v \rangle$ where the $\langle ... \rangle$ denotes velocity space averaging, and n_D and n_T refer to the deuterium and tritium density respectively. The rate is maximized when $n_D = n_T = \frac{1}{2} n_e \equiv \frac{1}{2} n$, hence $f = \frac{1}{4} n^2 \langle \sigma v \rangle = (p^2 \langle \sigma v \rangle)/(16T^2)$ (the DT subscript has been suppressed) where $p = n_e T_e + n_D T_D + n_T T_T$, which, assuming $T \equiv T_e = T_D = T_T$, gives $p = 2nT$. This assumes that the impurities are negligible contributions to the density and the temperature. Since the energy with which every He^4 nucleus (known as an "α" particle) from the DT reaction (shown in Equation 1.4) is $E_\alpha = (1/5) \times 17.6MeV \approx 3.5MeV$, the power density provided by the αs from the fusion reactions is, therefore, given by[30]: $\mathbf{P}_\alpha = 3.5MeV \times p^2 \langle \sigma v \rangle / (16T^2)$. Meanwhile, the power lost from the plasma is characterized by the energy confinement time, τ_E, as:

$$\tau_E \equiv \frac{\mathbf{W}}{\frac{1}{V} P_{loss}} = \frac{3nTk_B}{\frac{1}{V} P_{loss}} \tag{1.6}$$

where $\mathbf{W}$ is the stored energy density (with stored energy, $W = \int \mathbf{W} dV$), V is the total volume of the plasma and k_B is the Boltzmann constant. For an ignited plasma, the α power must overcome the lost power[30]:

$$\mathbf{P}_\alpha > \frac{P_{loss}}{V} \tag{1.7}$$

$$\frac{3.5MeV \times p^2 \langle \sigma v \rangle}{16T^2} > \frac{(3/2) p k_B}{\tau_E} \tag{1.8}$$

$$2nT\tau_E = p\tau_E > \frac{24 k_B T^2}{3.5MeV \langle \sigma v \rangle} \geq 8.3 \text{ atm s @ } T = 15keV \tag{1.9}$$

The product $nT\tau_E$ is known as the *triple product* and it is a figure of merit for the reactor. The RHS of Equation 1.9 has been evaluated at T=15keV (note, 1eV=11,604K) for which it reaches its minimum, giving the triple product a lower limit below which ignition cannot be attained. This inequality implies that, in order to reach ignition

the plasma must be dense enough, hot enough and well confined. Similarly, the product $n\tau_E$, known as the *Lawson parameter*[31], is also used in the literature as a metric to gauge the quality of a fusion experiment[32][24][33].

The fact that the required temperatures for which these fusion reactions take place are in the tens of keV range require the use of clever confinement schemes that separate the reactants from the surrounding laboratory environment. Two main approaches have been proposed to deal with the confinement of the plasma, inertial confinement and magnetic confinement[1]. Inertial confinement fusion (ICF) uses very fast compression of pellets containing the fusion reactants (D and T) to generate fusion energy yield during the inertial timescale of the system[34][35]. With the construction and operation of the National Ignition Facility (NIF)[36], among other experimental facilities[37], ICF research has advanced greatly in the last decades. The second principal approach towards fusion, which I will focus on for the rest of this thesis, is magnetic confinement fusion (MCF)[33] which will be described in the following section.

1.1.2 Magnetic confinement and tokamaks

The Lorentz force exerted on an electrically charged particle of charge q moving with velocity $\vec{v}$ in a space with an electric field $\vec{E}$ and a magnetic field $\vec{B}$ is: $\vec{F} = q(\vec{E} + \vec{v} \times \vec{B})$. This implies that when $\vec{B}$ dominates, the electrically charged particle will spiral, following the direction of the magnetic field line (see Figure 1-2a). In this simple picture, the particle will traverse freely in the direction parallel to the magnetic field but is confined perpendicular to it to a gyroradius: $\rho_q = mv_\perp/qB$ where $v_\perp = \left|\vec{v} \times \vec{B}\right|/B$ (note that, as a shorthand, the magnitude of a vector is written as the variable with suppressed vector sign, e.g. $B \equiv \left|\vec{B}\right|$). If the magnetic fields close upon themselves the parallel direction is also confined as shown in Figure 1-2b. This is the basis of magnetic confinement.

The simplest solution is a torus with circular magnetic fields, where the magnetic

[1]Confinement schemes have been proposed that utilize alternative methods such as inertial-magnetic hybrids, nonetheless, the two most developed methods are ICF and MCF described.

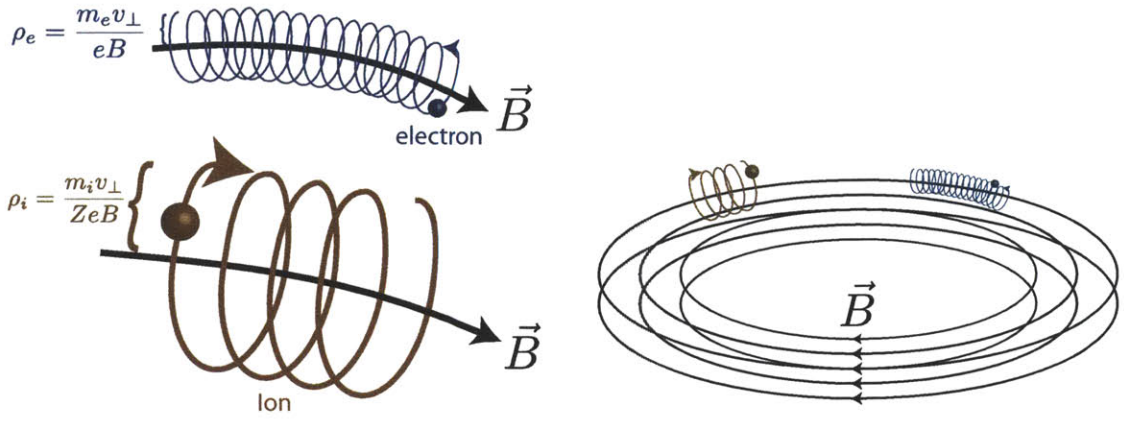

(a) (b)

Figure 1-2: a)electrons and ions spiral around magnetic fields at the gyro frequency and gyro radii. b) In order to contain the particles in the direction parallel to the magnetic field, the fields can be closed upon themselves.

fields can be constructed through magnetic coils surrounding the torus, creating fields in the $\hat{\phi}$ direction and the plasma is confined in a given region of $\hat{R}$ and $\hat{Z}$ (see Figure 1-3). The problem with this configuration comes from the ∇B drift:

$$v_{\nabla B} = \frac{v_\perp^2}{2\Omega} \frac{\vec{B} \times \nabla B}{B^2} \tag{1.10}$$

where Ω is the species cyclotron frequency, $\Omega = qB/m$, and the curvature drift:

$$v_\kappa = \frac{v_\parallel^2}{\Omega} \frac{\vec{R}_c \times \vec{B}}{R_c^2 B} \tag{1.11}$$

where $\vec{R}_c$ is the radius of curvature of the magnetic field. These drifts are in the $\hat{Z}$ direction and are in opposite direction for positive (ions) and negative (electrons) species, separating the charges vertically. This creates an electric field in the $\hat{Z}$ direction that ejects the plasma radially through an $\vec{E} \times \vec{B}$ type drift towards the walls of the machine. To solve this problem, a magnetic field is created that includes both a toroidal component, in the direction of the main torus, as well as a poloidal one circling the cross section of the plasma in the $\hat{\theta}$ direction of as shown in Figure 1-3. The two configurations which have been studied the most in MCF research that

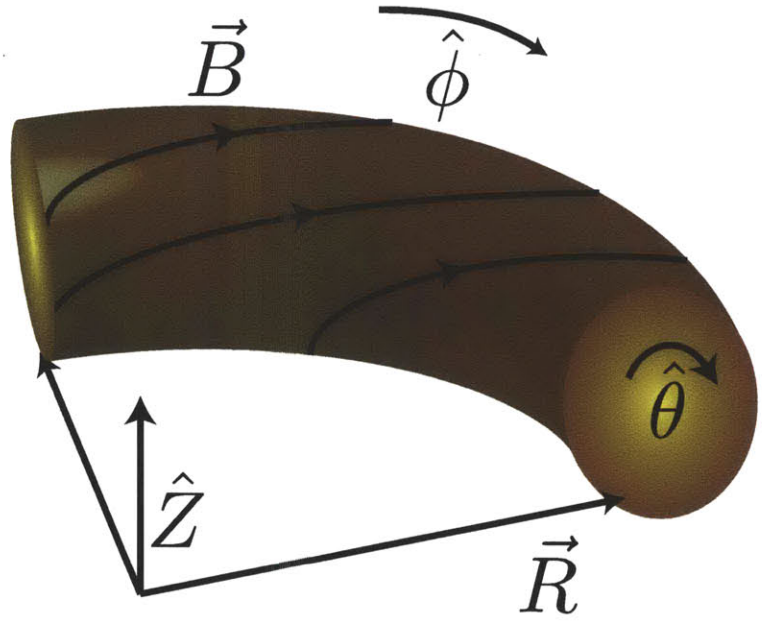

Figure 1-3: In order to maintain the plasma in equilibrium, a magnetic field with both a toroidal and a poloidal component is needed.

incorporate these types of magnetic fields are the Stellarator and the Tokamak[33].

Initially developed in the 1950s , the stellarator uses specially designed magnetic field coils which break the axisymmetry[38] ($\frac{\partial \phi}{\partial t} = 0$) of the system. The magnetic field lines are no longer circular but full toroidal flux surfaces which, on average, cancel out the drift away from the flux surfaces. The second major configuration, known as a *Tokamak*, features a central magnetic solenoid. During operation, a time varying current is applied to the solenoid which acts as the primary of a transformer, with the plasma acting as the secondary, inducing a plasma current in the toroidal direction. The current, in turn, produces a poloidal magnetic field inside the plasma. The resulting magnetic field is composed of B_ϕ in the toroidal direction and B_θ in the poloidal direction. As in the stellarator, the magnetic field lines in a tokamak trace full toroidal flux surfaces instead of circles, and the particles have no net curvature of ∇B drift away from the flux surfaces; in principle, the tokamak configuration is axisymmetric.

Since a linearly increasing current in the solenoid is needed to induce a toroidal

electric field, the tokamak configuration is intrinsically pulsed, that is, it cannot run steady state. In contrast, the stellarator requires no induced current, hence, it is not inherently transient. Advances in tokamak physics, like the discovery of the *bootstrap current*, a toroidal current generated by pressure gradients in the plasma, as well as technological advances like the development of auxiliary RF current drive, has extended tokamak pulses to order 100s lengths. The simplified geometry of the tokamak magnetic field coils results in more flexible plasma geometries as well as greater port access, which is ideal for physics and engineering research reactors.

The basic geometry of a tokamak can be seen in Figure 1-4. Its main components are: The metallic toroidal vacuum vessel wherein the working gas, typically deuterium (and tritium for D-T experiments), is puffed in and maintained at low pressure, toroidal magnetic field coils generating the $\vec{B}_\phi$ in the plasma, equilibrium magnetic field coils used for vertical and radial control, as well as plasma shaping, and the central solenoid responsible for the plasmas current, I_p, which provides the poloidal magnetic field, $\vec{B}_\theta$, and ohmic heating of the plasma: $P_{ohmic} = I_p^2 R_\Omega$, where R_Ω is the total plasma resistance. While this is the basic tokamak configuration, they are also equipped with various forms of auxiliary heating such as neutral ion beams, ion cyclotron minority heating, ECE heating, etc; as well as expansive diagnostic sets, additional magnetic field coils, cryogenic thermal shielding, etc. Over 200 tokamaks have been built up to date, of which, by 2012, more than 30 are still in operation[2], each with a unique configuration, hence, focused on specific areas of study.

1.2 Alcator C-Mod tokamak

After the successful operation of two previous high magnetic field compact tokamaks at MIT: Alcator A and Alcator C, a new tokamak was commissioned in 1993 which expanded the operational range of the previous iterations[39]. Alcator C-Mod retains the thrust set by its predecessors by operating at high magnetic field and density, with the addition of a divertor which enables a magnetic configuration in which the last

[2]For an up to date list, go to http://www.tokamak.info/

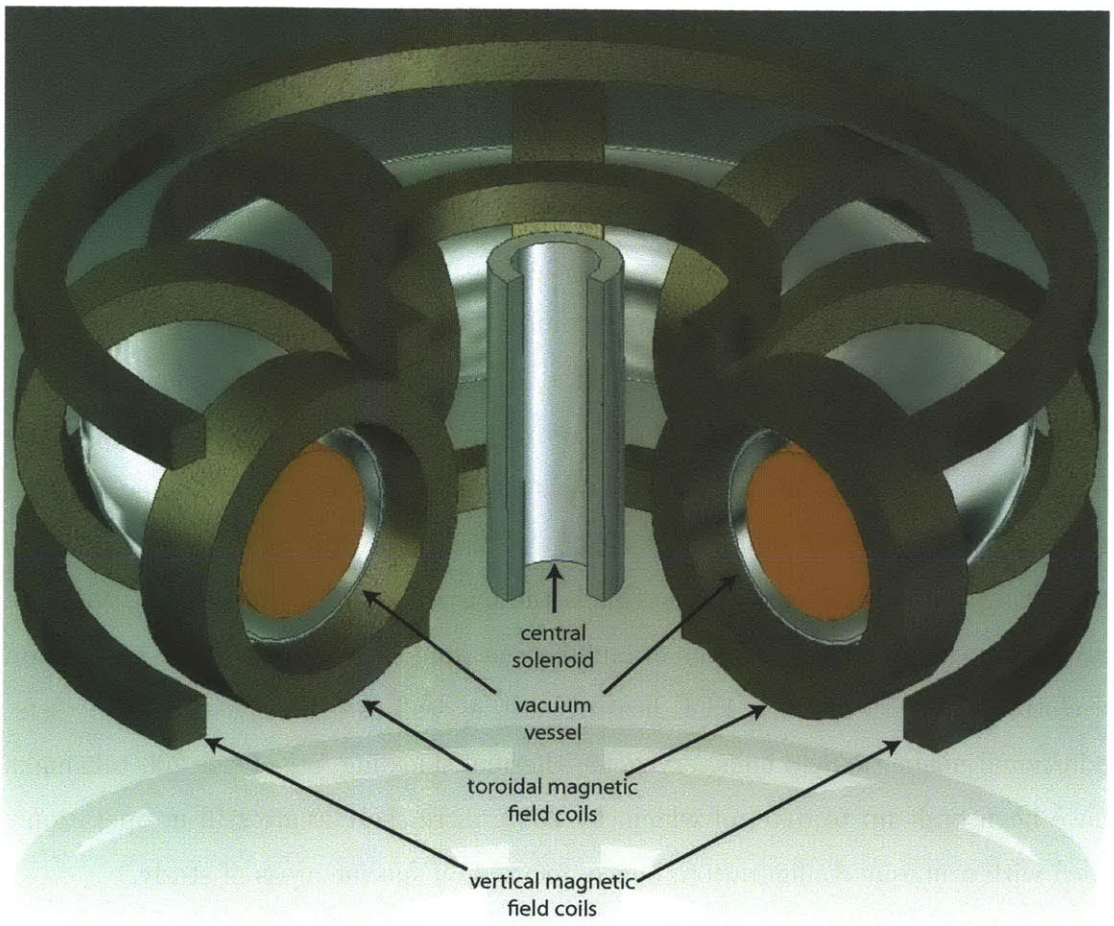

Figure 1-4: The basic tokamak includes a vacuum vessel to contain the plasma, a central solenoid which provides I_p and, hence, $\vec{B}_\theta$, as well as ohmic heating to the plasma, toroidal magnetic field coils for $\vec{B}_\phi$ and vertical field coils for plasma shaping and vertical positioning

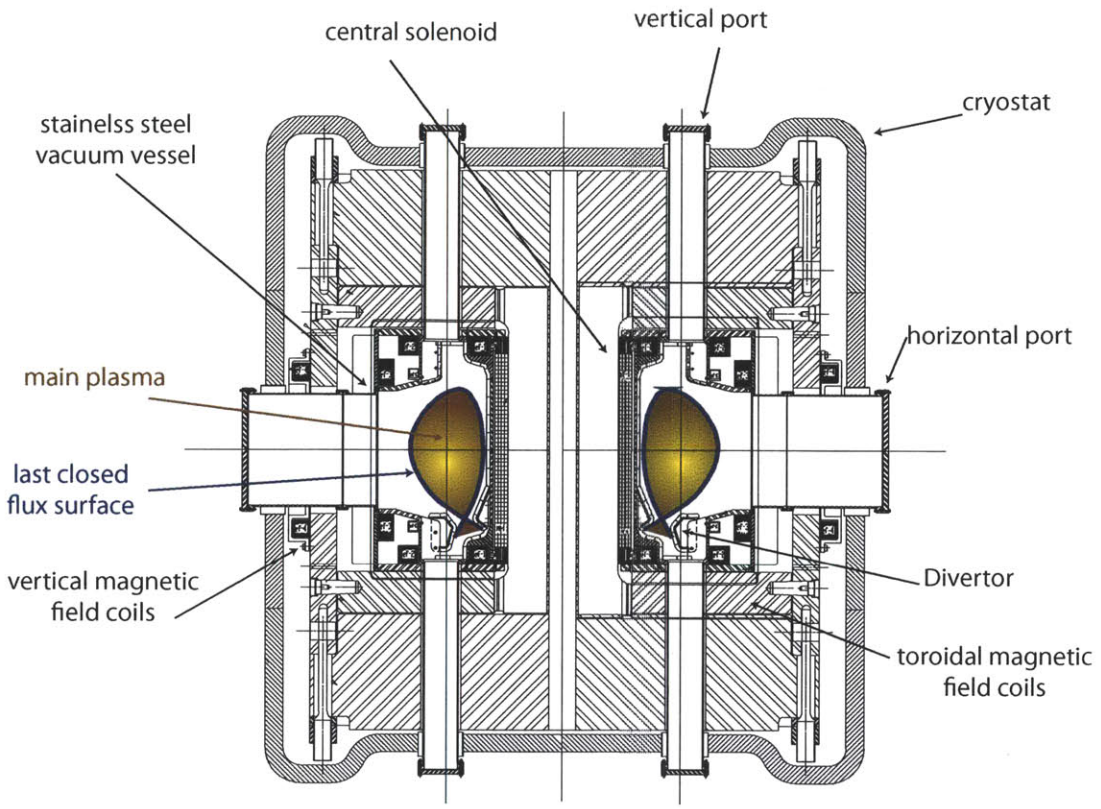

Figure 1-5: The Alcator C-Mod tokamak cross-section, wherein a lower single null plasma is plotted. The machine is encased in a cryostat needed to maintain the magnetic coils within operational temperatures.

closed flux surface of the confined plasma has no contact with the limiting surfaces of the main chamber. In this configuration, a magnetic X-point separates the main plasma from the divertor surfaces.

1.2.1 Alcator C-Mod parameters

The main engineering and plasma parameters of Alcator C-Mod are summarized in Table 1.1. It was constructed to study many topics of plasma physics and plasma engineering necessary for the development of future, energy producing tokamaks. Figure 1-5 shows the cross section of C-Mod. The main gas of operation is deuterium, but helium and hydrogen can also be used as main ion species.

The plasma is enclosed in a stainless steel vacuum vessel with 20 vertical and 10 hor-

Alcator C-Mod Parameters	
Major radius	0.67m
Minor radius	0.22m
Toroidal Magnetic Field	$3-8$T
Plasma Current	<2.02MA
Central density	$<5\times10^{20}$m^{-3}
Central temperature	<8keV
Pressure	$\sim$1.8atm
q_{95}	3-7
Auxiliary Heating	ICRF LHRF
Plasma surface components	W Mo

Table 1.1: Alcator C-mod physics and engineering parameters.

izontal entry ports used for diagnostic and RF antenna access. A 120 turns toroidal field magnetic coil, running currents of up to 250kA, surrounds the vessel creating magnetic fields of up to 8T at the center of the plasma with operation spanning $2T < \vec{B}_\phi < 8T$. 10 toroidally wound copper coils are used for position control and shaping.

The central solenoid in C-Mod consists of 3 independent coils wound around the core of the toroidal field magnet. By running linearly increasing currents of up to 30kA, the variable magnetic field induces a current inside the plasma, I_p, in the toroidal direction of up to 2MA which serves to ohmically heat the plasma as well as inducing a poloidal magnetic field, $\vec{B}_\theta$, used to maintain plasma equilibrium.

The first wall of the tokamak is lined by metallic high Z (Z=42) molybdenum tiles, including the inner and outer wall limiters. A closed divertor at the bottom of the machine and an open divertor at the top complete the interior of the machine. The high Z plasma surface components provide low deuterium retention and high heat load capabilities with low erosion. The need for low tritium retention and high power handling make high Z PFCs the leading candidates for use in tokamak reactors.

The presence of both limiters and divertors provides increased flexibility of plasma shaping, including the ability to run in lower single null topology, as shown in Figure

1-5, as well as in upper single null configuration, where the main x-point is above the plasma column. This flexibility has been crucial in the discovery of the I-mode regime, which will be discussed later in the chapter.

In addition to ohmic heating, the main auxiliary heating on Alcator C-Mod utilizes RF waves to heat minority Hydrogen or Helium^3 ions in the deuterium plasma[40]. The waves are launched at 50-80.5MHz into the plasma and can provide a total of up to 6MW heating. The minorities interact with the electrons through binary collisions and they, in turn, heat up the majority ions. Similarly, microwaves, at 4.6GHz, launched from the outboard side of the plasma column, can be used to accelerate electrons to high energies and drive currents non-inductively, thereby supplementing the solenoid-induced I_p.

While Alcator C-Mod is small in physical size compared to other fusion research tokamaks like DIII-D[41] and JET[32] which have major/minor radii of 1.66m/0.67m and 2.96m/1.25m respectively, due to C-Mod's high magnetic field, it has many parameters that are similar to ITER's. One of the advantages of the high magnetic field is that the magnetic pressure, $B^2/2\mu_0$, can sustain higher plasma pressures without letting the plasma go unstable. This has led to C-Mod reaching volume averaged pressures of $p = 1.8$ atm, a tokamak record[42]. While the temperature in ITER is expected to be about twice as high as that in C-Mod (approximately 15keV), ITER's $\beta_t \equiv 2\mu_0 p/B^2$ is expected to be closer to C-Mod's than that of other tokamaks, as seen in Figure 1-6.

1.2.2 Summary of confinement regimes on Alcator C-Mod

Alcator C-Mod has featured several confinement regimes, including:

- The Linear Ohmic Confinement (LOC) and Saturated Ohmic Confinement (SOC) regimes, which were originally observed on Alcator A and Alcator C.
- The L-Mode regime, both ohmic and with auxiliary heating.
- ELM-free H-modes, which exist without the presence of edge localized modes (ELMs) and are typically short lived.

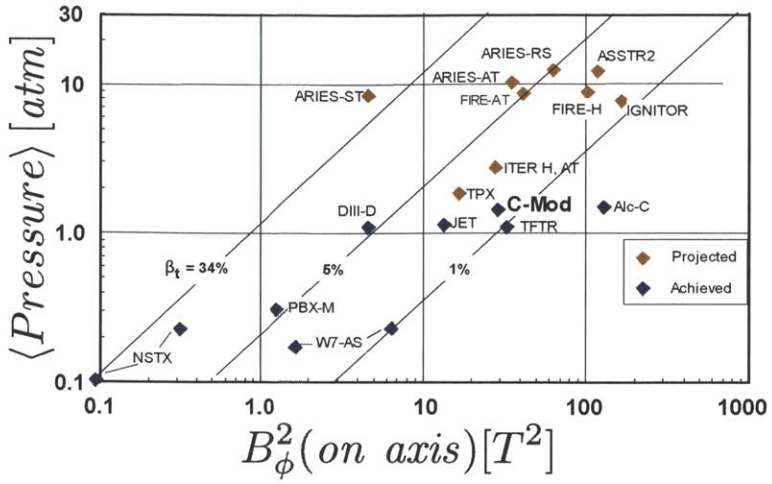

Figure 1-6: C-Mod's pressure and toroidal magnetic field position it well to study physics relevant to future tokamaks.

- ELMy H-modes which feature type I, II and III ELMs all of which have been observed on C-Mod.
- Enhanced D_α (EDA) H-Modes which can be sustained in steady state without the need for ELMs.

A review of these confinement regimes can be found in Appendix A, including a discussion about the possible physical mechanisms responsible for the different confinement characteristics of each regime.

1.2.3 Introduction to the I-Mode regime

The H-mode regime is characterized by the formation of edge transport barriers that confine both particles and energy which, as discussed in Appendix A, is believed to be due to the presence of E_r wells at the edge of the plasma, creating strong $v_{E\times B}$ shears that reduce turbulent transport at the pedestal. Nonetheless, the variety of H-modes discovered hint at the complexity of the physics behind the formation of this regime and its stabilization mechanisms.

Within the last 5 years, a novel regime has been discovered on the Alcator C-Mod Tokamak[1][2][3][4], which has also have been observed on AUG[16] and is currently

being searched for on DIII-D. It features high energy confinement reminiscent of the H-mode and low particle and impurity confinement similar to the L-mode (see Figure 1-7). The regime, named the *I-mode*, has been a major area of research on Alcator C-Mod since its identification and will be dealt with in detail in Chapter 3.

In the context of the L-mode and the different types of H-modes observed on C-Mod, the I-mode plays a unique role due to the separation of particle and energy transport, hence, it has the potential of elucidating relevant physical mechanisms involved in tokamak particle and energy transport.

E_r measurements in the I-mode have identified an E_r well located at the pedestal region, which can account for the high energy confinement[2][4]. In this thesis, I will explore the physics of the relatively low particle confinement in this regime through a study of edge fluctuations at the edge of the plasma and detailed measurements of particle transport in the same region.

1.3 Motivation for this thesis and outline

The H-mode regime was a big step in the development of magnetic confinement fusion. It opened the field of tokamak reactors to more economically feasible designs, including the potential of producing electricity that is competitive against more established energy production schemes. The physics behind this regime is still actively studied and has led to new theories and models describing the plasma behavior in a tokamak.

As will be discussed, the I-mode regime also has the potential of being an operational regime for next step tokamak reactors because of its favorable impurity control and high energy confinement. This regime brings a new piece of the puzzle to the understanding of plasma physics, particularly the physics behind particle and energy separation channels in tokamaks.

In Chapter 2, the relevant C-Mod diagnostic systems are presented. Emphasis is given to the O-mode reflectometry system, since most of the fluctuation measurements used in this analysis are from this diagnostic. This chapter includes a description of an

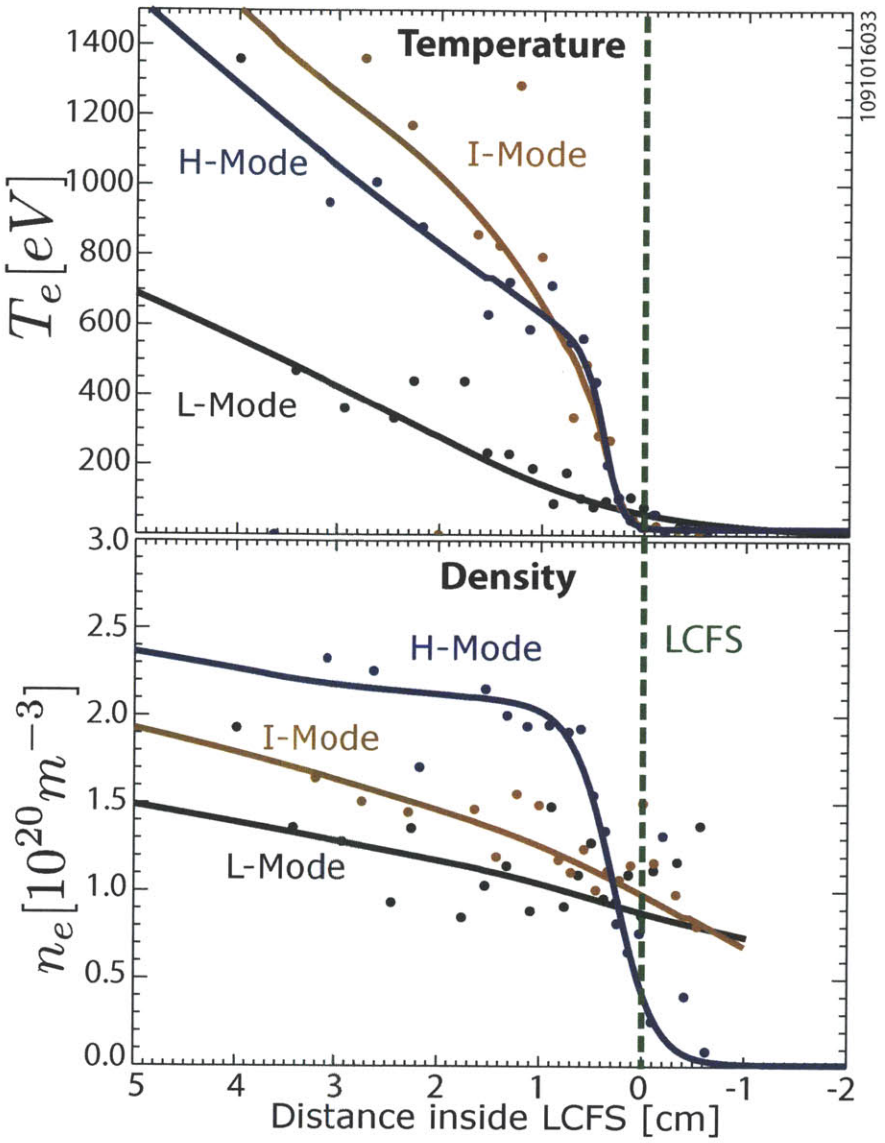

Figure 1-7: In the I-mode regime (red), a steep temperature pedestal is formed as in the H-mode (blue) while the density gradient at the plasma edge is maintained low, as in the L-mode (black)

upgrade of the reflectometry system which repurposed it to focus on detection of density fluctuations and which I spearheaded.

In Chapter 3, the I-mode regime is described in detail. The history of the mode, as well as its accessibility and global properties are discussed. The characteristic edge fluctuations that accompany the I-mode are presented, particularly the Weakly Coherent Mode (WCM) which in many regards is similar the the QCM. Many of the results included in this chapter were obtained by me directly and/or with the use of the upgraded reflectometry system discussed in Chapter 2.

Chapter 4 presents the particle transport measurements used to model the particle flux across the last closed flux surface during the I-mode. Having presented all the tools necessary for a comparison between the edge fluctuations in the I-mode and the particle transport, Chapter 5 presents the experimental plan and results, including the positive correlation between the intensity of the WCM and the particle transport across the LCFS.

Finally, the summary of the work is presented in Chapter 6, as well as possible experiments proposed to study this regime further.

Chapter 2

Fluctuation diagnostics

2.1 Introduction

Before a further explanation is given of the specific characteristics of the I-mode regime and of the particle transport measurements performed, it is helpful to review the main diagnostic systems used in the detection and characterization of fluctuations at the edge of the plasma. This is by no means an exhaustive review, but it is meant to introduce the tools used for the experimental analysis performed in this work.

2.2 Reflectometry

Initially developed as a tool for ionospheric studies, the reflectometry technique has been used in fusion experiments since the early 1980's[43]. This technique is similar to radar technology wherein a probing electromagnetic wave of a given frequency or combination of frequencies (e.g. wave packets), is sent into a plasma. The polarization and frequencies are chosen such that the wave's cutoff condition is satisfied in the probed plasma and the wave is reflected back towards the detection antenna which may or may not be the same as the launch antenna. Since the index of refraction of the plasma for a given wave is a function of the density and magnetic field, the user can deduce properties of the plasma based solely on the relation between the transmitted and received waves.

In this section, I will review the general theory behind the diagnostic technique, as well as describe the O-mode reflectometry system used in Alcator C-Mod [44].

2.2.1 Theoretical basis for reflectometry measurements

To derive the equations used in reflectometry studies, we begin with Ampere's and Faraday's laws:

$$\begin{aligned} \nabla \times \vec{E} &= -\frac{1}{c}\frac{\partial \vec{B}}{\partial t}, \\ \nabla \times \vec{B} &= \frac{1}{c}\frac{\partial \vec{E}}{\partial t} + \frac{4\pi \vec{J}}{c}. \end{aligned}$$

Which can be combined to form:

$$\nabla^2 \vec{E} - \nabla(\nabla \cdot \vec{E}) - \frac{1}{c^2}\frac{\partial^2 \vec{E}}{\partial t^2} - \frac{4\pi}{c^2}\frac{\partial \vec{J}}{\partial t} = 0. \tag{2.1}$$

Since the phase velocity of the waves is much larger than typical thermal speeds $v_{ph} \gg v_{the} \gg v_{thi}$ at the edge of Alcator C-Mod plasmas, the cold plasma dispersion relation applies[44]. For the cold plasma approximation, the pressure gradient term in the momentum equation can be neglected, and the single species momentum equation can be written as:

$$\frac{\partial \vec{v}_j}{\partial t} = \frac{q_j}{m_j}\left(\vec{E} + \frac{\vec{v_j} \times \vec{B}}{c}\right) - \cancel{\frac{\nabla p}{m_j n_{oj}}}.$$

The incoming waves cause small perturbations to the equilibrium quantities and can, therefore, be expressed as Fourier 1st order linear perturbations:

$$\vec{E}_1 \sim \vec{B}_1 \sim \vec{v}_{j1} \sim n_1 \sim \exp\left[i\left(\vec{k} \cdot \vec{r} - \omega t\right)\right], \tag{2.2}$$

for individual species of ions or electrons "j". One of the advantages of this method is the resulting simplicity of the temporal and spatial derivatives. If the variable Q_1 is assumed to be a generic variable that satisfies the condition set in Equation 2.2, then: $\frac{\partial Q_1}{\partial t} = -i\omega Q_1$ and $\nabla Q_1 = i\vec{k}Q_1$. For an equilibrium magnetic field, $\vec{B}_0 = B_0\hat{b}$,

the following equations are satisfied for the first order terms in the expansion:

$$\frac{\partial \vec{v}_{1j}}{\partial t} \sim -i\omega \vec{v}_{1j} = \frac{q_j}{m_j}\left(\vec{E}_1 + \frac{\vec{v_{1j}} \times \vec{B}_0}{c}\right), \tag{2.3}$$

$$\vec{J} = \vec{J}_1 = \sum_j n_{j0} q_j \vec{v}_{j1}. \tag{2.4}$$

We can then combine Equations 2.1 and 2.4 as:

$$-N^2 \vec{E}_1 + \vec{N}(\vec{N} \cdot \vec{E}_1) + \vec{E}_1 + \frac{4\pi i}{\omega} \sum_j n_{j0} q_j \vec{v}_{j1} = 0, \tag{2.5}$$

where $\vec{N} = \frac{c\vec{k}}{\omega}$ is the index of refraction for the wave. Note that Equation 2.3 establishes a relationship between the perturbed velocities of the electrons and ions and the perturbed electric field $\vec{E}_1$; therefore, Eq. 2.5 describes a set of homogenous linear equations for (E_{1x}, E_{1y}, E_{1z}). Using Stix notation[44] and assuming (without loss of generality) that the direction of the equilibrium magnetic field, $\hat{b} = \hat{z}$ and $\vec{N} = (N_x, 0, N_z) = \frac{c}{\omega}(k_x, 0, k_z)$, the following matrix equation arises:

$$\begin{bmatrix} S - N_z^2 & -iD & N_x N_z \\ iD & S - N^2 & 0 \\ N_x N_z & 0 & P - N_x^2 \end{bmatrix} \cdot \begin{bmatrix} E_{1x} \\ E_{1y} \\ E_{1z} \end{bmatrix} = \begin{bmatrix} 0 \\ 0 \\ 0 \end{bmatrix}, \tag{2.6}$$

where:

$$S \equiv 1 - \sum_j \frac{\omega_{pj}^2}{\omega^2 - \Omega_j^2} \quad ; \quad D \equiv \sum_j \frac{\Omega_j}{\omega} \frac{\omega_{pj}^2}{\omega^2 - \Omega_j^2};$$

$$P \equiv 1 - \sum_j \frac{\omega_{pj}^2}{\omega^2};$$

$$\omega_{pj}^2 = \frac{4\pi n_{0j} q_j^2}{m_j} \quad ; \quad \omega_{cj} = |\Omega_j| = \frac{|q_j| B_0}{m_j c}.$$

If the probing waves are transmitted into the plasma perpendicular to the equilibrium $\vec{B}_0$ (as is the case in Alcator C-Mod), assuming $\vec{B}_0 = B_0 \hat{z}$, then $N_z = 0$ and therefore $\vec{N} = N_x \hat{x}$ and $\vec{k} = k_x \hat{x}$. Using this simplification, we can deduce a dispersion relation

for the waves by forcing the determinant of the first matrix in Equation 2.6 to be zero in order to find a non-trivial solution for $\vec{E_1}$. This leads to the following equation:

$$\left(S \cdot (S - N^2) - D^2\right)\left(P - N^2\right) = 0, \tag{2.7}$$

which has two solutions for N^2:

$$N^2 = \frac{S^2 - D^2}{S}, \tag{2.8}$$

$$N^2 = P = 1 - \frac{\omega_{pe}^2}{\omega^2} - \sum_j \frac{\omega_{pj}^2}{\omega^2} \sim 1 - \frac{\omega_{pe}^2}{\omega^2}, \tag{2.9}$$

where j in Equation 2.9 refers to all ions. It can be shown, by replacing N^2 from Equation 2.8 in matrix Equations 2.6, that for waves which satisfy $N^2 = \frac{S^2-D^2}{S}$, the electric field amplitude is of the form: $(E_{1x}, E_{1y}, 0)$, that is, perpendicular to the equilibrium magnetic field $\vec{B_0}$, as shown in Figure 2-1(a). These waves, denoted X-mode (or extraordinary) waves, have a dispersion relation that depends on both, the local density, and $\vec{B_0}$. X-mode wave reflectometry systems in tokamaks have the advantage of probing through hollow and flat density profiles, but have the disadvantage of requiring very high microwave frequencies, especially in high density, high $\vec{B_0}$ tokamaks such as Alcator C-Mod and ITER. Recently, an X-Mode reflectometry system has been installed and commissioned in Alcator C-Mod that probes the scrape-off layer of the plasma, where the density is sufficiently low to use economically accessible microwave technology[45].

By substituting the $N^2 = P$ solution (Equation 2.9) into the matrix Equation 2.6, it can be shown that this dispersion relation describes a wave with an electric field amplitude of the form $(0, 0, E_{1z})$, that is, parallel to the equilibrium magnetic field $\vec{B_0}$ as can be seen in Figure 2-1(b). In Equation 2.9, the fact that $m_e \ll m_i$ has been used to simplify the dispersion relation to the simple form: $N^2 = 1 - \frac{\omega_{pe}^2}{\omega^2}$. These waves are denoted as O-Mode (or ordinary) waves and have a dispersion relation that only depends on the electron density n_0 (from the density dependence of ω_{pe}). For O-mode propagation, the electrons are only accelerated parallel to $\vec{B_0}$ so they don't

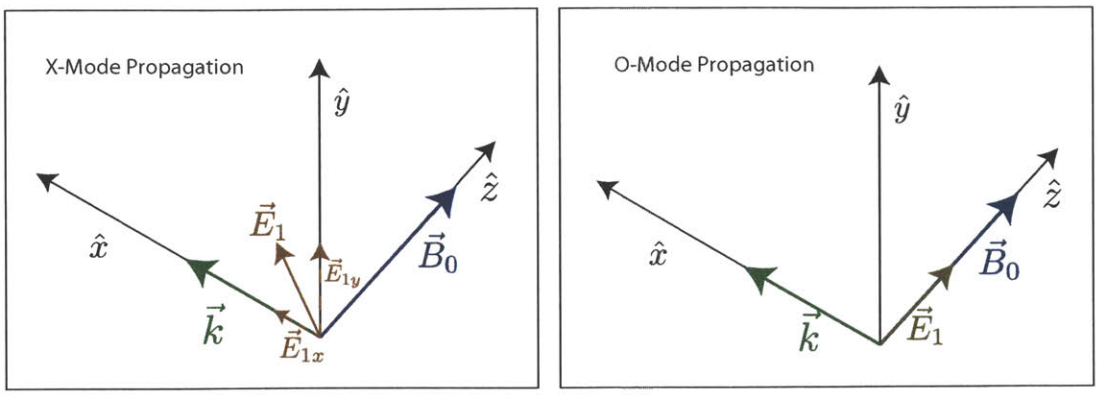

Figure 2-1: Geometry of X-Mode and O-Mode wave propagation

feel any force from the magnetic field, while the ions are taken as stationary. The O-mode can exist in the plasma regardless of the existence of the magnetic field (for $\vec{B_0} = 0$, the wave is simply a modified free space light wave).

By setting $N^2 = 0$, or $\omega^2 = \omega_{pe}$, in Equation 2.9, the condition for propagation of the wave is obtained. For cases where the $RHS > 0$, then $k^2 > 0$ and the equations describe an oscillatory solution corresponding to propagating waves. On the other hand, if the $RHS < 0$, then $k^2 < 0$ which leads to an evanescent wave and reflection. As the waves are launched from outside the plasma, they start with $\omega \gg \omega_{pe}$ so $N^2 \sim 1$. As the electromagnetic wave reaches the density layer that satisfies the cutoff condition:

$$N^2 = 0 \rightarrow \omega = \omega_{pe} \tag{2.10}$$

the wave can no longer propagate into the plasma. As will be discussed later, to satisfy the boundary conditions at the cutoff layer, the wave must reflect back, perpendicular to the reflection layer.

WKBJ solution to the O-Mode wave equation

For O-Mode polarization, Equation 2.1 can be expressed in the simplified form:

$$\nabla^2 \vec{E} - \frac{1}{c^2}\frac{\partial^2 \vec{E}}{\partial t^2} - \frac{\omega_{pe}^2}{c^2}\vec{E} = 0 \tag{2.11}$$

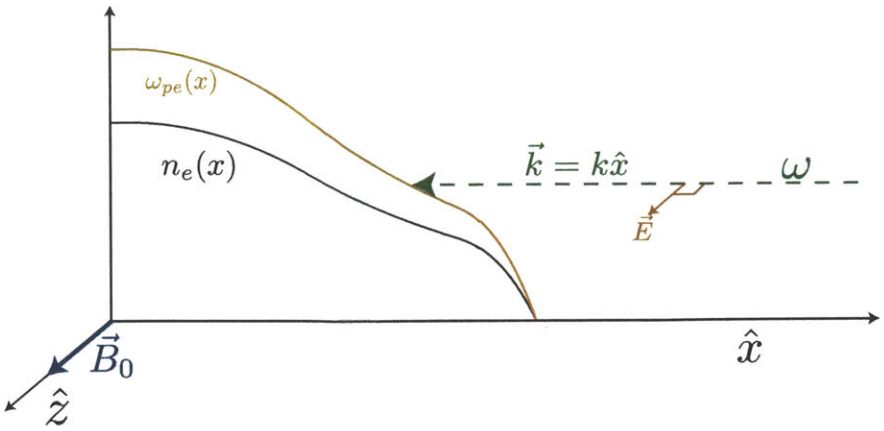

Figure 2-2: Accessibility of O-Mode reflectometry waves in a plasma. As the cutoff condition is reached, the wave can no longer penetrate into the plasma and is reflected.

where the "1" subscript has been dropped. In the previous section, we have investigated the Fourier expansion in both temporal and spatial dimensions. These solutions are *locally* valid and lead to the dispersion relation: $\frac{c^2}{\omega^2}k^2 = 1 - \frac{\omega_{pe}^2(n_e)}{\omega^2}$ (where $k \equiv \left|\vec{k}\right|$). In a typical tokamak plasma, however, the electron density, n_e, and hence ω_{pe}, varies with spatial location, as represented in Figure 2-2. This inhomogeneity requires a solution with a more general spatial dependence than $\vec{E} \propto e^{i\vec{k}\cdot\vec{r}}$. Keeping the temporal Fourier decomposition, we can assume an electric field of the form $\vec{E} = (0, 0, E_z(x))e^{-i\omega t}$. Using this solution, Equation 2.11 can be simplified resulting in the scalar equation:

$$\frac{d^2E_z}{dx^2} + \frac{\left(\omega^2 - \omega_{pe}^2(x)\right)}{c^2}E_z = 0 \tag{2.12}$$

We note that when the second term of Equation 2.12 is constant, that is, if $\omega_{pe}(x) = constant$, the simple wave function $\vec{E} = E_z e^{i(k_x x - \omega t)}$ is a valid solution (now global as well as local).

If, on the other hand, the spatial variation of the $\frac{\left(\omega^2 - \omega_{pe}^2(x)\right)}{c^2}$ term is weak, an approximate solution for Equation 2.12 can be obtained using the WKBJ method, developed initially for applications in quantum mechanics[46]. For O-Mode reflectometry, if the condition:

$$\frac{\lambda}{2\pi} \equiv \frac{c}{\omega} \ll L_n \equiv \left|\frac{1}{n_e}\frac{dn_e}{dx}\right|^{-1} \tag{2.13}$$

is satisfied, then the solution to Equation 2.12 maintains the wave-like form[44]:

$$E_z(x) = \frac{E_{0\pm}}{\left(1 - \frac{\omega_{pe}^2(x)}{\omega^2}\right)^{1/4}} \exp\left(\pm i\frac{\omega}{c}\int^x \left(1 - \frac{\omega_{pe}^2(x)}{\omega^2}\right)^{1/2} dx\right) \tag{2.14}$$

where $E_{0\pm}$ is determined by boundary conditions. There are several important points to make about this solution:

1. As stated before, it is only valid away from the cutoff condition $\omega = \omega_{pe}$. This means that, as the wave reaches the cutoff layer (a distance which will be quantified in the next section), another solution to the wave Equation 2.12 must be used.

2. The WKBJ approximation is not valid where $\lambda/2\pi \geq L_n$, so effects of large density gradients along the propagation path (such as edge density barriers) must be handled with care.

3. The amplitude of the wave is modulated by the inverse square root of the index of refraction: $\left|\vec{N}\right|^{-1/2} = \left(1 - \frac{\omega_{pe}^2}{\omega^2}\right)^{-1/4}$ which implies that, as the wave approaches the cutoff condition, its amplitude will grow.

4. The $\pm$ that precedes the exponential factor implies that the actual solution is a linear combination of two waves (the incident and reflected) propagating along the positive and negative $\hat{x}$ direction (hence the $\pm$ subscripts in $E_{0\pm}$). The amplitudes will be determined by the RF power launched by the antenna and the boundary conditions at the cutoff layer.

The WKBJ solution is suitable to describe reflectometry wave propagation through most of the plasma except, crucially, close to the reflection layer which will be the topic of the next section.

Exact solution close to the cutoff layer

If the electron density varies slowly at the turning point (the critical density at which $\omega_{pe} = \omega$ of the incoming reflectometry wave), the density can be taken as a linear

function:

$$n_e(x) = n_e(x_0)\left(1 - \frac{(x - x_0)}{L_n}\right) \tag{2.15}$$

where the cutoff condition occurs at $x = x_0$, at a density $n_e(x_0)$, hence $n_e(cutoff) = n_e(x_0)$, $n_e > n_e(x_0)$ for $x < x_0$ and $n_e < n_e(x_0)$ for $x > x_0$. Using this simplified density form, the wave Equation 2.12 simplifies to:

$$\frac{\partial^2 E(\zeta)}{\partial \zeta^2} - \zeta E(\zeta) = 0 \tag{2.16}$$

where the subscript z in E_z has been dropped for convenience and:

$$\zeta = \left(\frac{L_n}{k_0^2}\right)^{-1/3}(x_0 - x) \quad \text{with} \quad k_0 \equiv \frac{\omega}{c} \tag{2.17}$$

Note that as x increases, ζ decreases. Equation 2.16 is known as the Airy equation [47]. ζ can be either positive, for $n_e > n_e(cutoff)$ or negative when $n_e < n_e(cutoff)$. The solution to Equation 2.16 is:

$$E(\zeta) = \alpha Ai(\zeta) + \beta Bi(\zeta) \tag{2.18}$$

where Ai and Bi are the Airy functions of the first type and second type, respectively:

$$Ai(\zeta) = \frac{1}{\pi}\int_0^\infty \cos\left(\frac{1}{3}t^3 + \zeta t\right) dt \tag{2.19}$$

$$Bi(\zeta) = \frac{1}{\pi}\int_0^\infty \left[e^{-\frac{1}{3}t^3 + \zeta t} + \sin\left(\frac{1}{3}t^3 + \zeta t\right)\right] dt \tag{2.20}$$

The Airy function solutions have been plotted in Figure 2-3. As can be observed, both Ai and Bi display oscillatory behavior in the region where $N^2 > 0$ ($n_e < n_e(cutoff)$), while, as the solutions penetrate the high density region, the Bi solution exponentially increases and the Ai function decays exponentially. This behavior is clear from the

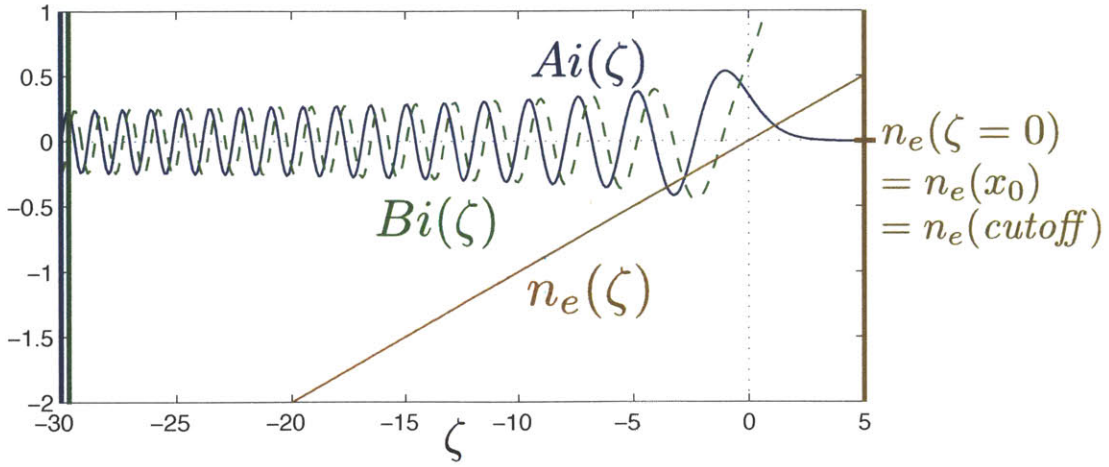

Figure 2-3: Airy function are solutions to the wave equation with a linear density profile of the form: $n_e(x) = n_e(x_0)\left(1 - \frac{(x-x_0)}{L_n}\right)$ and $\zeta = (L_n/k_0^2)^{1/3}(x_0 - x)$.

asymptotic formulae of the Airy functions[47]:

$$\begin{aligned} & & \text{As } \zeta & \rightarrow & -\infty & \\ Ai(-\zeta) \rightarrow \frac{1}{\sqrt{\pi}\zeta^{1/4}} \sin\left(\frac{2}{3}\zeta^{3/2} + \frac{\pi}{4}\right) & \text{and} & Bi(-\zeta) \rightarrow \frac{1}{\sqrt{\pi}\zeta^{1/4}} \cos\left(\frac{2}{3}\zeta^{3/2} + \frac{\pi}{4}\right), & \\ & & \text{As } \zeta & \rightarrow & +\infty & \\ Ai(\zeta) \rightarrow \frac{e^{-\frac{2}{3}(\zeta)^{3/2}}}{2\sqrt{\pi}\zeta^{1/4}} & \text{and} & Bi(\zeta) \rightarrow \frac{e^{\frac{2}{3}(\zeta)^{3/2}}}{\sqrt{\pi}\zeta^{1/4}} & . \end{aligned}$$

Since the solution must decay as it goes into the evanescent region, the Bi coefficient in equation 2.18 must be zero: $\beta = 0$. If we now include the temporal dependence of the wave, $e^{\pm i\omega t}$, the total wave describes incoming and outgoing traveling solutions for $\zeta \ll -1$ of the form:

$$\begin{aligned} E(\zeta, t) &= \alpha Ai(\zeta)\cos(\omega t) && (2.21) \\ &\sim \frac{\alpha}{2\sqrt{\pi}(-\zeta)^{1/4}} \cos\left(\frac{2}{3}(-\zeta)^{3/2} - \frac{\pi}{4}\right)\cos(\omega t) && (2.22) \\ &= \frac{\alpha}{4\sqrt{\pi}(-\zeta)^{1/4}}\left[\cos\left(\frac{2}{3}(-\zeta)^{3/2} - \frac{\pi}{4} - \omega t\right) + \cos\left(\frac{2}{3}(-\zeta)^{3/2} - \frac{\pi}{4} + \omega t\right)\right], \end{aligned}$$

where $\sin(z+\frac{\pi}{4}) = \cos(z-\frac{\pi}{4})$ has been used. Since the energy carried by the wave is proportional to $|E|^2$, the fact that the amplitudes of the incoming and outgoing waves are equal, shows that the wave energy is not absorbed by the plasma at the evanescent region and is, therefore, entirely reflected.

One can manipulate the spatial phase factor of Eq. 2.22 by recalling the linear density approximation, Equation 2.15 and noting that, close to the cutoff: $N^2(x) \sim (x - x_0)/(Ln)$:

$$\Phi \equiv \frac{2}{3}(-\zeta)^{3/2} - \frac{\pi}{4} \tag{2.23}$$

$$= \frac{2}{3}\left(L_n/k_0^2\right)^{-1/2}(x-x_0)^{3/2} - \frac{\pi}{4} \tag{2.24}$$

$$= \frac{\omega}{c\sqrt{L_n}}\int_{x_0}^{x}(x'-x_0)^{1/2}\,dx' - \frac{\pi}{4} \tag{2.25}$$

$$= \frac{\omega}{c}\int_{x_0}^{x} N(x')dx' - \frac{\pi}{4} \tag{2.26}$$

When compared with the WKBJ approximation in Equation 2.14, we can identify Φ as the phase factor (the term in the exponential) with an added $\pi/4$ constant. From Equation 2.24 we can also identify the characteristic length which defines proximity to the cutoff layer in this model: $(L_n/k_0^2)^{1/3}$. The resolution length scale that is more widely used is the Airy width: $W_A = 1.63(L_n/k_0^2)^{1/3} = 0.48(\lambda_0^2 L_n)^{1/3}$[48][49], where $k_0 = 2\pi/\lambda_0$ has been used (λ_0 being the freespace wavelength). For distances much greater than W_A from the cutoff layer, the WKBJ approximation suffices. Since the reflectometry wave travels from the antenna to the reflection layer and back, the total phase gained by the wave in the process is given by:

$$\Phi_{tot} = \frac{2\omega}{c}\int_{x_0}^{a} N(x')dx' - \frac{\pi}{2}\,. \tag{2.27}$$

Equation 2.27 is the basis for much of reflectometry research. It tells us that if a 1D approximation can be assumed, and if the phase gained in the returning signal can be accurately measured, one can deduce properties of the plasma through which it is traveling, particularly the index of refraction. If many channels are simultaneously

used, one can use a technique similar to an Abel inversion[50] to reconstruct the density profile of the plasma. This was the primary use of the reflectometry system on Alcator C-Mod as originally constructed[51], as will be discussed in the Section 2.2.3.

In laboratory plasmas the physics scenarios are inherently three dimensional so the simple analysis described above is incomplete. Nonetheless, due to symmetries in the plasma (such as toroidal symmetry) and the fact that in many cases the waves are launched and received equidistant from the midplane and close to normal to the reflecting layer, the simple 1D description encompasses the principal physics relevant to the diagnostic. Higher dimensional effects will become relevant in the discussion regarding the use of reflectometry to measure density fluctuations occurring along the wave path.

2.2.2 Measuring density fluctuations using reflectometry

Reflectometry has been used to measure density fluctuations for several decades including early measurements of turbulence in tokamaks[52][?]. Nonetheless, quantitative interpretations of the measurements have required increasingly advanced models and such techniques are still current[43]. In this section, I will present the theoretical framework used for the interpretation of the reflectometry fluctuation measurements acquired in the experiments reported here.

One dimensional models

The first approach that can be taken to analyze the effects of density fluctuations is to add a perturbation that propagates in the same dimension as the probing wave, that is, $\vec{K}_{fl} \parallel \vec{k}_0$ and restrict the geometry of the problem to 1D defined by the $\vec{k}_0$ direction. In typical plasma scenarios, the 3D effects of the plasma-wave interactions, as well as the fact that in general $\vec{K}_{fl} \not\parallel \vec{k}_0$, are important; nonetheless, the $\vec{K}_{fl} \parallel \vec{k}_0$ approximation makes for a mathematically tractable problem due to its 1D character and gives important insights about the general interpretation of density fluctuations

using reflectometry.

Before a model of the fluctuating density is proposed, it is useful to explore the effects of a generic first order fluctuating density on the WKB phase gain (Equation 2.27). Consider a fluctuating density: $n_e = n_{0e} + \tilde{n}_e$, such that n_{0e} is the equilibrium density profile and $\tilde{n}_e$ is a perturbation to the equilibrium. The linearized form of Equation 2.27 is:

$$\Phi + \tilde{\Phi} = \frac{2\omega}{c}\int_{x_0}^{x}\sqrt{1 - \frac{4\pi e^2(n_{0e} + \tilde{n}_e)}{\omega^2 m_e}}dx' - \frac{\pi}{2}. \tag{2.28}$$

If $\tilde{\omega}_{pe}^2/\omega^2 \ll 1 - \omega_{pe}^2/\omega^2$, where $\tilde{\omega}_{pe}^2 \equiv 4\pi e^2\tilde{n}/m_e$ is an equivalent plasma frequency for the density perturbation, then:

$$\tilde{\Phi} = \frac{2\omega}{c}\int_{x_0}^{x}\frac{\tilde{\omega}_{pe}^2/\omega^2}{2\sqrt{1 - \omega_{pe}^2/\omega^2}}dx' \tag{2.29}$$

By assumption this result is valid only far from the reflection layer. Nonetheless it shows that, even though the fluctuations throughout the whole path of the probing wave contribute to $\tilde{\Phi}$, it is the ones closest to the reflection layer that contribute most strongly (since the denominator in the RHS integrand goes to zero). This is the basis for the fluctuation assumption used in reflectometry: the fluctuations measured are generally assumed to be close to the reflection layer of the probing frequency.

In [48], the author tackles the effect of a generic fluctuation of the index of refraction (a proxy for density fluctuation in O-mode reflectometry) on the total phase gain by solving the full 1D inhomogeneous wave equation:

$$\frac{d^2\tilde{E}}{dx^2} + \frac{\omega^2}{c^2}N^2\tilde{E} = -\frac{\omega^2}{c^2}\tilde{N}^2 E_0 \tag{2.30}$$

where N is the index of refraction applied to the equilibrium density, $\tilde{N}^2 \equiv \tilde{\omega}_{pe}^2/\omega^2$, E_0 is the solution to the homogeneous Equation 2.12 and $\tilde{E} = E - E_0$. By using a Green's function method, the author solves the inhomogeneous equation. The perturbation

to the return field is:

$$\tilde{E}_{ret} = 2iE_{ret}\int_{x_0}^{x}\frac{\omega^2}{c^2}\tilde{N}^2\frac{E^2}{W}dx' = \frac{2i\omega E_{ret}}{c}\int_{x_0}^{x}\frac{\tilde{\omega}_{pe}^2}{\omega^2}\frac{k_0E^2}{W}dx' \tag{2.31}$$

where E_{ret} is the complex amplitude of the returned reflectometry wave electric field far from the cutoff layer (e.g. at the antenna plane) and $\tilde{E}_{ret}$ is the perturbation to this field. The total phase gained by the returned reflectometry signal can then be derived from Equation 2.31 to be:

$$\tilde{\Phi} = \frac{2\omega}{c}\,\mathrm{Re}\int_{x_0}^{x}\frac{\tilde{\omega}_{pe}^2}{\omega^2}\frac{k_0E^2}{W}dx' \tag{2.32}$$

where "W" is the Wronskian[53] between the unperturbed solutions and which, for this case, is simply a constant. The fullwave result from Equation 2.32 can be compared to the result from the WKB approximation in Equation 2.29 by plotting the factor that multiplies the fluctuating component, $\tilde{\omega}_{pe}^2/\omega^2$ in the integrand of both equations, as is done in Figure 2-4, following [48]. In this example, the same parameters have been taken as in Figure 2-3, wherein the density profile is of the form $n_e = n_e(0)\,(1 - x/L_n)$.

The integrand asymptotes to $+\infty$ close to the reflection layer in the WKB case, but in the fullwave case it reaches a maximum at $\zeta = -(L_n/k_o^2)^{-1/3}x = -1.02 \rightarrow x = 0.63W_A$ away from the reflection layer. For the cases studied in the present research, I-mode plasmas where the reflection layers are located close to the LCFS, typical values for the Airy length are $W_A \sim 0.4$cm. The width of the last lobe of the fullwave solution in Figure 2-4 is the definition of the Airy width.

In [54], a numerical study is conducted in which an oscillatory model of the fluctuating density is proposed of the form:

$$\tilde{n}(x) = \tilde{n}_0 e^{-[x-x_0]^2/\Delta^2}\sin\left[2\pi(x - x_0)/\Lambda\right] \tag{2.33}$$

where the fluctuation has a spatial Gaussian envelope centered at x_0 with a width of Δ and has an oscillatory component with wavelength Λ in the same spatial direction

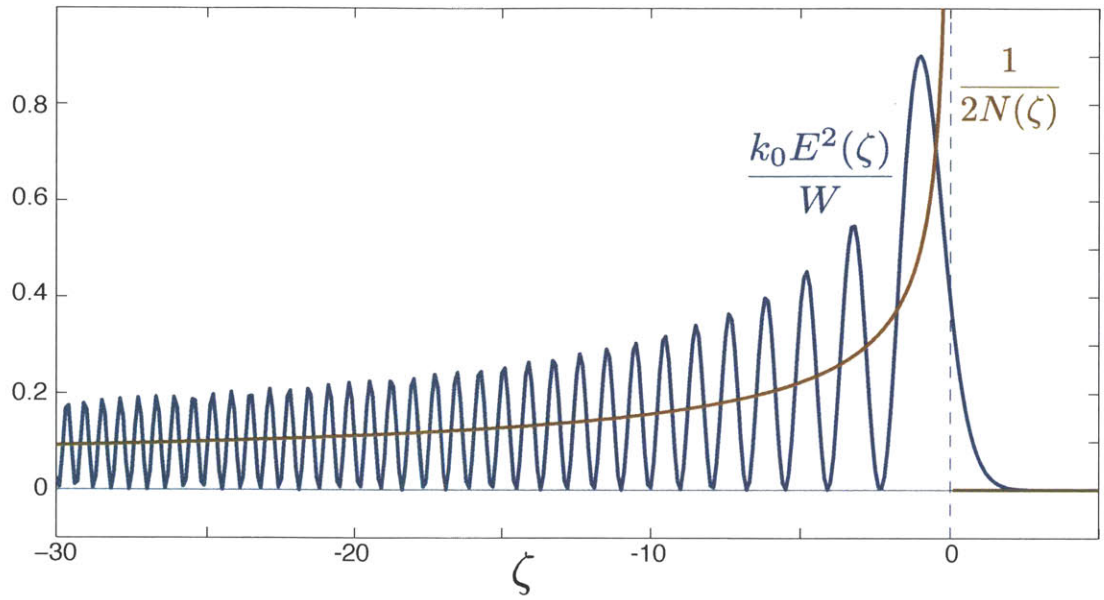

Figure 2-4: Comparison between integrand of the fullwave (blue) and the WKB (red) phase gain equations in a 1D model. Both axes in the plot are non-dimensional quantities. The density profile is assumed to be a linear function of position.

as the probing wave. The center of the gaussian envelope is shifted with respect to the cutoff position of the probing wave, to measure the sensitivity of the wave to the position of the fluctuation. For cases where the fluctuation wavelength is much larger than the free space wavelength of the probing wave, $\Lambda \gg \lambda_0$, the phase fluctuation response of the reflectometry wave is most sensitive to density fluctuations near the cutoff. As Λ is reduced, the position of the envelope peak, x_0, at which the response is maximized, is given by the local Bragg condition:

$$k_\Lambda \sim 2N(x)k_0 = 2k \tag{2.34}$$

where $k_0 = 2\pi/\lambda_0$, $k_\Lambda = 2\pi/\Lambda$ and $N(x)$ is the local index of refraction and, therefore, k is the probing wavelength at a given location, x. For a linear equilibrium density profile, the Bragg condition can be rewritten as: $(x - x_0)/L_n = N^2(x) = [\lambda_0/2\Lambda]^2$, therefore, for $\Lambda \gg \lambda_0$, the Bragg condition is satisfied at $x \sim x_0$, whereas, at $\Lambda = \lambda_0/2$, the location of maximum response occurs at a distance L_n away from the cutoff,

and monotonically increases as λ_0/Λ increases. Therefore, for large fluctuation wave numbers, one cannot assume the signals represent phenomena local to the cutoff location.

As has been presented above, in the 1D model the density fluctuations affect primarily the phase of the returned reflectometry signal. The 1D models are typically lossless, which result in little to no fluctuating component of the amplitude of the perturbed electric field. As is presented in [55], several critical effects are ignored in 1D models, including refraction, diffraction and resonance absorption. Refraction, in particular, plays an important role in reflectometry interpretation, including the experimentally observed effects that density fluctuations have on the electric field amplitude.

2D models

More physically realistic models of the wave-plasma systems incorporate the effects of a vertical or poloidal dimension. The addition of 2D effects is usually reserved for numerical models which will be discussed later in this section; however, 2D analytical models have been proposed which give additional insight into the interpretation of reflectometry fluctuation data.

In [56], the authors assume a 1D linear density profile similar to the one discussed in the previous section, but with a superimposed localized 2D density fluctuation of the form:

$$\tilde{n} = n_0 \exp\left[-ik_x(x-x_0) - \left(\frac{x-x_0}{W}\right)^2\right] \cos k_y(y-y_0) \tag{2.35}$$

where k_x and k_y are fluctuation wavelengths in the parallel and perpendicular directions relative to the propagation of the probing reflectometry wave. The model also assumes a reflectometry wave with a Gaussian envelope distribution close to the transmitting antenna. The authors find that in the 2D picture, the signal scattered from the cutoff region, E_{ret}, has the following properties:

1. For small k_y, the returned signal strength goes as $E_{ret} \propto (L_n - x_0)^{-1/2}$; that is, as the peak of the density fluctuations move toward the antenna plane, the effect of the fluctuations on the reflected signal is to attenuate it, with a similar

weight factor as that of $\tilde{\Phi}$ in the WKB approximation, but on the amplitude of the electric field.

2. For larger k_y, the return signal strength has an exponential dependence of the form: $E_{ret} \propto e^{-k_y^2}$. This implies a very strong loss of signal at high k_y, giving a limitation of poloidal wavenumber for which the reflectometry signal is sensitive to the density fluctuations. As in the 1D models, at high k_y, reflectometry becomes unsuitable for detecting density fluctuations.

In [57], the authors find, through numerical 2D simulations, that the second property becomes less stringent in curved convex plasmas (as in low field side, midplane reflectometry systems) due to a refractive focussing effect. Notwithstanding, for large wavenumbers, reflectometry becomes less sensitive to the fluctuating phenomena. Similar analysis of 2D fluctuation effects has been done[8][9]wherein the fluctuation is modeled as a surface ripple that is moving poloidally, as shown in Figure 2-5a. In the case of a reflectometry signal of frequency ω launched towards the plasma, numerical simulations show that the reflected signal acquires sidebands with frequency shifted by $\vec{k}_y \cdot \vec{v}_{ph}$, where $\vec{k}_y$ is the poloidal wavenumber of the fluctuation and $\vec{v}_{ph}$ is the phase velocity of the fluctuation in the lab frame. As shown in Figure 2-5b, the measured power for the low ripple wavelength case ($\Lambda/\lambda_0 = 1.5$) shows strong sidebands around the zeroth order reflection, whereas the long wavelength case ($\Lambda/\lambda_0 = 40$) shows little to no sidebands. Higher order harmonics of the fluctuation are also present but are substantially reduced in amplitude and are, hence, neglected.

The sidebands propagate at an angle determined by the poloidal fluctuation wavelength $\vec{k}_y$ and are symmetric in amplitude. When the specular, or zeroth order, reflection is not directed towards the receiving antenna due to misalignment or plasma positional shifts, the receiving antenna will detect a given sideband preferentially. This effect can lead to the phenomenon known as phase runaway, wherein the detected signal of the form $S = A(t)\exp[i\phi(t)]$, suffers fluctuations both in $A(t)$ and $\phi(t)$, especially when the amplitude of the density fluctuation is strong ($> 1\%$). Phase runaway is pervasive in laboratory reflectometry systems[58][8],[59],[60] and can be a

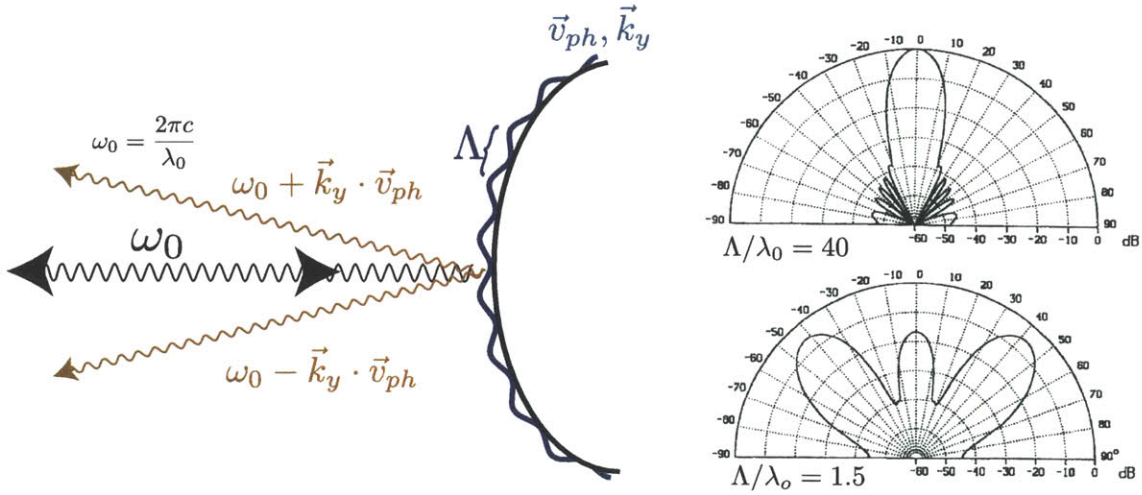

(a) (b)

Figure 2-5: a) A 2D model is used in [8] and [9] where the fluctuation is taken as a rippled surface moving in the poloidal direction. b) Numerical simulations show an acquired sideband for cases where the ripple wavelength is of the same order as the free space reflectometry wavelength. Figure adapted from [9].

major hurdle in interpreting the density fluctuations from the $\tilde{\phi}(t)$ measurements. It is in part due to this effect that much of the interpretation of reflectometry signals study a combination of amplitude and phase changes, such as the homodyne signal: $A(t)\cos(\phi(t))$, or the complex signal: $A(t)\exp[i\phi(t)]$.

Finally, a particularly elegant approach to model the effects of a poloidally distributed perturbation on the reflectometry signal has been developed [61][62]. Assuming a density fluctuation of the form:

$$\tilde{n} \propto \sin(k_y y - \Omega t) \tag{2.36}$$

where k_y is the poloidal wavenumber amplitude, as in Figure 2-5a, and $\Omega = k_y \times |v_{ph}|$, for which a reflectometry signal of the form $E_0 = A\exp[i(k_0 z - \omega_0 t)]$ is reflected, one can model the effects of the fluctuation as a thin screen (no additional distance traveled), through which the reflectometry signal gains a phase component of the form: $a\sin(k_y y - \Omega t)$ where $a \sim \tilde{n}/n_0$. The reflected signal is, therefore, of the form:

$$E = E_0 \exp[i(a\sin(k_y y - \Omega t))] \tag{2.37}$$

which, can be expanded as:

$$E = A \sum_{m=-\infty}^{\infty} J_m(a) \exp[i(mk_y y - \sqrt{k_0^2 - m^2 k_y^2}(z - z_c) + (\omega_0 + m\Omega)t)] \qquad (2.38)$$

where $J_m(a)$ is the m^{th} order Bessel function of the first kind, and z_c is the location of the phase screen. It is informative to observe the effect of a small amplitude fluctuation on the received signal. If we assume $a \ll 1$, all orders of the Bessel functions, except 0,1 and -1, can be ignored. This leads to the following simplified equation:

$$E \simeq A \left[1 + 2ia \sin(k_y y - \Omega t) e^{-i(\sqrt{k_0^2 - k_y^2} - k_0)(z - z_c)}\right] e^{i(k_0(z - z_c) + \omega_0 t)} \qquad (2.39)$$

From this simplified form, we can observe that when $z = z_c$, the amplitude weight factor in square brackets reduces to $[1 + 2ia \sin(k_y y - \Omega t)]$, which, for small a, is only a phase change. As z moves away from the phase screen, the $e^{-i(\sqrt{k_0^2 - k_y^2} - k_0)(z - z_c)}$ term creates constructive and destructive interference effects on the signal, which result in changes in the amplitude. This implies that both the phase and the amplitude of the reflected signal will start to vary far from the reflection layer (such as at the receiving antenna position).

Numerical studies

It's clear from the previous section that as fewer assumptions are taken and the analytical models become closer to a real laboratory plasma-wave interaction, the simple interpretations of the reflectometry signal become less reliable and the analytical models become more intractable. With the rapid advancement of computer power of the last few decades, numerical analyses of the reflectometry systems have become a reliable tool in the understanding and interpretation of the experimental data. There are currently many codes used to study reflectometry data, including advanced simulation codes for 2D imaging reconstructions[63][64] as well as commercial codes that have been adapted for reflectometry analysis, such as COMSOL. Two examples of

particular interest for the research presented, will be discussed below.

A 2D full-wave code was developed to simulate reflectometry data at Alcator C-Mod[65][12], which uses a finite-difference time-domain method. Using this code, the focusing effect that occurs due to plasma curvature, described on page 64, was found. Also, simulations of the quasi-coherent mode showed that for density fluctuation amplitudes of the mode larger than $\tilde{n}_e/n_e \sim 10\%$, phase gain fluctuations, $\tilde{\Phi}$, are not linearly dependent on $\tilde{n}_e/n_e$, consistent with the analytical models previously discussed, wherein, as $\tilde{n}_e/n_e$ becomes large, $\tilde{\phi}$ is no longer proportional to $\tilde{n}_e/n_e$, due to 2D effects that lead to phase runaway. As will be discussed in Chapter 3, reflectometry analysis of the Weakly Coherent Mode (WCM) in I-Mode plasmas, for which $\tilde{n}_e/n_e \approx 16\%$, have shown little phase response, whereas the complex amplitude of the received signals, $A(t)\exp(i\phi t)$, does show the WCM, again consistent with theory and modeling.

Another 2D approach to numerically simulating the effects on reflectometry signals of tokamak plasmas was developed at PPPL[66][67]. The FWR2D code incorporates density fluctuations in wavenumber phase space of the form:

$$\delta n_{\vec{k}} = \sqrt{I_0}\exp\left[-\left[\frac{(\vec{k}-\vec{k}_0)}{\sqrt{2}\Delta\vec{k}}\right]^2\right] e^{i\phi_{\vec{k}}} \tag{2.40}$$

where $\vec{k}_0$ and $\Delta\vec{k}$ are the mean and spectral width of the density fluctuations in 2D $\vec{k}_R$, $\vec{k}_Z$ space, and $\phi_{\vec{k}}$ is a random phase included for each temporal step of the code. The density fluctuations in real space are deduced from the spectral fluctuation distribution through the Fourier transform:

$$\frac{\delta n_{\vec{r}}}{n_{\vec{r}}} = \int (\delta n_{\vec{k}}) e^{-i\vec{k}\cdot\vec{r}} d\vec{k} \tag{2.41}$$

Using the previously defined spectral density fluctuation distribution, the following property of spatial density fluctuations can be shown[66]:

$$\left\langle \frac{\delta n^*_{\vec{r}_1}}{n_{\vec{r}_1}} \frac{\delta n_{\vec{r}_2}}{n_{\vec{r}_2}} \right\rangle = \left(\frac{\tilde{n}}{n_0}\right)^2 \exp\left[i\vec{k}_0 \cdot \vec{r} - \left(\frac{\pi \Delta\vec{k} \cdot \vec{r}}{2}\right)^2 \right] \tag{2.42}$$

where $\vec{r} \equiv \vec{r}_2 - \vec{r}_1$, $<>$ is the ensemble average taken over a large number of iterations (typically > 1000) and $\tilde{n}/n_0$ is the density fluctuation amplitude (not spatially localized). The fluctuations are, therefore, modeled with fluctuation wavenumber, $\vec{k}_0$, and correlation length, $\lambda_{fj} = 2\pi/\Delta\vec{k}_j$, with "$j$" covering each of the two dimensions "R" and "Z", in the acquired ensemble averages. This code has been particularly useful for interpreting correlation reflectometry data, where the received signals from closely separated reflectometry channels are compared and turbulent radial correlation lengths can be investigated. It can also help quantify the amplitude of density fluctuations for low $\tilde{n}_e/n_e$, as will be discussed later in this chapter.

Comparisons between simulations and established fluctuation diagnostics

As can be seen, there are many difficulties involved in the analytical interpretation of reflectometry signals for the understanding of density fluctuations in the plasma. In order to tackle some of the difficulties, numerical models have been developed that simulate the plasma-wave interactions, two of which were discussed above. Experimental comparisons between reflectometry density fluctuation measurements in various machines and simulation codes and/or other well established density fluctuation diagnostics are discussed in this section. These experiments have established the validity of reflectometry as a fluctuation diagnostic, as well as the validity of techniques of analysis developed to better interpret the physical phenomena being studied.

In [10], density fluctuations were studied using both a quadrature phase detection reflectometry system (which can detect both the phase and the amplitude of the received signals), as well as a beam emission spectrometer (BES) in the DIII-D tokamak. The results show good agreement between the BES measurements and reflectometry

measurements for both broadband fluctuations and for coherent MHD type modes, both of which are in the $\tilde{n}/n \sim 1\%$ range in these experiments. For the coherent modes, the authors find that a 1D phase screen model suffices for the interpretation of the reflectometry data. By measuring the phase fluctuations, $\tilde{\phi}(t)$, the density fluctuations at the cutoff layer are estimated as $\tilde{n}/n \approx \tilde{\phi}/(2k_0 L_n)$. The estimated density fluctuation levels are consistent with the BES levels, as can be seen in Figure 2-6, at the location of the reflectometry signal, approximated to $\rho \approx 0.84$ from Thomson scattering density profile measurements (Figure 2-6(a)). For the broadband fluctuations, the authors find that the $\tilde{n}/n \propto \tilde{\phi}$ assumption from the 1D phase screen model doesn't suffice for the interpretation of the density fluctuations. The 2D simulation code FWR2D, described in the previous section, is used to interpret these data, and it is found that the broadband fluctuation level deduced from the reflectometry system is $\tilde{n}/n \sim 0.5\% \pm 0.2\%$, to be compared with the measured BES density fluctuation amplitude for a similar radial position of $\tilde{n}/n \sim 0.33\%$. The spectral shape of the BES signal is found to agree well with the auto-power spectra using the complex signal, $S(t) = \tilde{E}(t)\exp(i\tilde{\phi}(t))$, as can be observed in Figure 2-6(b). The fluctuation levels measured in these experiments are much lower than those measured in I-Mode plasmas in Alcator C-Mod (as will be discussed in the next chapter), but it is useful to note that even for these low fluctuation levels, the simple picture, in which only the phase fluctuations on the received reflectometry signal are required for the interpretation of the density fluctuations at the cutoff layer, is not applicable. Nonetheless. in the case where 2D effects are important (in the broadband fluctuation case), the spectral shape of the complex signal power spectra describes the density fluctuation behavior well compared to BES, which is a more direct measurement of the $\tilde{n}_e/n_e$.

In one of the first comparative studies between reflectometry and Langmuir probe measurements[11], the authors used both of these diagnostic techniques in the CCT and DIII-D tokamaks to observe both broadband and MHD-type modes. It was observed that for a density fluctuation amplitude range of $\tilde{n}/n \sim 10\% - 60\%$, the measurements acquired from the Langmuir probe signals closely match the reflectometry homodyne signal, $S(t) = \tilde{E}(t)\cos(\tilde{\phi}(t))$, which incorporates both the amplitude

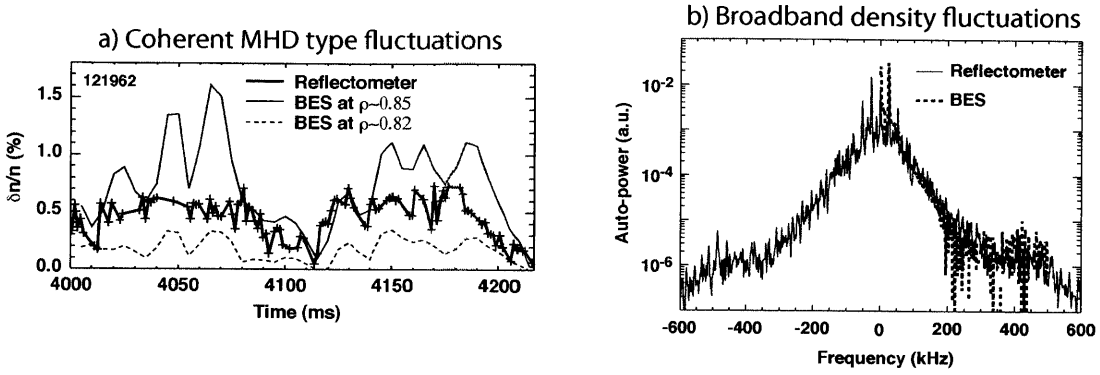

Figure 2-6: DIII-D comparisons of reflectometry data and beam emission spectroscopy (BES) measurements of density fluctuations for (a) coherent MHD type fluctuations and (b) broadband fluctuations. The 1D phase screen model is used to interpret the reflectometry signal in (a), while in (b) the auto-power of the complex signal is compared to the auto-power of the BES at approximately the same radial location. for the broadband fluctuation case, the 2D FWR2D code is used to interpret the reflectometry data. The figures are taken from [10].

of the received wave, $\tilde{E}(t)$, and the acquired phase, $\tilde{\phi}(t)$. As shown in Figure 2-7(a), for low amplitude density fluctuation cases (in H-mode), the power spectrum of the homodyne signal is described by the spectrum of the acquired phase, $\tilde{\phi}(t)$. For these low $\tilde{n}/n$ cases, the experiment follows previous 1D theory, wherein the density fluctuations linearly modulate the phase acquired by the reflectometry system. For higher amplitude density fluctuation cases, like the one shown in Figure 2-7(b), the homodyne signal is mainly characterized by the amplitude of the returned reflectometry fluctuating signals, $\tilde{E}(t)$ ($|E|$ in the reference). In view of the 2D effects discussed in the previous section, it is not surprising that for higher density fluctuation amplitudes, interference and refraction effects modulate the amplitude of the received reflectometry signal, and they dominate the homodyne signal, which in turn correlates well with the Langmuir probe measurements of density fluctuations. As will be discussed in the next chapter, the complex signal of the Alcator C-Mod reflectometry signal, $S(t) = \tilde{E}(t)\exp(i\tilde{\phi}(t))$, is consistently more sensitive to the fluctuating phenomena at the reflection layer than either the homodyne signal or the phase signal. The complex signal has been particularly sensitive to the Weakly Coherent Mode,

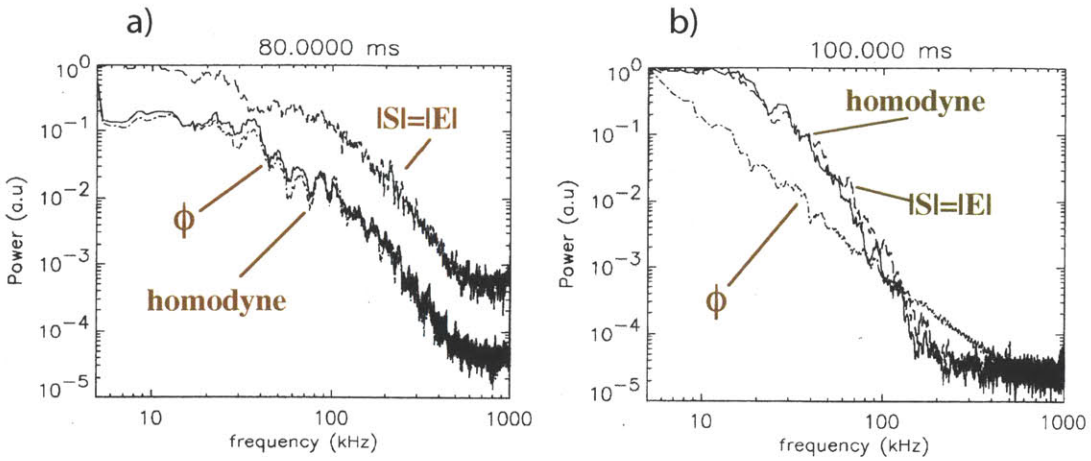

Figure 2-7: Reflectometry signals measured in the CCT tokamak for low amplitude density fluctuations (a) and high amplitude density fluctuation (b). In both cases, the homodyne signal is most consistent with Langmuir probe measurements at the same r/a of the plasma. The figure is taken from [11].

nearly ubiquitous in I-mode plasmas.

In summary, the use of reflectometry for the study of density fluctuations in tokamaks has become widespread and, while quantitative data interpretation is still an ongoing challenge, various qualitative comparisons have shown that reflectometry systems are good qualitative tools for measuring localized density fluctuations non-perturbatively.

2.2.3 O-Mode reflectometry system on Alcator C-Mod

Original reflectometry installation

The O-mode reflectometry system was installed on Alcator C-Mod as an amplitude modulated (AM) reflectometry system[68][51], designed for the acquisition of radial electron density profiles.

The schematic of the AM reflectometry system is outlined in Figure 2-8. The figure omits components which are not relevant for explaining the circuitry. The system consists of two sub-systems, the RF system, which contains all the mm range microwave components, and the intermediate frequency (IF) system, which is used to down-convert the signals to a more manageable frequency range.

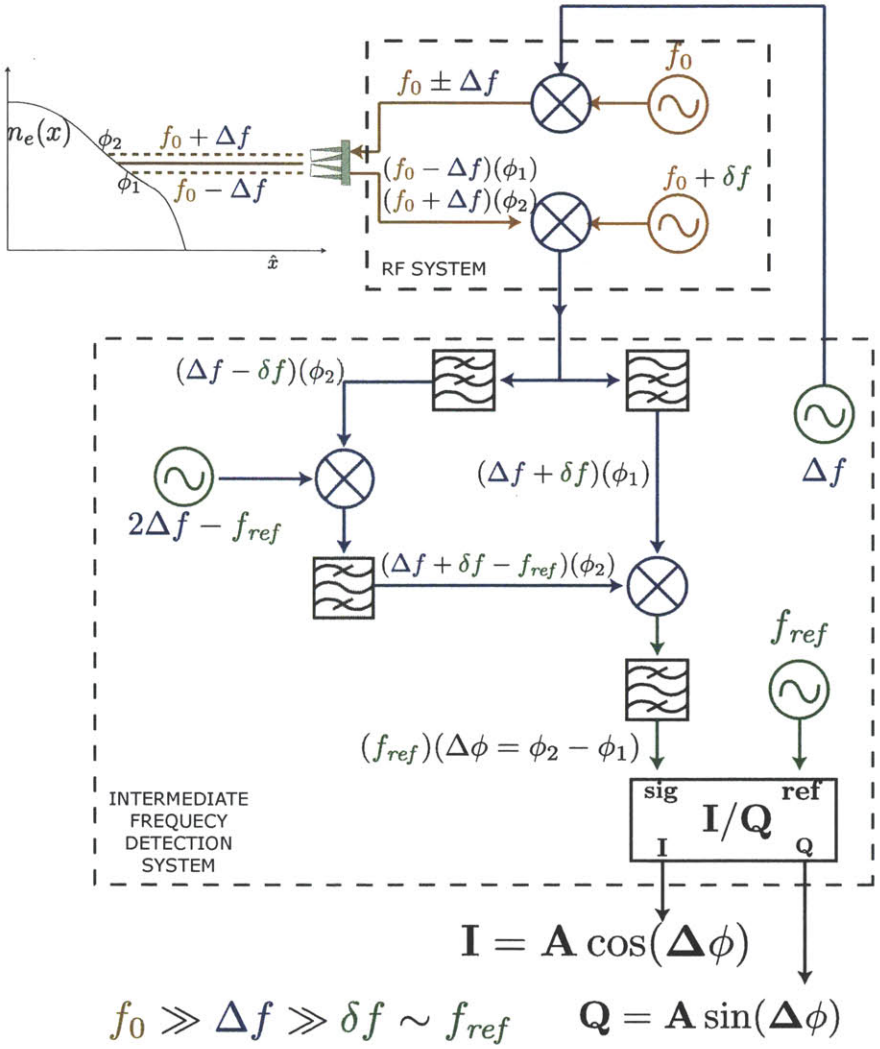

Figure 2-8: The O-mode reflectometry system, as originally installed on Alcator C-Mod, uses amplitude modulated signals to measure radial density profiles. The two sub-systems used are: The RF system which launches 2 closely separated signals into the plasma and an IF detection system which uses a series of down-conversion steps to output the $(A, \Delta\phi)$ information from the plasma through an I/Q detector

In the schematic, the frequencies, as well as the signal paths, are color coded by range: f_0, in red, is in the GHz range (50GHz-110GHz), in blue $\Delta f = 500MHz$, and δf and f_{ref}, in green, are in the tens of MHz (both 30MHz for most cases). The final signals out of the I/Q detector are in the ~1MHz bandwidth range.

The red sources in the RF system are Gunn diode oscillators, both veractor tuned or mechanically tuned to within $\sim 500MHz$. The green coded sources in the IF system are derived from crystal oscillators, which are very stable and are used to ultimately output a signal at frequency f_{ref} containing the plasma information.

Mixers are used to multiply 2 incoming signals, for example, $s_{i1} = A\cos(f_1 t)$ and $s_{i2} = B\cos(f_2 t)$ to create two output signals at the modified frequencies: $s_{o1} = a\cos((f_1 + f_1)t)$ and $s_{o2} = b\cos((f_2 - f_1)t)$. Mixers are used in the AM system to create the amplitude modulation (as the mixer in the transmitting branch of the RF system), as well as to down convert the system to the $\leq 1GHz$ range of the IF system and manipulate the signals to ultimately extract the information from the plasma at a suitable frequency range.

The I/Q detector, a schematic of which is shown in Figure 2-9, has input signals at the same frequency, one of which has a variable amplitude and phase: A and ϕ. The I/Q detector also has 2 outputs: $I = A\cos(\phi)$ and $Q = A\sin(\phi)$.

Finally, the I and Q signals were transmitted to a CAMAC digitizer, which digitized the signals at 5Ksps and had enough memory for 1.64s of data acquisition. Looking again at Figure 2-8, as the two transmitted signals, at frequencies $f_0 \pm \Delta f$, reflect from the cutoff layers in the plasma, each gaining phase information, ϕ_1 and ϕ_2. These signals reflect very close to one another in the plasma, since $f_0 \gg \Delta f$. Using the IF system, the signals are down converted to $< 1GHz$ frequency range and, at the output, a single signal at the frequency f_{ref}, with a phase shift $\Delta\phi = \phi_2 - \phi_1$, is fed to the *sig* input of an I/Q detector. The reference signal from the crystal oscillator is then used for the *ref* input, and an I/Q signal is output which has the amplitude and $\Delta\phi$ information from the plasma.

This is a heterodyne detection system, where a local oscillator (LO) source is used (with frequency $f_0 + \delta f$ in the diagram) to down-convert the original signal to the δf

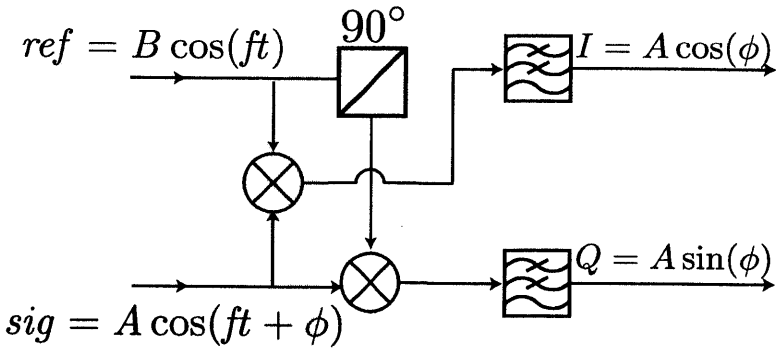

Figure 2-9: The I/Q detector is used to extract amplitude and phase information from a signal as it relates to a reference signal at the same frequency. The schematic shows that it consists of a simple circuits which, at its heart, uses two mixers and a 90° phase shifter, followed by lowpass filters so as to output DC level signals which contain the amplitude and phase information of the input signal.

range, instead of using the same transmitting source to down convert the signal to DC (a homodyne case). Using this method, there is no ambiguity regarding the *sign* of the phase changes due to the round-trip transit through the plasma[69]. The original system consisted of 5 frequency channels, identical to the one described above, at 50, 60, 75, 88 and 110GHz all launched from the outboard midplane.

As was discussed on page 59, by inverting the total phase gain equation derived for reflectometry, an equation for the radial location of the cutoff layers of a given frequency $\omega = 2\pi f$ can be derived[69]:

$$R_c(\omega) = a - \frac{c}{\pi}\int_0^{\omega} \frac{d\phi}{d\omega'}\frac{d\omega'}{(\omega^2 - \omega'^2)^{1/2}} \tag{2.43}$$

where $d\phi/d\omega$ is the phase delay and "a" is an integration constant which sets an offset and must be determined for absolute radial profile measurements.

The $\Delta\phi$ is used, in conjunction with Δf, to estimate a local value for the phase delay in the experimental setup for each of the channels with carrier frequencies f_0:

$$\left.\frac{d\phi}{d\omega}\right|_{f_0} \approx \frac{\Delta\phi}{2\pi(2\Delta f)} \tag{2.44}$$

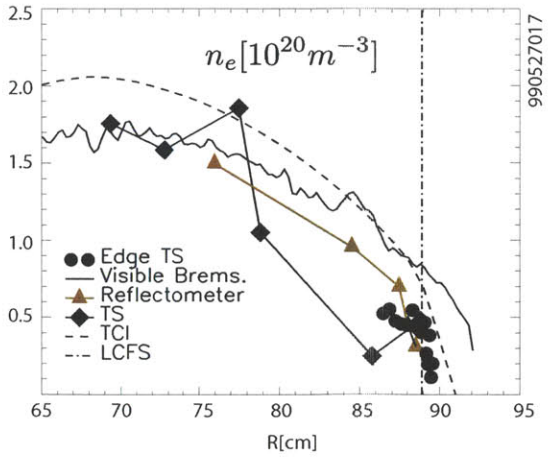

Figure 2-10: Electron density profiles measured using various diagnostics. The reflectometry signal is shown in red. Figure adapted from [12].

This way, the integral can be expanded as a Riemann series with each interval evaluated at each of the 5 fixed frequency channels.

A typical density profile obtained using the O-mode reflectometry system is shown in Figure 2-10, where it can be compared with other density profile measurements.

Initial upgrade to baseband reflectometry

The sensitivity of the reflectometer system to density fluctuations was apparent from the early experiments with the system[15]. These observations led to the first upgrade of the system, for the dedicated study of density fluctuations[5].

The fact that the detected signal comes from a subtraction between the signal from $(f_0+\delta f)(\phi_1)$ and $(f_0+\delta f)(\phi_2)$ results in the cancellation of any coherent information between the two signals. To alleviate this, an upgrade was implemented for the 88GHz channel, which consisted of separating each sideband, and measuring the signals for each. The system was modified in parallel to the AM circuit, that is, the differential signal used for the phase delay estimate was still available. The original modifications are described in detailed in [5] and [12]; the system was subsequently further modified to the circuit presented in Figure 2-11. This schematic shows the 88.5GHz baseband channel, or upper sideband (USB). The 87.5GHz baseband channel, or lower sideband

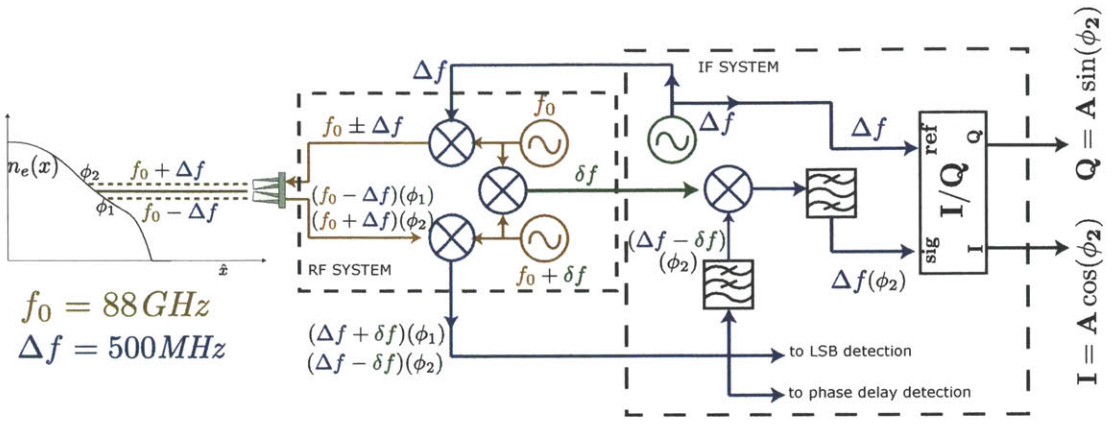

Figure 2-11: The schematic of the upper sideband (USB) detection circuit, installed in parallel of the AM detection system, is shown. The output of the USB and LSB I/Q detectors has the phase and amplitude information gained by each individual sideband without losing coherent information, as occurs with the $\Delta\phi$ signal from the AM output.

(LSB) filtering stage is identical to that of the USB. Also note that while the circuits shown in the references are different from the one shown (which is currently installed), the functionality is identical.

The data acquisition system was also upgraded to higher frequency digitizers, which, at a 1Msps sampling rate, are capable of detecting fluctuating phenomena at up to 500kHz (Nyquist frequency). Due to memory limitations, the sampling time was reduced to 500ms.

By using the sideband detection scheme and with the higher frequency sampling, the upgraded reflectometer was capable of observing and helped characterized the quasi-coherent mode (QCM), signature of the EDA H-Mode[12].

Figure 2-12 shows the autopower signals (proportional to the square of the temporal Fourier transform of the (I+iQ) signal) of the two baseband channels, 87.5GHz and 88.5GHz, as well as the 88AM channel reflecting off the edge of an EDA H-mode plasma. While, in this example, the baseband channels are able to detect the QCM up to its third harmonic, the AM signal can only detect the fundamental of the QCM and at a much lower signal level. This underlines the increased sensitivity provided by the baseband upgrade.

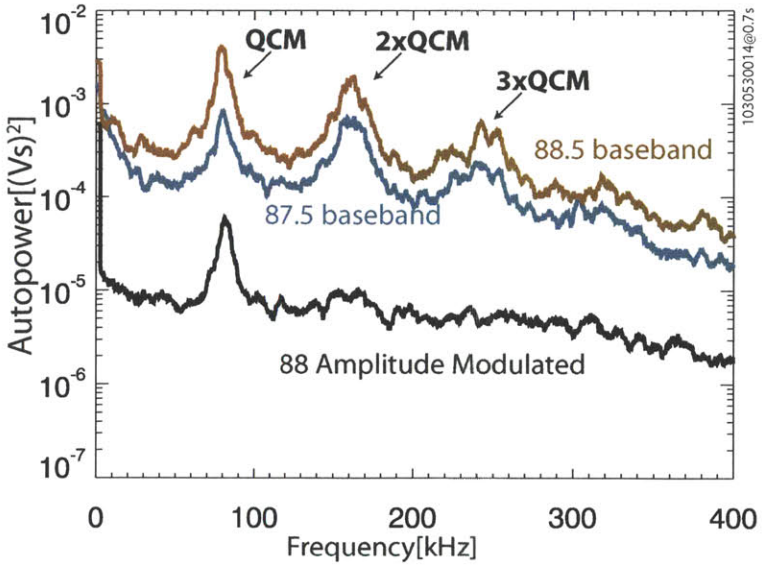

Figure 2-12: The autopower of the baseband signals, 87.5GHz and 88.5GHz, are plotted, as well as that of the 88AM channel. The sensitivity of the baseband channels to the density fluctuations due to the QCM and its harmonics is shown to be much higher than that of the AM signal.

Full upgrade to baseband reflectometry

The successful upgrade of this system, plus the parallel upgrades to the Thomson Scattering system (which will be described later), led to the decision to implement a similar upgrade for the other frequency channels in the system to focus on fluctuation measurements.

Prior to the FY2007 campaign, the remaining 4 channels in the O-mode reflectometry system (50, 60, 75 and 110GHz) were modified to baseband operation[7], that is, the transmitting system is no longer AM modulated before being launched towards the plasma and the detection circuit focuses on the individual phase and amplitude changes in each channel (analogous to the sideband detection scheme of the 88GHz channel). A schematic of the modified system is shown in Figure 2-13.

As can be seen in the figure, the RF stage no longer has the amplitude modulation of Figure 2-8. The frequency difference between the transmitting Gunn diode and the LO source is fed to the IF system and is used, in conjunction with the same

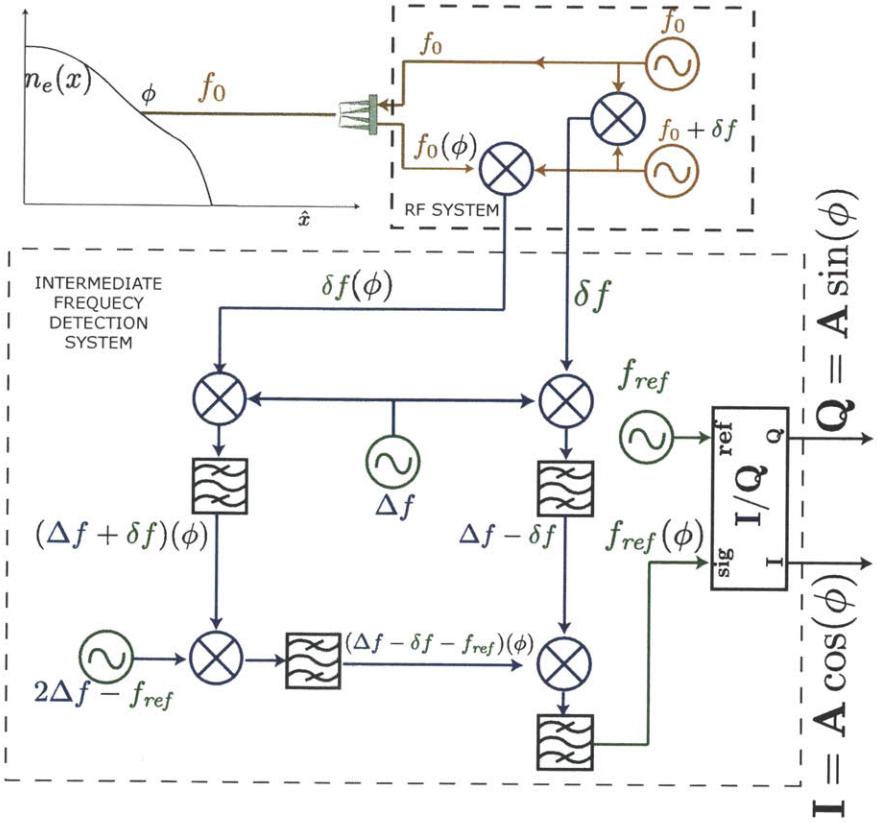

Figure 2-13: The 50, 60, 75 and 110GHz channels were modified to baseband operation, that is, the wave transmitted into the plasma is no longer modulated by Δf as in the AM system (see Figure 2-8) but it is sent as a single frequency which is detected and the amplitude and phase information is acquired through an IF detection stage. The IF stage uses the same crystal oscillators and I/Q detectors as original used.

crystal oscillators and I/Q detectors used for the AM system, to obtain the phase and amplitude changes at f_0 due to plasma transit.

In the figure, the assumptions $f_0 \gg \Delta f \gg \delta f \sim f_{ref}$ are used, so as to omit the use of absolute values for the frequencies in each step. The values that have been used, up to date, are $\Delta f = 500MHz$, $f_{ref} = 30MHz$ and $f_0 = 50, 60, 75, 110$ and $112GHz$[1]. δf of $300MHz$, $1.1GHz$ and $2GHz$ have been used for individual channels, which determine the values of the center frequency and bandwidth of the filtering used for the system. Regardless of the individual details, the baseband upgrade led to full coverage of density fluctuation characteristics for cutoff densities in the $n_e = (0.31 - 1.55)10^{20}m^{-3}$ range, corresponding to 50GHz and 112GHz.

In parallel to these efforts, our PPPL collaborators, led by Dr. G.J. Kramer, with technical support from Dr. C. Kung, installed two high frequency baseband reflectometers at 112GHz and 140GHz, giving the system an increased cutoff density range of $n_e = (0.31 - 2.43)10^{20}m^{-3}$.

Because of the 500ms data acquisition window limit, much of the interesting phenomena from the ~2s plasma discharge were missed. To improve the time interval acquired by the system, as well as increase the digitization rate, a major upgrade to the data acquision system was implemented: The digitizers were upgraded to 2Msps acquisition rate (x2 increase) with a 2s time window (x4 increase). The new digitizers have been essential in allowing detection of fluctuation phenomena occurring during unexpected time segments of the shots (for example, during the current ramp up and ramp down), as well as any phenomena in the 500kHz-1MHz range, since the Nyquist frequency is increased to 1MHz.

One final upgrade to the system has been the installation of a variable frequency channel (VFC), designed in collaboration with the same PPPL team. The VFC has the capability of operating in the 110GHz-140GHz range and is used to probe the core of the plasma.

[1]The 110GHz channel was changed to 112GHz before July, 13^{th} 2010 run day.

Launch configuration

The RF, IF and data acquisition systems for all channels are housed in a metallic rack located approximately 3 meters in front of the A-port horizontal C-Mod port. Within each RF system, all connections use fundamental rectangular waveguides for each set of frequencies, WR-15 for the 50GHz and 60GHz channels, WR-12 for the 75GHz and 88 ± 0.5GHz channels and WR-08 for the 112GHz, VFC and 140GHz channels. Fundamental waveguides are necessary to maintain proper polarization during bends and twists and to feed active and passive components, like mixers, couplers, isolators and amplifiers, which use fundamental waveguide size. To transmit the signals to and from the machine, overmoded waveguides are used (WR-42), since the dB loss/ft of overmoded waveguides is much lower than that in fundamental waveguides. The WR-42 waveguides must be kept straight through the path so as to maintain the same polarization.

The arrangement of the channels in the RF system boards is such that several individual channels share the transmitting and receiving overmoded waveguide paths as well as launch horns. The 50GHz and 60GHz RF system is shown in Figure 2-14a. The signals are combined before being launched into the WR-42 overmoded waveguides, and upon the return from the plasma, the signals are also split and filtered so that the analysis can be done for each channel. The (88 ± 0.5)GHz and 75GHz channels also share a transmission line and antenna system, as do the 112GHz, 140GHz and VFC, the three of which share.

In Figure 2-14b, an in-vessel view of the current antenna configuration is shown. The system uses a bi-static antenna configuration, with pairs of antennas for transmitting and receiving.

One of the major recent changes to the system, which was implemented in collaboration with PPPL, to improve the functionality of the VFC, was the design and installation of the horns used for launching and receiving the high frequency channels: 112GHz, 140GHz and VFC. The details of the previous high frequency horns are described in reference [51]. They were placed inside the vessel and the aperture size

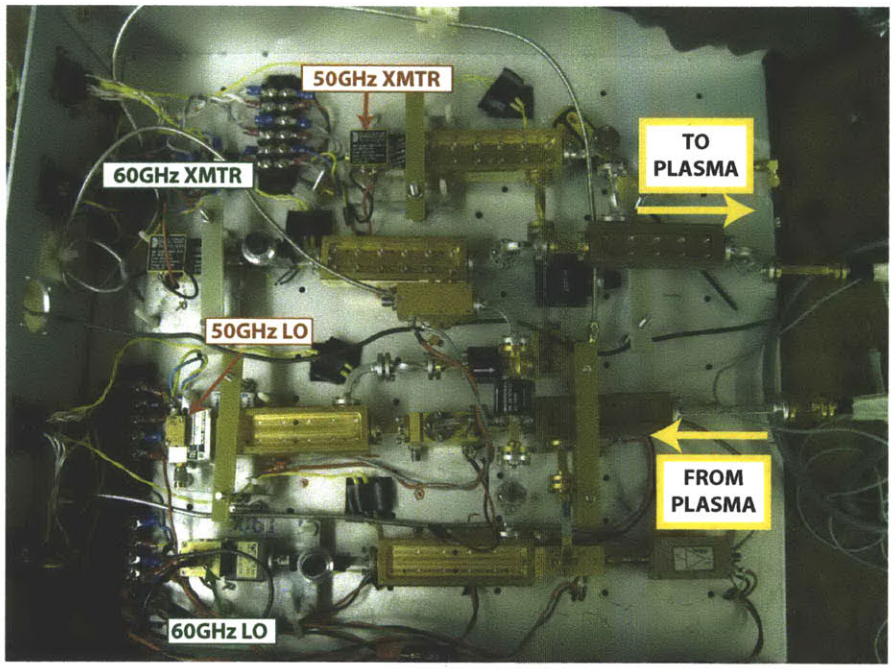

(a)

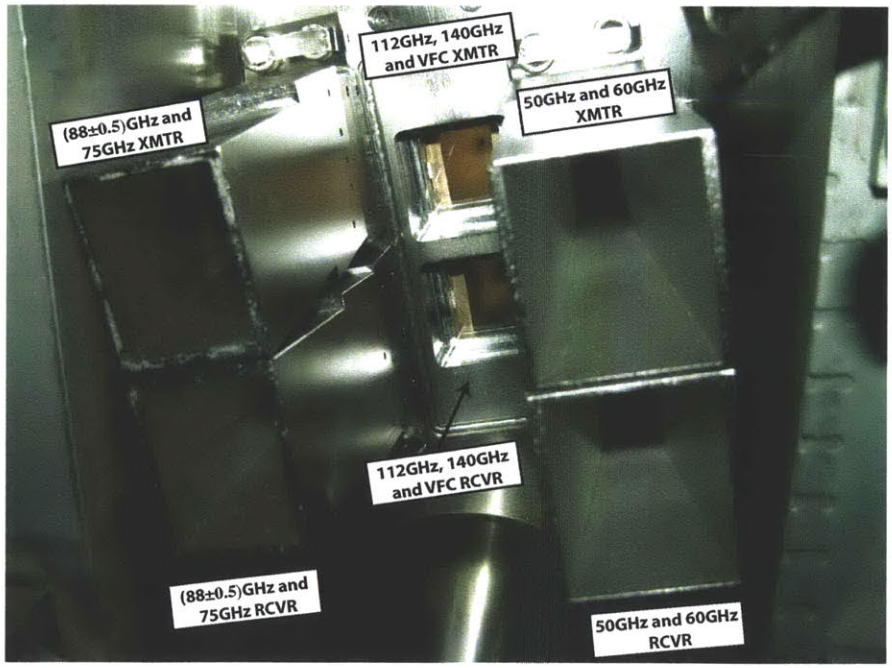

(b)

Figure 2-14: a)Millimeter wave components of the 50GHz and 60GHz systems are shown, where the transmitting Gunn diodes (labeled XMTR) and the local oscillators (labeled LO) are highlighted. Millimeter boards are shared with 50GHz and 60GHz on one, 75GHz and 88±0.5GHz on a second, and 112GHz, 140GHz and the VFC on a third. b)After the signal is transmitted through the overmoded waveguides to the A-port horizontal port, they are launched and received using 3 pairs of pyramidal horns. This picture is taken in-vessel, viewing from the plasma side.

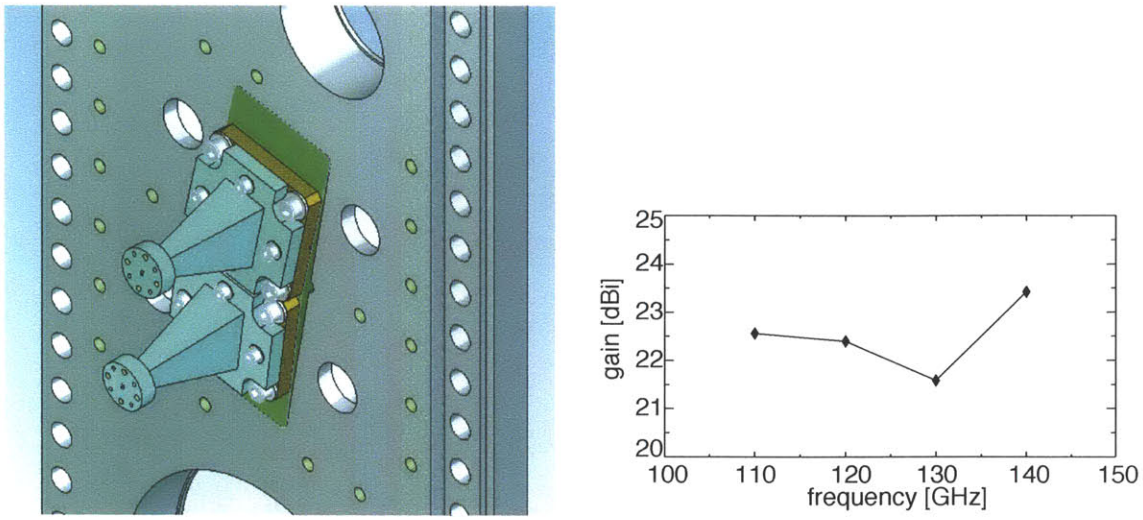

(a) (b)

Figure 2-15: a) The highest frequency channels are launched through a pair of horns that have been designed to optimize the gain for the 110GHz-140Ghz range. b) The calculated horn gain as a function of frequency is flat (to within 2dB) for the whole range.

was chosen to comply with the position of the other four horns. For the redesigned horns, the aperture size was chosen to optimize the horn gain in the 110GHz-140GHz range. The horn dimensions were chosen such that, in the far field approximation, the gain in the 110GHz-140GHz range would be flat, as hown in Figure 2-15b, the calculated gain of the horns using the far field equations[70] are 22.5 ± 1dBi (decibel isotropic). A CAD drawing of the installed pair of horns is shown in Figure 2-15a.

Thomson Scattering density profiles and reflectometry cutoff localization

The baseband upgrade improved the sensitivity of the reflectometry system to density fluctuation measurements, but with the loss of the ability to use the AM capabilities, and thus, make electron density profile measurements. One of the main reasons that this was not a prohibitive hurdle for the development of the baseband system is the use of a Thomson Scattering diagnostic system, specifically the commissioning of an edge TS system which overlaps well with the reflectometry channels, especially for H-mode cases and high density L-modes.

The Thomson Scattering (TS) system consists of two Nd:Yag lasers, each pulsing

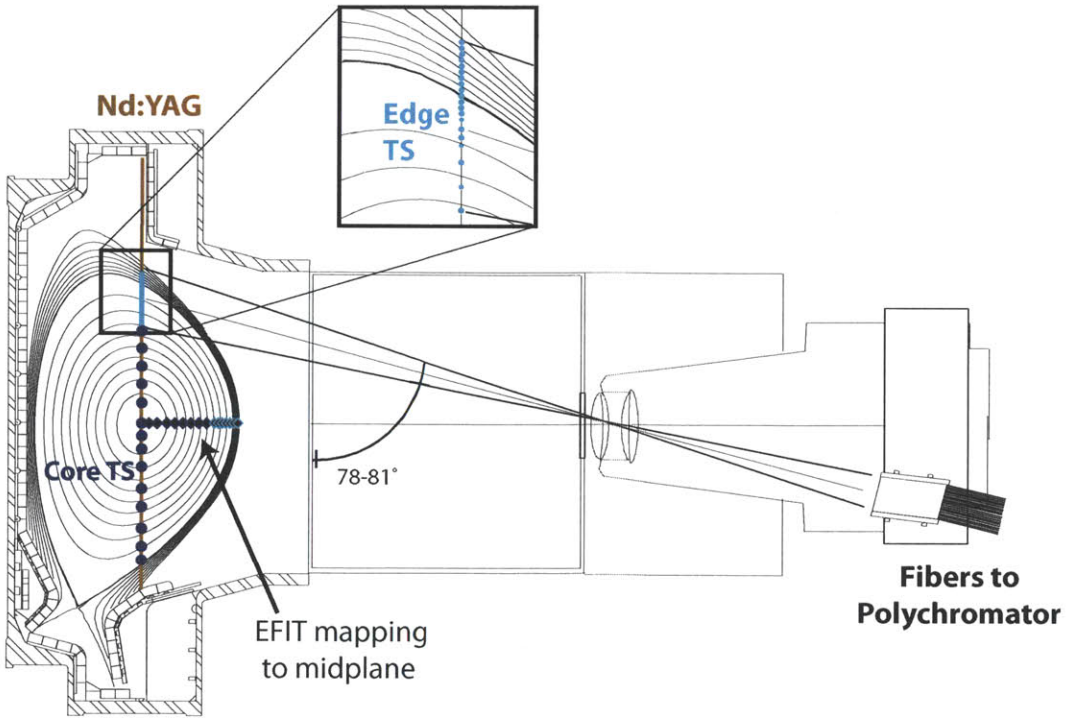

Figure 2-16: The Thomson Scattering system uses vertically launched lasers to excite TS events which are collected and analyzed to deduce the local T_e and n_e throughout the laser trajectory. The measurements are then mapped to the midplane to obtain radial density and temperature profiles. In the figure, the Edge TS system is shown. Figure adapted from [13] and [14].

at 30Hz, launched vertically at $R_{maj} = 0.69m$ into the plasma as shown in Figure 2-16[71]. By setting a 1/2 period shift between the lasers, the TS system can operate at 60 pulses per second.

The Thomson scattered light is collected using a series of fibers, which transmit the signals to an imaging filter polychromator, where they are spectrally separated. As the signals are collected for each spatial channel, the spectral width and intensity are used to derive the local T_e and n_e. The spatial location of each measured signal is then mapped back to the midplane using EFIT flux surface reconstructions, as shown in Figure 2-16.

By using both the edge and the core TS systems, the electron density and temperature profiles can be measured with average spatial resolutions of approximately 1cm

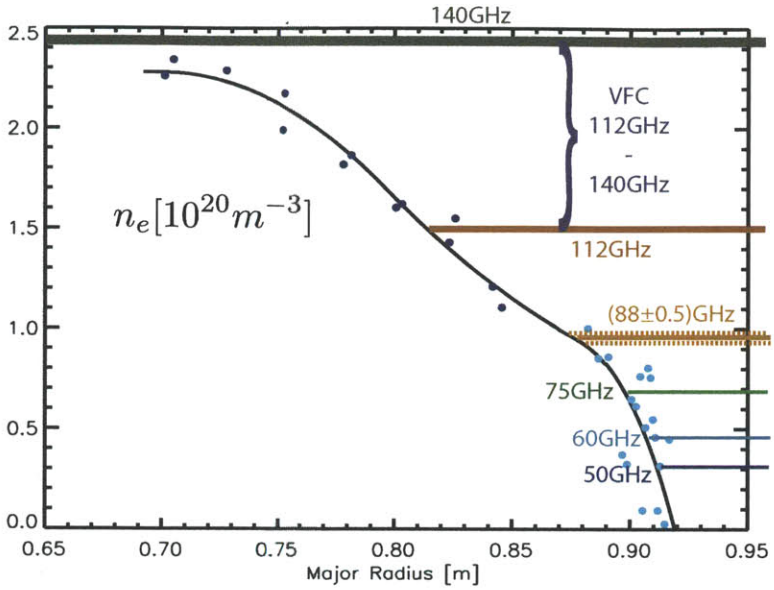

Figure 2-17: Using the TS system, the electron density profiles can be measured. The reflectometry channels currently available for use on Alcator C-Mod are shown for a typical L-Mode. Note that the 88GHz channel is really 2 baseband channels at 87.5GHz and 88.5GHz.

in the core and 1mm at the edge of the plasma. The radial location of the O-mode reflectometer cutoffs can then be inferred from fits to the TS density profiles.

In Figure 2-17, a typical density profile is shown, obtained using the TS system. The dark blue points refer to data measurements from the core TS system, and the light blue points are obtained using the edge system. The x axis is position, mapped to the outboard midplane, as shown in Figure 2-16. The cutoff densities for all of the O-mode reflectometry channels are overplotted on the TS density profile.

While the uncertainties in TS density measurements are approximately 5-10% and arise from various issues, including beam alignment, photon count and absolute calibration, the main radial positioning error comes from the EFIT reconstruction and is of the order of ±5mm. This value is similar to the resolution limit of the reflectometry system, the Airy width[2], $W_A = 0.48(\lambda_0^{2/3} L_n^{1/3})$, for the cases studied here.

[2]see page 58

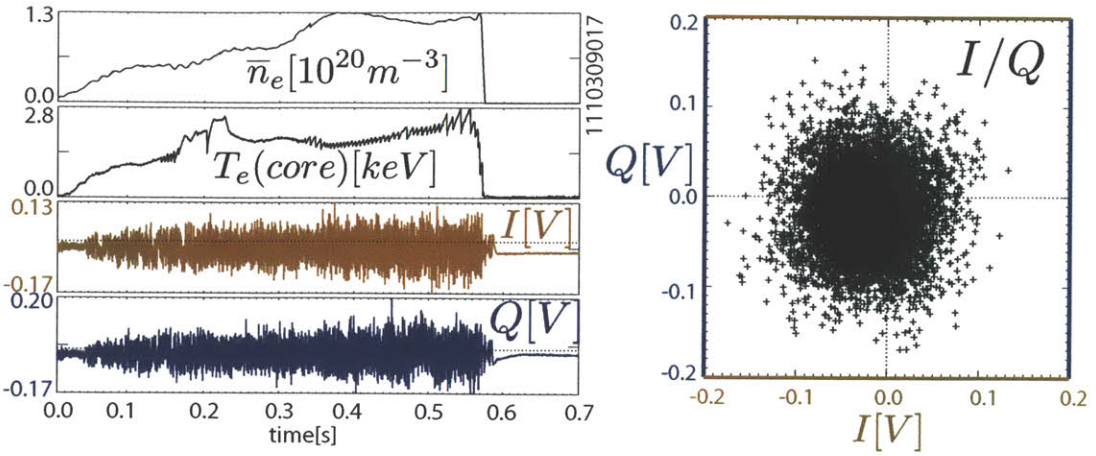

Figure 2-18: The raw I and Q data for the 50GHz channel (cutoff $n_e = 0.31\times10^{20}m^{-3}$) for an L-mode plasma that disrupts at $t = 5.8s$ is shown at left. At right, the I/Q plot is shown.

Reflectometry Data

A sample reflectometry time trace from the 50GHz channel (cutoff location at $n_e = 0.31\times10^{20}m^{-3}$) for an L-mode plasma is seen in Figure 2-18. As the plasma disrupts at t=0.58s, the I and Q signals from the reflectometry channel stop detecting the plasma and "zero out" (although the voltage doesn't exactly reach zero but a constant). The I/Q plot generated from the raw data can be seen on the same figure. As expected, the signal does not generate a perfect circular shell pattern, which would imply only changes in $\tilde{\phi}$ and no amplitude changes, but it fills the area, indicating fluctuations in both amplitude $\tilde{A}$, and phase $\tilde{\phi}$. The figure shows the expected circular pattern, although in many other instances there is elongation, tilt or squareness to the area, which is typically associated with imperfect filtering, parasitic signals or amplifier saturation. Efforts are made to keep these effects to a minimum by monitoring the saturation of IF amplifiers, filtering out parasitic signals, etc.

The center of the I/Q circle is usually not $[I, Q] = [0, 0]$, primarily due to cross contamination of the f_{ref} signal in the f_{sig} signal (see Figure 2-9); this is remedied by shifting the data to the center of a circular fit. The shift is typically implemented when selecting time intervals of approximately 1ms duration before doing spectral

analysis on the data.

As discussed in Section 2.2.2, the fluctuating reflectometry signal carries information of the density fluctuations at the cutoff location (or close to it), in the (A, ϕ) signal, or, more directly, in the (I, Q) signal. The spectral decomposition of the fluctuating signal is useful for separating the type of fluctuations involved by spectral region (e.g. broadband turbulence tends to be in the low frequency range, whereas coherent MHD fluctuations are seen as narrow bands in frequency space). From the (I/Q) output, there are different combinations of signals that can be analyzed, including the $I = A\cos(\phi)$ and $Q = A\sin(\phi)$ signals by themselves (the homodyne signals), the amplitude: $A = \sqrt{I^2 + Q^2}$, the phase: $\phi = \arctan(Q/I)$ and the complex signal: $I + iQ$.

In Figures 2-19a and 2-19b, the autopower of the 5 signals composed of combinations of I and Q defined above are plotted, where the autopower is defined as the amplitude squared of the Fourier transform of the signal:

$$\zeta(f) = \left| \frac{T}{N} \sum^{N} S(t) e^{-2\pi i t f/N} \right|^2 \tag{2.45}$$

where $S(t)$ is the relevant signal for the fluctuations. Note that a vertical offset has been added to the ϕ signal to match the autopower at low frequencies, identical to a multiplicative factor to the signal (since the plots are log-log). These signals can be compared to those obtained in [11], shown in Figure 2-7. On C-Mod, the behavior observed is somewhat similar to the one observed on [11]: At low $\tilde{n}_e/n_e$ levels, as is expected during H-mode, the spectral shape of the ϕ autopower signal is similar to the other 4 signals throughout the whole frequency range, with the homodyne and complex signal follow the "A" trace most closely. As the density fluctuations increase, as in the I-mode case, the shape of the ϕ autopower diverges significantly from that of the other 4 signals (all of which depend on the amplitude, A, of the received electric field), and decrease more sharply for higher frequencies. Note that at $f \sim 200kHz$, all amplitude dependent signals show a spectrally localized increase in fluctuations in the I-Mode case; this is the weakly coherent mode or WCM and will be discussed in

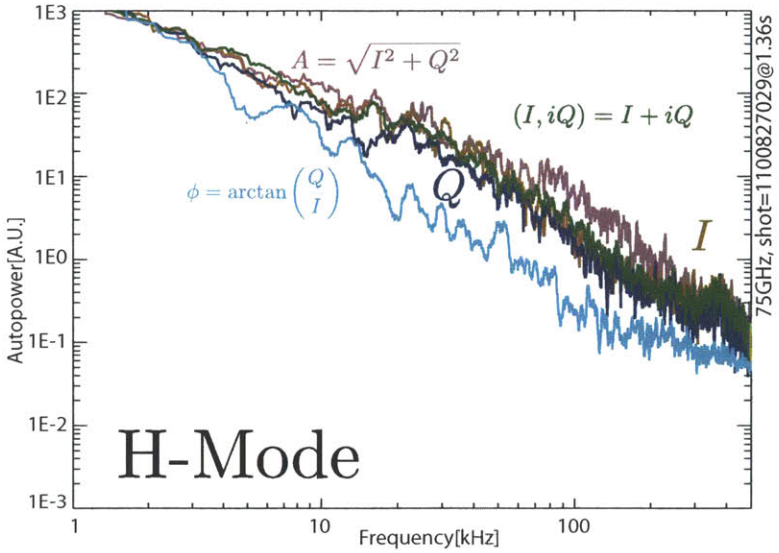

(a)

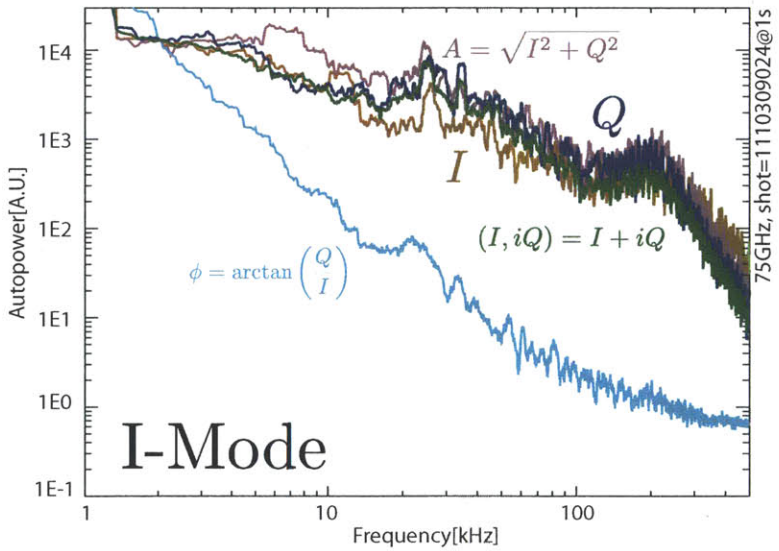

(b)

Figure 2-19: The autopower of different combinations of the I and Q signals are plotted for an a)H-Mode and an b)I-mode. A vertical offset has been added to the ϕ signal to match Autopower at low frequencies. The data can be compared to that obtained in [11], shown in Figure 2-7. On C-Mod, the ϕ signal has a slightly different shape than the others in the H-mode case, but for the I-mode, the sharp decrease of sensitivity of the signal at higher frequencies indicates that for higher fluctuation levels, the ϕ signal loses sensitivity to the phenomena.

depth in Chapter 3.

In this work, the autopower of the complex signal, $(I+iQ)$ will be used for fluctuation analysis. This choice is taken because the complex signal tends to be more sensitive to phenomena like the WCM and because previous analysis of C-Mod reflectometry data has been done using the same signal[5][72]. Nonetheless, similar analysis on the homodyne signals (or on $\tilde{A}$) is suggested for future work as a comparison.

Finally, in order to characterize a complete discharge and dynamically study the changes in fluctuations throughout, an *autospectrum* is used. The autospectrum is constructed by dividing the total acquired time interval into smaller windows and calculating the autopower for each sub-window. The data are then displayed in a 3D plot where the x and y axes are the time (typically determining the center of each sub-window) and the spectral frequency, respectively, and the autopower at a given (t, f) is shown in color (or some other 3D display, like contours). A sample autospectrum, from the 110GHz channel, for a plasma undergoing an I-H mode transition followed by an H-L mode transition is shown in Figure 2-20. As each transition occurs during the shot, the changes in fluctuations can be easily visualized in the autospectrum.

2.3 Additional fluctuation diagnostics

2.3.1 Gas puff imaging

The gas puff imaging diagnostic (GPI) is based on the idea that the local emissivity, ϵ, of the plasma due to line emission from neutral deuterium or helium can be expressed as being proportional to[22]:

$$\epsilon \propto n_e^{\alpha_n} T_e^{\alpha_T} \tag{2.46}$$

for most cases, $\alpha_n \gg \alpha_T$, hence, the emissivity signal is effectively proportional to a power of n_e.

The outboard midplane GPI system consists of an array of 9x10 in-vessel optical fibers focusing on a 2D viewing area of 4cm×4.4cm straddling the LCFS at the outboard midplane, as shown in Figure 2-21. By using optical interference filters with

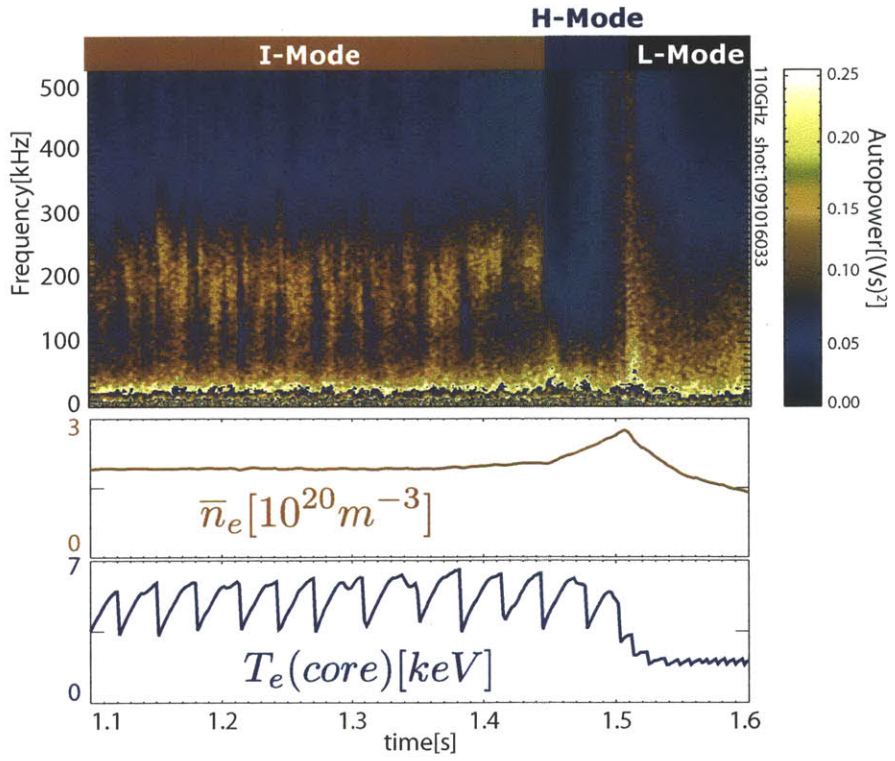

Figure 2-20: The autospectrum of the complex signal $(I+iQ)$ for the 110GHz channel is shown from a discharge that exhibits an I-L and then an L-H transition. The changes in fluctuations are apparent in the autospectrum.

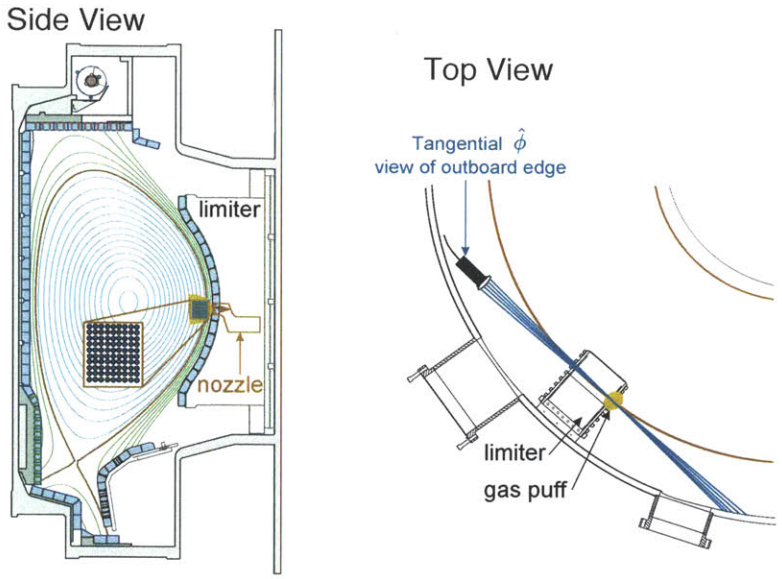

Figure 2-21: The viewing area of the GPI system is a 2D array localized at the outboard midplane. The line integrated brightness measurements can be spatially localized by puffing D_2 or He gas at the location shown in the "top view". The signals are then a local measurement of the emissivity which, in turn, contains the local n_e information.

center wavelengths at ~656nm and ~587nm, one can selectively study the deuterium Balmer-α light or the HeI ($3^3D \rightarrow 2^3P$) line respectively. After the filters, the light is fiber-optically coupled to a set of avalanche photo-diode (APD) detectors.

While the integrated brightness profiles can be used for background emissivity profiles (which will be discussed in detail in Chapter 4), a gas puff, injected at the midplane next to the A-B limiter, is used to localize the measurements. As a gas cloud of D_2 or He is puffed into the plasma, the signal is dominated by the line emission from the gas cloud, and the brightness signal can be interpreted as being primarily emitted at the gas cloud location. A schematic of this is seen in the top view in Figure 2-21.

Data from the APDs are digitized at 2Msps, and spectral analysis, similar to that done for the O-mode reflectometer, can be performed. The 2D diode array gives the GPI system the ability of measuring both frequency and wavenumber decomposition of the data, by applying both temporal and spatial Fourier analysis, generating $k - f$ spectral plots. In Figure 2-22, the $k - f$ spectral decompositions from L-mode,

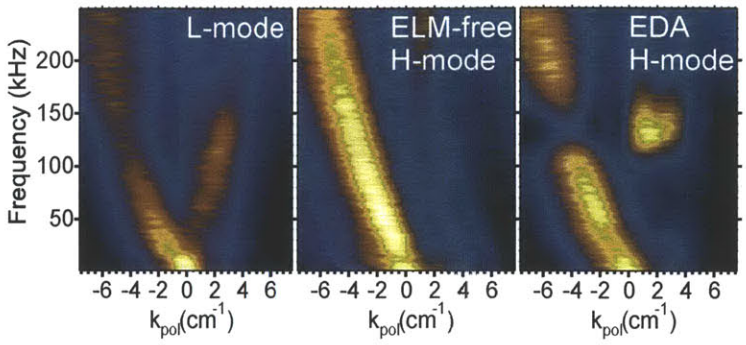

Figure 2-22: By using poloidal columns of GPI views, a $k - f$ diagram can be constructed that displays both the frequency information of signal fluctuations, but also the k_θ decomposition. This is essential in characterizing wavelike phenomena since it can display the frequency as well as the poloidal wavenumber of the fluctuations. In the EDA H-mode, for example, the QC-mode can be observed at $k_\theta \approx 2cm^{-1}$ at a frequency of $f \approx 130kHz$, hence, its phase velocity in the lab frame can be calculated to be: $v_{ph,\theta} = 2\pi f/k_\theta \approx 4.08km/s$. Figure from [22].

ELM-free H-mode, and EDA H-mode plasmas have been performed on data from a column of diodes located radially close to the edge of the plasma and ranging vertically from $z = -5.4$cm to $z = -1$cm. The temporal FFT of the data leads to the frequency decomposition (vertical axis) and the spatial FFT determines the poloidal wavenumber k_θ of the detected fluctuations (horizontal axis)[22].

The localized measurement capability of the GPI system, as well as it position at the outboard midplane, make the GPI system a workhorse diagnostic for the wavenumber characterization of edge fluctuations on Alcator C-Mod.

2.3.2 Phase contrast imaging

The phase contrast imaging (PCI) system is a modified interferometer, optimized for the detection of density fluctuations.

A CO_2 laser is radially expanded to span $R_{maj} = 0.64cm - 0.73cm$ and is vertically launched into the plasma as shown in Figure 2-23a after which it is collected by 32 independent detectors[73][74]. As the laser crosses the plasma, it gains a phase, $\tilde{\phi}$,

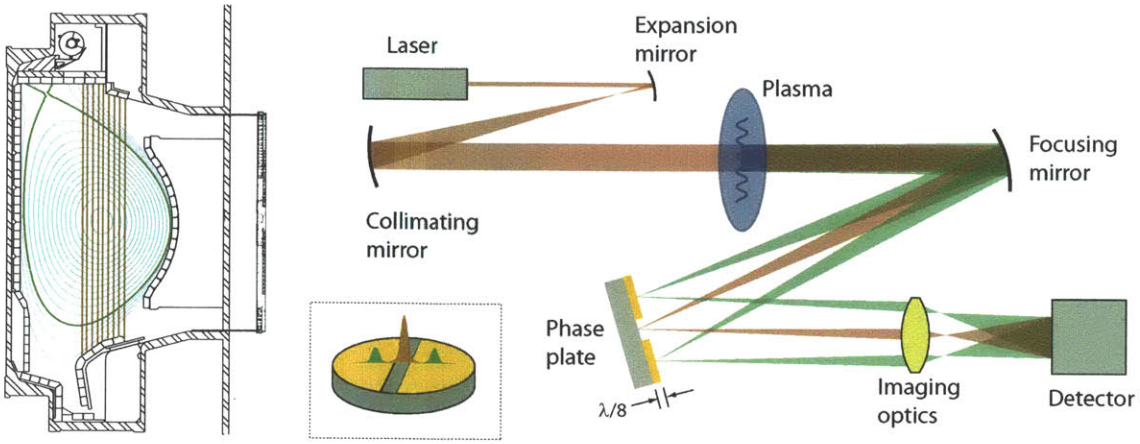

(a) (b)

Figure 2-23: a)The Phase Contrast Imaging (PCI) system detects line integrated density fluctuations across 32 vertical chords that encompass the plasma core. b) By using a phase plate the gives the unperturbed component of the laser signal a $\lambda/4$, hence, a $\pi/2$, phase shift, the intensity of the signal becomes dependent of the phase gained through the laser path which, in turn, is proportional to the line integrated $\tilde{n}_e$. Figure from [74].

proportional to the fluctuating density:

$$\tilde{\phi} = -r_e \lambda_0 \int \tilde{n}_e(x,z) dz \ , \tag{2.47}$$

where, $r_e = e^2/(4\pi\epsilon_0 m_e c^2)$ is the classical electron radius and $\lambda_0 = 10.6\mu m$ is the free space wavelength of the CO_2 laser used. The line integral is taken along the vertical path of the beam through the plasma. The fluctuations in the phase of the signal are, therefore, proportional to the line integrated density fluctuations.

The introduction of a phase plate, shown in the figure, introduces a $2 \times \lambda/8$ phase shift (equivalent to multiplying by $e^{i\pi/2} = i$) to the *unperturbed* component of the signal and, using focusing optics, the signals are recombined to form a single signal. The use of the phase plate modifies the total signal:

$$E = E^{(0)} + E^{(1)} = E_0(\mathbf{i} + i\tilde{\phi})e^{-i\omega_0 t} \rightarrow |E|^2 \approx |E_0|^2(1 + 2\tilde{\phi}) \ . \tag{2.48}$$

The variations from the unperturbed intensity of the measured beam are, therefore,

linearly proportional to changes in phase, which are proportional to $\int \tilde{n}_e dz$.
The radial separation between the channels provides the capability to measure k_R of the fluctuations within the $0.58cm^{-1} < k_R < 50cm^{-1}$ range, and a 5Msps data acquisition digitization rate provides a frequency bandwidth of up to $f = 2.5MHz$.
The line integral nature of the diagnostic is an inherent challenge for the localization of the modes, but if there is additional information regarding the vertical position of the fluctuations along the path of the laser (e.g. if we know that a given perturbation is localized close to the edge of the confined plasma), the system can be used, as with the GPI, for spectral characterization of fluctuations and determination of short wavelengths.

2.3.3 Electron cyclotron emission diagnostic

As the electrons gyrate around the magnetic field, they emit *electron cyclotron emission* at the local cyclotron frequency, Ω_e, and its harmonics. In the region of emission, the plasma is optically thick so it acts as a *black body* for which the intensity, as a function of the emitted frequency ν, is of the form:

$$I(\nu) = \frac{\nu^2}{c^2} \frac{h\nu}{e^{h\nu/T} - 1} \tag{2.49}$$

where h is the Plank constant. Therefore, the intensity emitted has a shape dependent on the local temperature. Since the 2nd harmonic of the X-mode ECE radiation can propagate out of the plasma without encountering a cutoff condition and can be detected at the outboard side of the plasma, the temperature at the 2nd harmonic can then be measured[69].
There are several electron cyclotron emission diagnostics on Alcator C-Mod[75][76], including 2 grating polychrometer (GPC) diagnostics which provide high time resolution measurements of the local electron temperature and are used as workhorse T_e profile diagnostics.
A high resolution, heterodyne ECE system, installed in collaboration with the *Fusion*

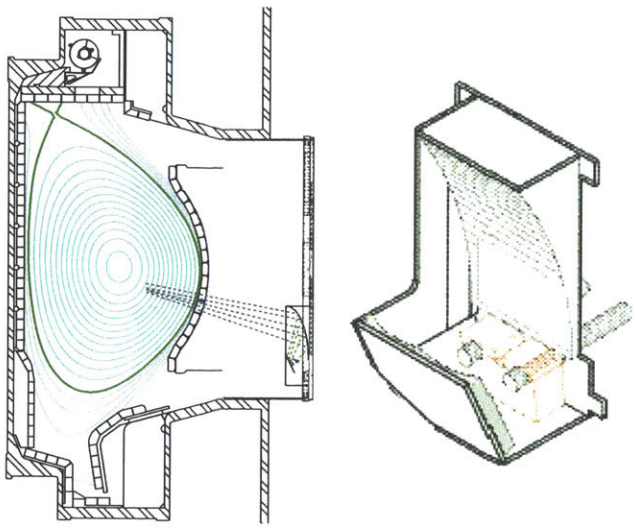

Figure 2-24: The high resolution ECE system, installed in collaboration with FRC, can provide local measurements of spatial resolution of $< 1cm$ at the edge of the plasma. The time resolution of the system is high enough to conduct spectral analysis of signal to up to 100s of kHz. Figure adapted from [77].

Reseatch Center group, uses 32 detector channels covering the 234-306GHz frequency range to give a resolution of less than 1cm between channels[77]. The system optics are located inside the vessel in the lower outboard side of the plasma, as shown in Figure 2-24, with the lines of sight of the system directed towards the magnetic axis and, therefore, mostly perpendicular to the flux surfaces.

By the use of video bandwidth filtering of 1MHz and a data acquisition system with a 2MHz digitization rate, the data acquired by this system can be spectrally analyzed to detect phenomena at 100s of kHz, which is not available with the T_e profile measurement ECE systems. Also, due to its high spatial resolution, local $\tilde{T}_e$ measurements have been obtained at the edge of the plasma and will be discussed in Section 3.3.2.

2.3.4 Fast magnetic pick-up coils

One of the most straightforward fluctuation measurements is that of the magnetic fluctuations at the edge. By using sets of coil solenoids, 13mm long and 4mm in

diameter, as shown in Figure 2-25(a), the voltage induced due to a time varying magnetic field, $\vec{B}$, can be calculated as $V = \vec{A} \cdot \dot{\vec{B}}$, where $\vec{A}$ is the total area enclosed by all coil turns, pointing along the coil axis[78][79].

There are currently a total of 66 operational probes arranged in poloidal and toroidal arrays at the outboard side of the plasma (see Figure 2-25(b) and (c)), aligned so as to measure $\dot{B}_\theta$. The poloidal and toroidal arrays give the fast magnetic coils the unique capability of measuring the poloidal (m) and toroidal (n) mode numbers for the fluctuations calculated by measuring phase differences between coils. The toroidal and poloidal separations of the coils also enables the detection of spatial variations in fluctuation intensities, as will be discussed in Section 3.3.2.

Finally, measuring the magnetic components of fluctuating modes helps to discriminate between electrostatic and electromagnetic types of fluctuations. If a particular mode is detected by the magnetic coils, the mode is not purely electrostatic, a fact that helps characterize the various modes that are detected.

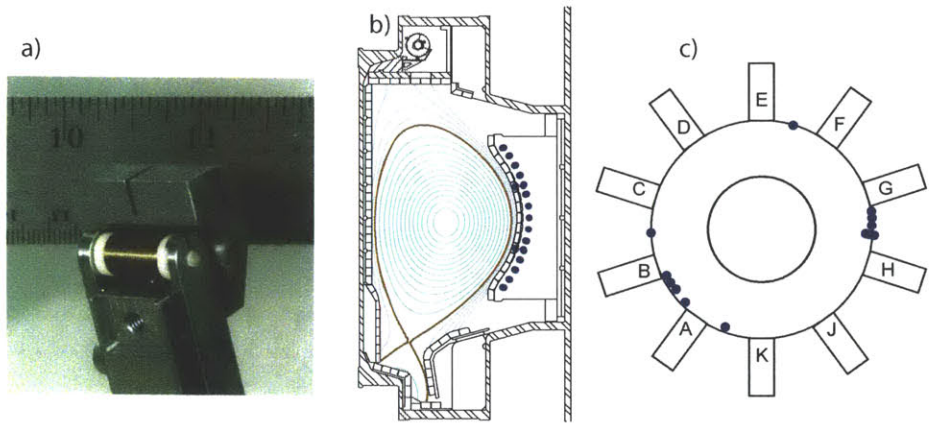

Figure 2-25: a) The fast magnetic coils consist of simple wound solenoids aligned in the $\hat{\theta}$ direction. By Faraday's law, a voltage is induced in the coil proportional to the fluctuating magnetic flux within the coil. There are currently 66 operational coils (shown in blue) distributed (b) poloidally and (c) toroidally around the outboard wall of Alcator C-Mod.

Chapter 3

The I-Mode regime

3.1 History of the I-Mode

The dependence of the L-mode to H-mode threshold power on the ∇B drift direction was quickly observed after the discovery of the H-Mode[80], and has been widely seen on many tokamaks[81][16][1]. The P_{L-H} scaling law shown in Equation A.6 refers to only L-H transitions in the *favorable drift direction*, that is, when the $\vec{B} \times \nabla B$ direction, or ∇B drift direction, is pointing towards the main X-point of the plasma. For many tokamaks, including Alcator C-Mod, the power needed to transition to H-mode is approximately 2 times larger in the *unfavorable drift direction*, that is, when the ∇B drift direction is pointing away from the main x-point, than in the *favorable drift direction*.

On Alcator C-Mod, it was observed that the L-modes preceding the L-H transition in the unfavorable drift direction featured high edge temperatures ($T_e > 200eV$), leading to enhanced values of the energy confinement coefficient $H_{89} \equiv \tau_E/\tau_{89} > 1.1$[15] as seen on Figure 3-1a. These initial measurements lacked sufficient time and space resolved density and temperature profiles to determine the edge barrier characteristics of the regime, nonetheless, it became clear that unfavorable drift direction L-modes close to L-H transitions exhibit atypical characteristics compared to the favorable drift direction L-modes. On ASDEX Upgrade (AUG), similar characteristics were found in the unfavorable drift direction prior to L-H transitions [16]. On AUG, this

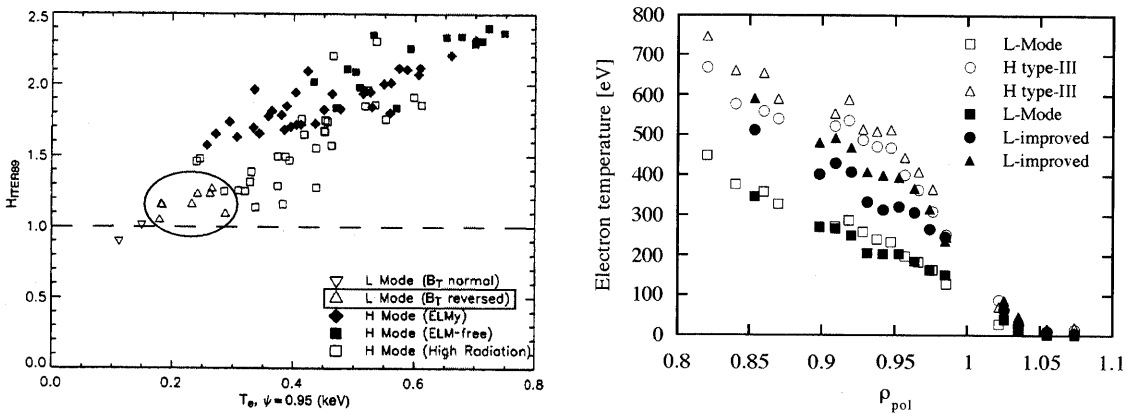

(a) (b)

Figure 3-1: The L-mode before an L-H transition in unfavorable drift direction plasma was found to have remarkably high edge temperature and energy confinement on Alcator C-Mod and on AUG. a)On C-Mod, the L-modes prior to L-H transitions show high $H_{98} > 1.1$ and edge temperatures above 200eV(adapted from [15]). b)On AUG, the unfavorable drift direction L-mode prior to the L-H transitions was named the *Improved L-Mode* and it featured H-mode like temperature profiles (figure from [16]).

regime was labeled *Improved L-Mode*, and also featured edge temperatures above 200eV. Temperature profiles in the improved L-mode regime were measured to be qualitatively similar to those in the H-mode (see Figure 3-1b), with 80% of the energy confinement of the H-mode. Nonetheless, this regime could only be sustained for about 3-5 τ_E.

On C-Mod, the unfavorable drift direction L-H transitions were initially studied because it was observed that they could develop the typical characteristics of the H-mode on a longer time scale than the favorable LH transition, hence facilitating a study of the transition dynamics. By 2007, it had been identified that the L-H transition in the unfavorable drift direction happened in two phases[82][1], first a rise in temperature, followed by a rise in density, concomitant with a decrease in D_α. As shown in Figure 3-2, during this intermediate phase, the density stayed constant while the edge temperature rose. As was the case for the *Improved L-modes* in AUG, these two-phase transitions occurred transiently, lasting up to 3-5 τ_E ($\sim 1\tau_E$ in Figure 3-2).

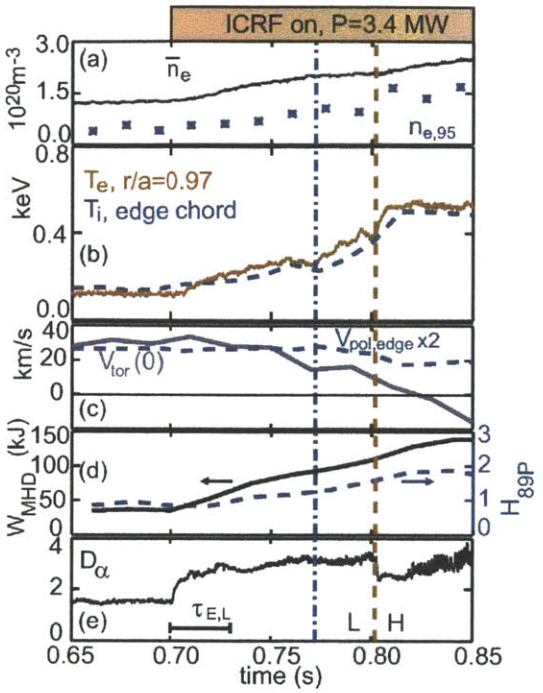

Figure 3-2: The two-phase transition was observed on C-Mod which showed a rise in edge temperature and stored energy ((b) and (d)) while maintaining constant density (a). The D_α is seen to stay high during the intermediate phase and decrease as the density rises (e). Figure from [1].

Through a more systematic approach, wherein the auxiliary power was slowly ramped at constant I_p, the intermediate phase was sustained in steady-state for longer than 10 τ_E[2]. The study also showed the ubiquitous presence of changes in edge fluctuations, as well as the development of an edge electric field well. The fact that the two-phase transition could be sustained to steady state, as well as its unique global characteristics and edge fluctuations, led to distinguishing it as a separate regime, the *I-mode*.

Following the publication of a review of the characteristics of this novel regime, [3], numerous experiments on C-Mod have been devoted to the physics of the I-mode as well as its accessibility, the results of which will be presented in the next section. Recently, interest in the study of the I-mode has also been renewed at AUG[83], and joint C-Mod/AUG experiments are currently being pursued. The fact that the I-mode

can be accessed using neutral beam injection heating is a welcomed development for the possibility of accessing this regime in non-ICRF auxiliary heated plasmas. Joint experiments are also being planned with DIII-D to search for this regime, thereby expanding the parameter space for its study.

3.2 General characteristics of the I-mode

As mentioned in the previous section, the main characteristics of the I-mode regime are the increase in energy confinement due to the presence of a thermal barrier at the edge of the plasma but, combined with no formation of a particle barrier, leading to low particle and impurity confinement, as shown in Figure 1-7.

3.2.1 I-Mode Accessibility

Typical operation on Alcator C-Mod has both I_p and B_T in the clockwise direction (viewed from above), hence the $\vec{B} \times \nabla B$, or ∇B drift, direction is pointing downward. The unfavorable drift direction in this configuration is, then, upper single null, (USN), as shown in Figure 3-3(a).

This is the configuration in which the I-mode was discovered on C-Mod and it has been the most widely used to access the regime. This configuration has several advantages, like the wide range of accessible upper triangularity, δ_u, as well as the use of a cryopump[84] located in the open upper divertor, but it also has problems of power handling because of leading edges in slots used by the cryopump, and the open flat-plate geometry of the upper divertor.

By reversing the directions of I_p and B_T, the unfavorable drift direction topology is the more standard LSN shape, as seen in Figure 3-3(c). Note that both I_p and B_T must be reversed in order to maintain the same helicity of the magnetic field. In this configuration, there are the advantages that the lower divertor is equipped with a large suite of divertor diagnostics, that the Edge Thomson Scattering system has improved spatial resolution (see Figure 2-16) and that the lower divertor is also

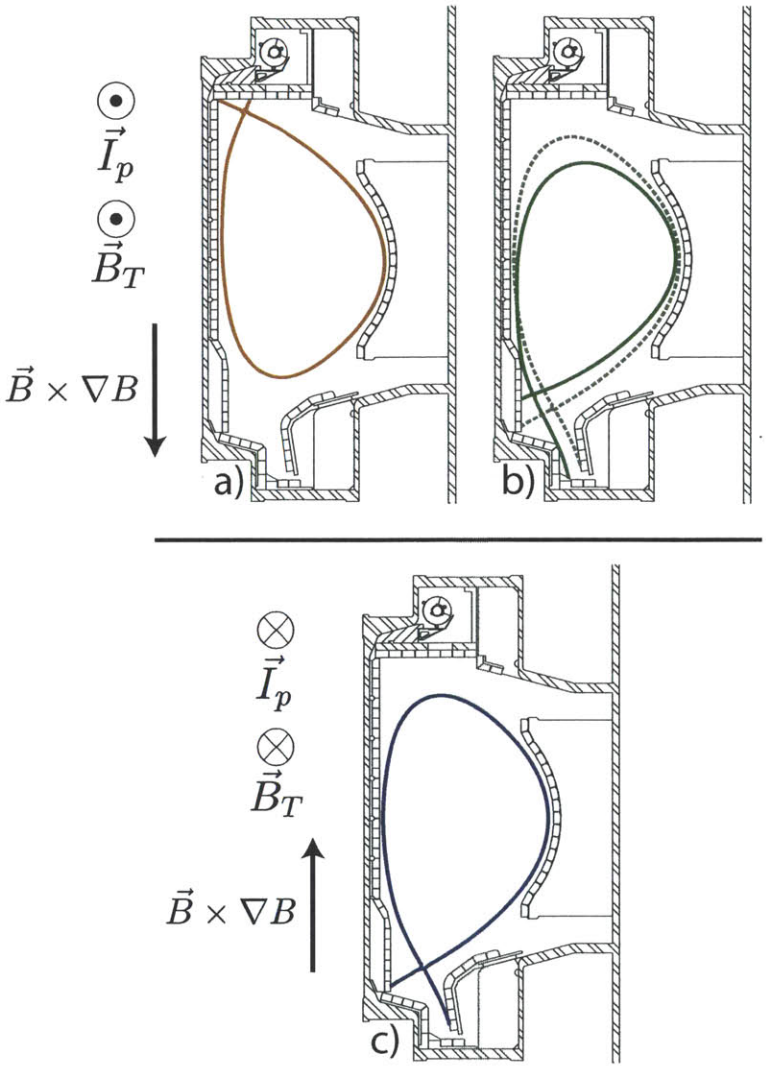

Figure 3-3: The I-mode regime has typically been accessed on Alcator C-Mod in the unfavorable drift direction in normal field (I_p and B_T clockwise when viewed from above) as seen in (a). By reversing the fields, the unfavorable drift direction is achieved using the more conventional LSN topology, (c). Finally, by using an exaggerated δ_l topology in normal field configuration, similar to the shape used for ELMy H-modes, I-modes have also been accessed (b).

optimized for power handling, with its closed, vertical plate design. I-Mode operation in reverse field, LSN shows a widening of the P_{ICRF} window between the L-I transition and the I-H transition, as compared to that of the normal field, USN case. This development has significantly widened the space of operation of this regime, making it more attractive as a potential regime for next step tokamaks.

While, the I-mode has been generally obtained in the unfavorable drift direction configuration, it has also been possible to access it in the favorable drift direction by operating with exaggerated lower triangularity shape ($\delta_l \sim 0.8$), shown in Figure 3-3(b). Note that this configuration is also used to access ELMy H-modes on C-Mod as described in Section A.3.1. For access, these I-modes require lower auxiliary heating power (as expected from being in the favorable drift direction), sometimes marginally appearing in ohmic plasmas, and are sometimes observed to coexist with ELMs and with the EDA H-mode's QC-mode.

3.2.2 Global Characteristics of the I-Mode

A typical discharge with L-mode to I-mode and I-mode to H-mode transitions is plotted in Figure 3-4. In this example, the I-mode is accessed in the normal field, USN configuration (Figure 3-3(a)). As the P_{ICRF} is slowly increased in steps, the plasma transitions from L-Mode to I-mode at $t \approx 1s$, as can be observed by the increases in edge and core electron temperatures. There is, nonetheless, no visible change in the line averaged density, indicating an L-mode like particle confinement during this period. At $t \approx 1.45s$, there is a transition from the I-mode to an ELM-free H-mode, which transiently raises the line averaged density. As was mentioned in Section A.3.1, the ELM-free H-mode is inherently transient and, as the impurities accumulate, the edge and core temperatures start to collapse and the plasma transitions back to L-mode after the ICRF is turned off. The τ_E is about 30ms in this shot, so the I-mode is sustained for approximately 15 energy confinement times. Also, the confinement factor for this example, $H_{98} \equiv \tau_E/\tau_{98}$, reaches 1 during the I-mode phase, indicating H-mode equivalent energy confinement.

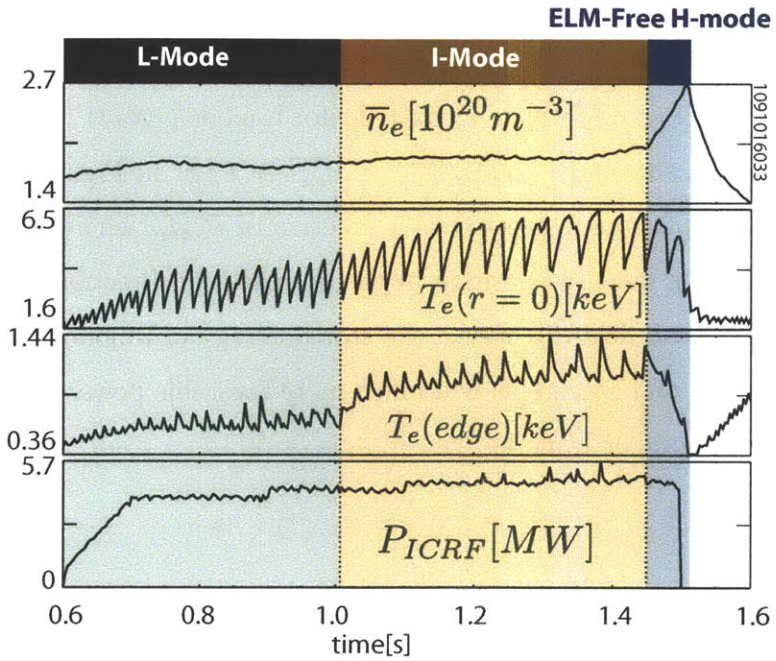

Figure 3-4: The time traces for a typical discharge with L-mode to I-mode and I-mode to H-mode transitions show the global characteristics of the I-mode regime. During the I-mode period, the edge and core temperatures rise while the density stays at the L-mode level. After the I- to H-mode transition, the density rises rapidly, leading to the typical H-mode regime. $I_p = 1.2MA$ during this discharge.

Improvement in power degradation

As discussed previously, the scaling laws for the energy confinement time of L-mode and ELMy H-mode plasmas in tokamaks have been determined by using data bases from many tokamaks from around the world. They have been presented in Section A as τ_{ITER89} for L-mode and as τ_{ITER98} for H-mode in Equations A.2 and A.7 respectively. The degradation of τ_E with increasing P_{tot} changes from $\tau_E \propto P_{tot}^{-0.5}$ in L-mode to $\tau_E \propto P_{tot}^{-0.69}$ in H-mode, while they both have approximately linear dependences on I_p. From these scalings, we can derive expectations for the stored energy, $W = \tau_E \times P_{tot}$ and $P_{tot} \times I_p$ which, at fixed I_p, for L-mode gives $W \propto P_{tot}^{-0.5+1} = P_{tot}^{0.5}$, while for H-modes, we get $W \propto P_{tot}^{-0.69+1} = P_{tot}^{0.31} \approx P_{tot}^{0.3}$. In Figure 3-5, the stored energy for I-mode plasmas is plotted as a function of $P_{tot}I_p$, where, for display purposes, the current is taken as positive in the normal field direction and negative in reverse field. For both field directions, the stored energy in I-mode is approximately linear with both I_p and P_{tot}. This is a much more favorable power dependence than that for either H-mode or L-mode.

I-mode impurity confinement

The impurity confinement time, τ_I, of the I-mode regime has been measured using a CaF_2 impurity laser blow off system[3][85]. Shown in Figure 3-6, the I-mode τ_I is similar to that of the L-mode while sustaining a much higher energy confinement factor, H_{98}. Compared with the EDA H-mode, the I-mode τ_I is, less than half as large, which is not surprising based on the L-mode like particle confinement. Beyond the range of the plot, the impurity confinement time of the transient ELM-free H-mode is too large to measure with the blow off system. This is consistent with the steady state nature of the I-mode and the EDA H-mode as compared to the ELM-free H-mode, and underlines the importance of impurity ejection for the sustainment of the high energy confinement regime.

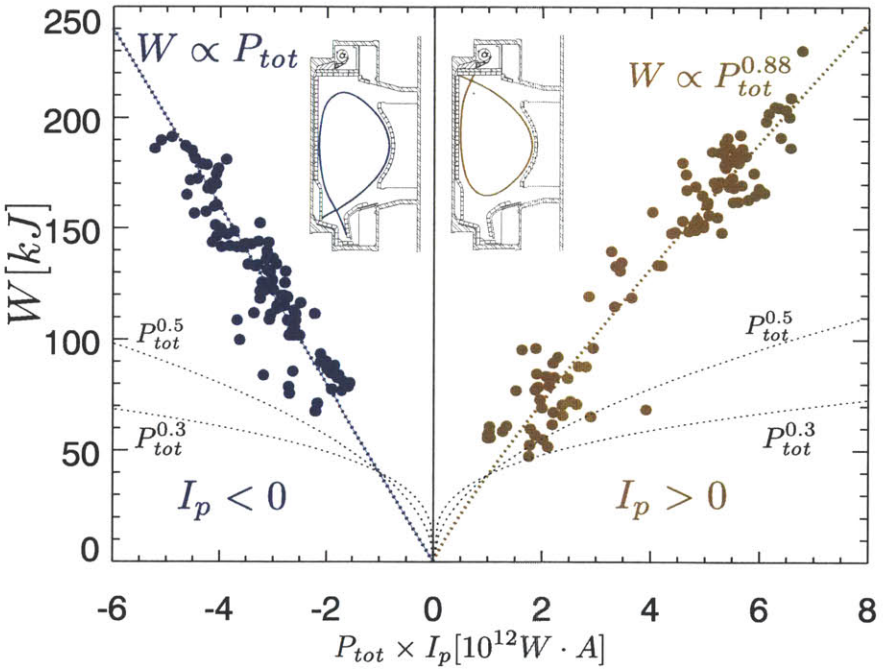

Figure 3-5: I-modes suffer less power degradation than L-modes and H-modes. Normalizing with I_p, the plasma stored energy, W, is almost linear in the unfavorable drift direction for both normal and reversed field configurations.

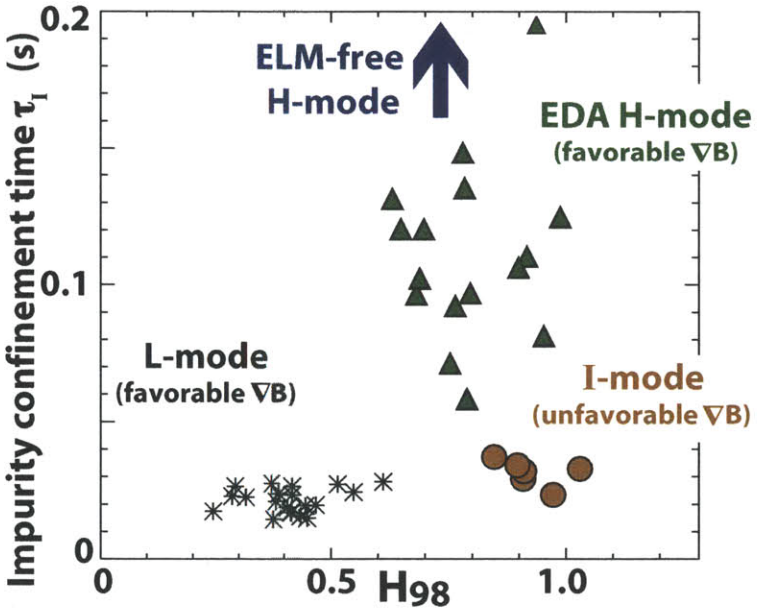

Figure 3-6: Impurity confinement times, τ_I, in I-mode are comparable to those of L-mode, lower than EDA H-mode and much lower than ELM-free H-mode. The high H_{98}, low τ_I characteristics of the I-mode are desirable for reactor type plasmas. Figure adapted from [3].

Confinement factor, q_{95} and pedestal collisionality of the I-mode

In Figure 3-7(a), the confinement coefficient, H_{98}, is plotted against the safety factor at the edge, q_{95}, for 215 time slices in the unfavorable drift direction I-modes, both in normal field (red) and in reverse field (blue), as well as 23 slices in the EDA H-mode (green triangles). As has been stated previously, in I-mode, the energy confinement coefficient, H_{98}, can surpass 1. Also observed in this plot, the I-mode can reach very low values of q_{95} (below 3) due to the high I_p (of up to 1.4MA), although with reduced confinement. Note that typically EDA H-modes can only be accessed at higher q_{95}, typically above 3.7, although at low I_p operation lower q_{95} values may be reached. In Figure 3-7(b), the edge temperature at the pedestal of the plasma in H-mode is plotted as a function of the normalized collisionality, ν^*, which is the electron collision frequency normalized by the banana orbit bounce frequency, $\nu^* \equiv \nu_{ee}/\nu_b$, where $\nu_b = \sqrt{\epsilon} v_{th,e}/(Rq_{95})$. The pedestal temperatures can reach 1keV, which are typically accessed only in ELMy H-modes on C-Mod. As a comparison, the EDA H-modes have a factor of two lower pedestal temperatures, typically 500eV or less. Consequently, the edge collisionality of the I-mode is much lower (by an order of magnitude) than that of the EDA H-mode.

Due to the high temperatures reached at the pedestal and to the temperature profile stiffness observed on C-Mod[25], the I-modes reach very high core electron temperatures (up to 9keV). Due to their high temperatures, the pressure profiles in I-mode can be comparable to those of typical EDA H-modes, as can be observed in Figure 3-8. The ion temperature is typically not as high as the electron temperature due to the lower collisionality at the core, nonetheless, the ion temperature at the core of $T_e(core) = 9keV$ plasmas is estimated to be in the order of $T_i(core) = 6keV$. This is very favorable for the prospect of using I-modes in reactors because of the neutron rate proportionality to p_i^2, as discussed in Section 1.1.1.

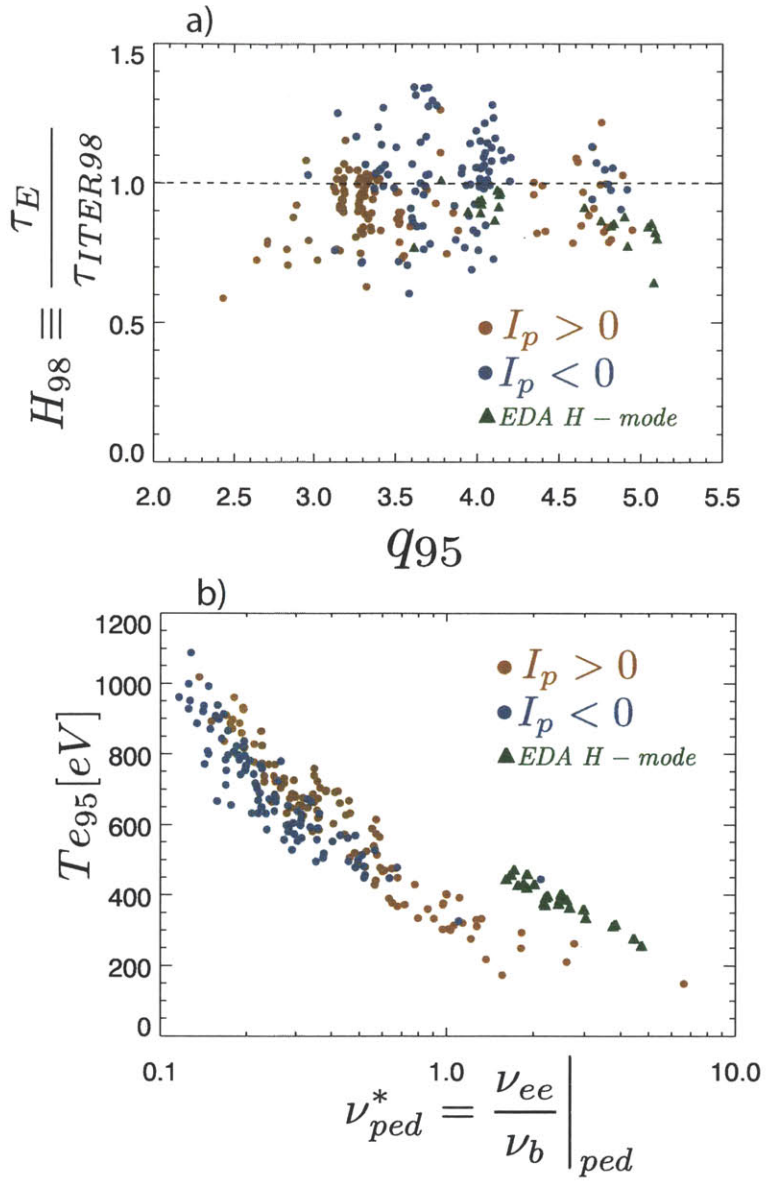

Figure 3-7: a)The confinement coefficient, H_{98}, for I-modes in unfavorable drift direction in both normal and reverse field is similar to, or higher than, that of the H-modes. The I-modes can be accessed at high I_p, with q_{95} reaching below 3. b)The I-modes are typically restricted to very low collisionality due to the very high T_e and low n_e at the edge. Due to the very high temperatures at the edge of the plasma, the expected pedestal collisionalities for ITER are $\nu^*_{ped} \leq 0.1$[17][18]

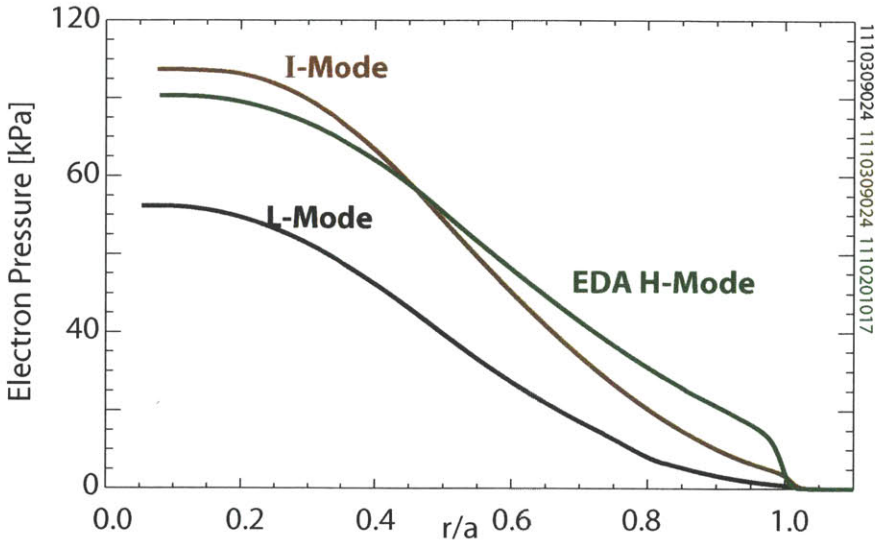

Figure 3-8: Typical L-mode, I-mode and EDA H-mode pressure profiles versus normalized minor radius. Due to the high core temperatures, I-modes reach high pressures at the core of the plasma, similar to, and even surpassing, H-mode pressures. The pressure is derived from Thomson scattering n_e and T_e measurements.

E_r wells at the edge of the plasma

As discussed in Section A.3, one of the main theories behind the formation of the H-mode transport barrier is the presence of a radial electric field well at the edge of the plasma which causes $v_{E\times B}$ shearing of turbulent eddies and reduces transport.

The E_r well has been measured on Alcator C-Mod using a high resolution charge exchange recombination spectrometer[2] for various regimes. The E_r radial profiles at the edge are plotted in Figure 3-9. As expected, the L-mode E_r profile shows no sign of a well close to the LCFS of the plasma. The EDA H-mode, on the other hand, displays a clear dip in the value of E_r, changing sign from radially outward to radially inward and back, within 1cm. This is also consistent with the global confinement enhancement of the EDA H-mode, because of the strong shear in $v_{E\times B}$.

The I-mode also displays the presence of an E_r well, albeit not as exaggerated as that of the EDA H-Mode. This measurement clearly separates the I-mode as an independent regime and suggests a physical mechanism for the enhanced energy confinement characteristic of the mode. Nonetheless, there remains the question of the particle

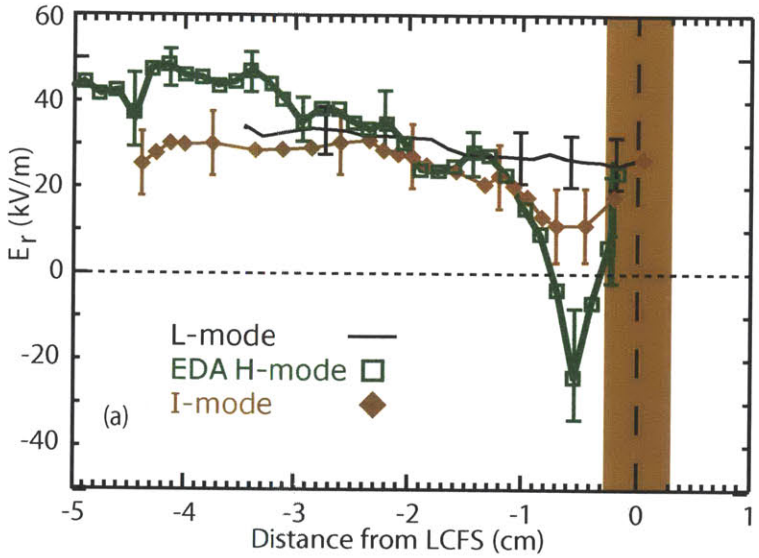

Figure 3-9: Using charge exchange recombination spectroscopy, the E_r radial profiles have been measured for L-mode, I-mode and EDA H-mode plasmas on Alcator C-Mod[2]. The presence of an intermediate E_r well for the I-mode suggests a mechanism for the enhanced energy confinement in this regime. This finding leaves the mechanism behind particle and impurity L-mode-like transport unresolved. The figure used is from [2].

and energy channel separation. In other words: If the presence of an E_r well is responsible for the enhanced energy confinement, how does the particle and impurity transport remain at L-mode levels?

Toroidal rotation in the I-mode

Finally, one interesting physical insight that has been gained by the particle and energy transport channel separation obtained in the I-mode, has to do with the intrinsic toroidal rotation in this confinement regime. As discussed in Section A.3, velocity shear can lead to improved confinement due to the breaking of turbulent eddies. Neutral beam injection is a natural source of toroidal torque in large tokamaks today, leading to sheared rotation in the plasma, yet this method will be very difficult to implement in energy producing-type tokamaks due to limitations on beam penetration[86]. Intrinsic rotation has been extensively studied on Alcator C-Mod, where, due to the fact that it does not use NBI, there is no source of external torque on the plasma during auxiliary heating. It was found that when the stored energy is increased in the L-H transition, a change in core toroidal rotation towards the co-current direction is observed, which is proportional to the change in stored energy normalized by the plasma current: $\Delta V_{tor} \propto \Delta W/I_p$[87]. This dependence can be traced back to the edge of the plasma with $\Delta V_{tor} \propto \nabla p_{edge}$. Nonetheless, in [19], it was shown that the fit is improved when comparing the change in rotation to the edge temperature gradient as opposed to the edge pressure gradient, as shown in Figure 3-10.

3.3 Changes in edge fluctuations

Early in the exploration of I-modes on C-Mod, it was observed that the global changes associated with this regime were accompanied by changes in the fluctuations measured at the edge (first observed on the fast magnetic coils described in Section 2.3.4)[1]. As shown in Figure 3-11, the two main fluctuation features of the I-mode are:

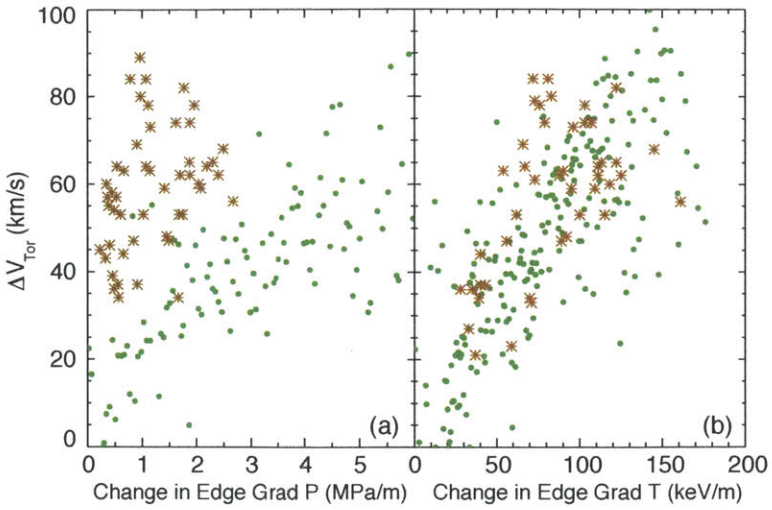

Figure 3-10: The change in toroidal rotation in H-mode (green) scales well with both ∇T and ∇p at the edge on Alcator C-Mod. Since I-modes can have strong ∇T while having small ∇n it can be distinguished that the changes in toroidal velocity are more correlated with edge temperature gradients than with edge pressure gradients. Figure from [19].

- Reduction of broadband fluctuations at intermediate frequencies ranges, $50kHz < f < 150kHz$.
- Enhanced fluctuation levels spectrally centered at around $150kHz < f < 300kHz$.

These two phenomena will be discussed in depth in the next two sections.

3.3.1 Broadband fluctuation reduction and energy confinement

During the L-mode phase, the edge fluctuations are dominated by broadband turbulence, as observed before t=1.14s in Figure 3-11. As the plasma transitions to the I-mode, one of the principal changes in fluctuation characteristics is a decrease in this broadband fluctuation level in the mid frequency range: approximately $50kHz - 150kHz$[1][3][4]. This range can vary, for example, in Figure 3-11 the broadband reduction occurs for $f \approx 40kHz - 200kHz$.

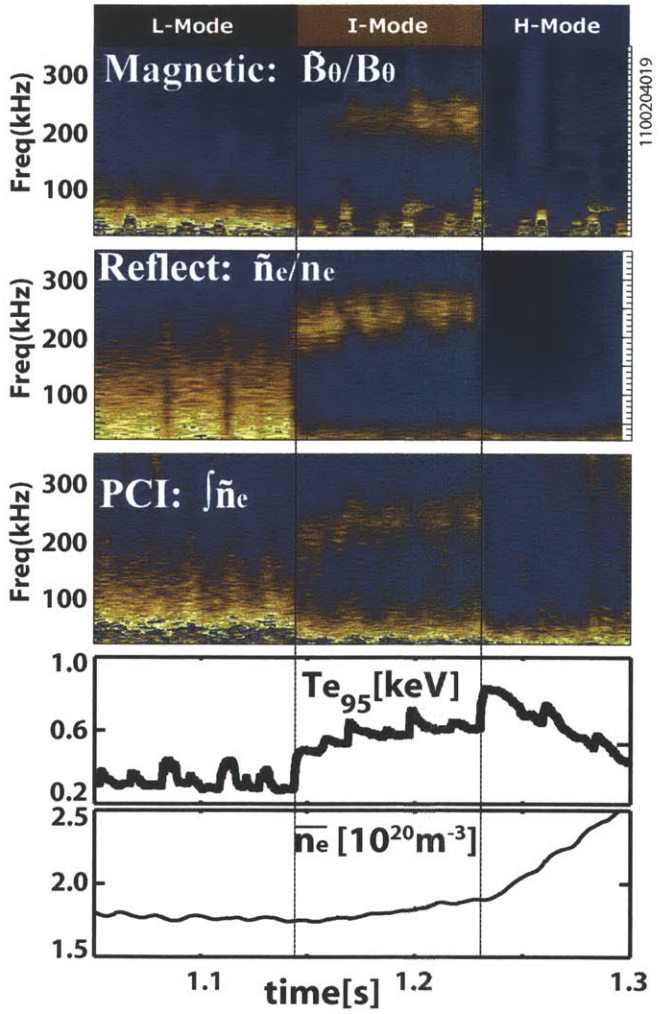

Figure 3-11: The I-mode is accompanied by changes in the edge fluctuations, mainly an enhancement at high frequencies ($200kHz - 300kHz$ in this example), and a reduction of broadband fluctuations at lower frequencies ($50kHz - 200kHz$ in this example). Shown, are the fluctuation spectra for magnetic coils, reflectometry and PCI, but these phenomena have also been observed on GPI and ECE (all described in Chapter 2). The bottom 2 traces show time histories of T_e at the 95% flux surface (near the top of the pedestal), and the line averaged density, $\overline{n}_e$. $I_p = 1.3MA$ for this discharge.

The frequency range of the broadband reduction is typically proportional to I_p, or inversely proportional to q_{95}, that is, the clearest examples of the reduction occur for high plasma current cases such as the one shown in Figure 3-11 ($I_p = 1.3MA$).

It is observed that the broadband reduction correlates well with a decrease in the measured effective thermal conductivity, χ_{eff}, of the plasma at the steep temperature pedestal region, where $\chi_{eff} \equiv -P_{net}/(2n_e\nabla T_e)$, $P_{net} = P_{tot} - dW/dt - P_{rad}$, P_{tot} is the input power associated with the ohmic and auxiliary RF sources, dW/dt is the power going to increase the stored energy of the plasma and P_{rad} is the radiated power from the confined plasma. P_{net} is, therefore, the power that is conducted across the LCFS of the plasma.

In the example shown in Figure 3-12, the power balance code TRANSP has been used to estimate the value of χ_{eff} at $r/a \approx 0.98$ for an I-mode shot. The integrated fluctuation level in the 50kHz to 150kHz range from a reflectometry channel reflecting at approximately the same radial location, has been overplotted on the χ_{eff} trace. As the fluctuation level in the mid-frequency range drops through the L-I transition and then, later, through the I-H transition, the thermal conductivity follows the same exact trends.

This correlation is strong evidence of the causal connection between the decrease of mid-frequency range fluctuations and the suppression of energy transport across the LCFS. As is discussed in Section 3.2.2, the presence of an E_r well, measured using charge exchange recombination spectroscopy[2], during the formation of the I-mode could explain the physical mechanism of the formation of the T_e barrier through $\vec{v}_{E\times B}$ shear suppression. The particle transport is, nonetheless, much higher than in an H-mode, so there must exist a mechanism that leads to the increased particle transport. One such mechanism proposed is the WCM.

3.3.2 The Weakly Coherent Mode

The high frequency feature observed during the I-mode is typically centered at around $150kHz - 300kHz$ and has a spectral width of $\Delta f/f_{peak} \approx 0.5$, but it can vary

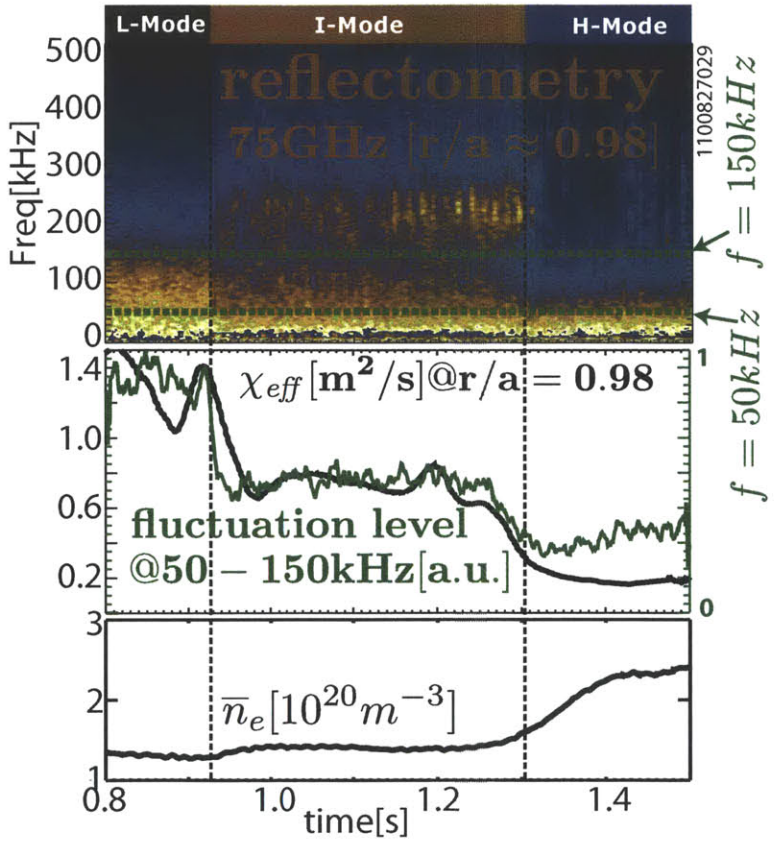

Figure 3-12: The broadband reduction during the I-mode correlates well with the changes in χ_{eff} at the edge of the plasma. In this example, the power balance code, TRANSP, has been used to estimate χ_{eff} at the top of the pedestal, and the fluctuation changes are observed in the reflectometry signal at the same edge region.

from $0.2 < \Delta f/f_{peak} < 1$, hence the *weakly coherent mode* description, or WCM. In Figure 3-11, the spectra from fast magnetic field coils, reflectometer and PCI during a discharge with L-mode to I-mode and I-mode to H-mode transitions are shown, featuring the presence of the WCM at f_{peak}~$250kHz$ with $\Delta f \approx 50kHz$. In addition to the traces shown, the GPI system and the ECE diagnostic also observe the presence of the WCM, and thus, the mode has density, temperature and magnetic field fluctuating components. The wide range of diagnostics sensitive to the WCM have helped to characterize the mode.

WCM radial localization

The radial position of the WCM has been localized by the use of the O-Mode reflectometry system. As discussed in Section 2.2, the radial position of the reflection layer of each channel in O-mode reflectometry is determined by the local electron density as: $n_{e(cutoff)} = (f(GHz)/89.8)^2$, where n_e is in units of $10^{20}m^{-3}$, $f(GHz)$ is the channel frequency in GHz, and interpolated Thomson scattering data are used to determine the electron density radial profiles of the plasma, and thus, the positions of the cutoffs.

In the example shown in Figure 3-13(a), the autopower spectra of three independent reflectometry channels at 60GHz, 75GHz and 88.5GHz are plotted during an I-mode phase. The radial location of each cutoff layer, determined from the TS density profiles, are plotted as a function of time. The lowest frequency channel, which reflects outside the LCFS during the duration of the I-mode, does not observe the WCM throughout. The 75GHz channel, which reflects within the first 1 to 2 cm inside the LCFS, observes the WCM during the entire I-mode period. As observed by the density time trace, the electron density rises at the end of this time. As the density rises, the cutoff position of the 88.5GHz channel moves from the core to the edge, and, while its spectra do not show the presence of the WCM during the lower density segment of the I-mode, as the density rises and the cutoff layer approaches the LCFS, the spectra begin to show the enhanced fluctuations at ~$300kHz$.

A density profile is plotted for t=1.35s, approximately when the 88.5GHz begins to

detect the WCM. The shadowed radial region in both the density profile plot, as well as the channel cutoff location plot, is the region where, in this example, the WCM is observed, corresponding to approximately the first 2cm inside the LCFS or $0.9 < r/a < 1$.

Another diagnostic technique routinely used to determine the position of the WCM is gas puff imaging (GPI). As shown in Figure 3-13(b), by using the 2D diode array (described in Section 2.3.1), the radial position has also been estimated to within the first 1-2cm inside the LCFS. Typically, the largest distance inside the LCFS that the array can detect during I-mode discharges, is $\sim 1.5cm$, and in many cases, the *rollover* of the detected WCM signal is not observed, suggesting a peak further inside the plasma. Nonetheless, by repeated observation of I-mode discharges using reflectometry, GPI and ECE (which will be discussed later), the radial location of the mode has been well determined to be within the outer 10% in flux of the confined plasma, with little or no contribution outside the LCFS.

WCM poloidal localization

While the GPI system and the reflectometry system are best suited for radial localization of the mode, their poloidal extent is limited to a region of about 10cm at the outboard midplane of the plasma.

Magnetic coils, on the other hand, have a large poloidal extent which has been used to detect poloidal variations of the WCM strength (see Section 2.3.4). While the poloidal localization studies are still preliminary, the amplitude of the magnetic fluctuating component of the WCM is observed to vary poloidally at the outboard side of the plasma as observed in Figure 3-14a[88].

The PCI system (see Section 2.3.2), which observes vertical line integrated density fluctuations through the core of the plasma, has measured a peak of the WCM within its radial viewing range, hence, away from the outboard midplane. An example of this can be seen in Figure 3-14b.

This asymmetry has been observed in all I-mode configurations shown in Figure 3-3,

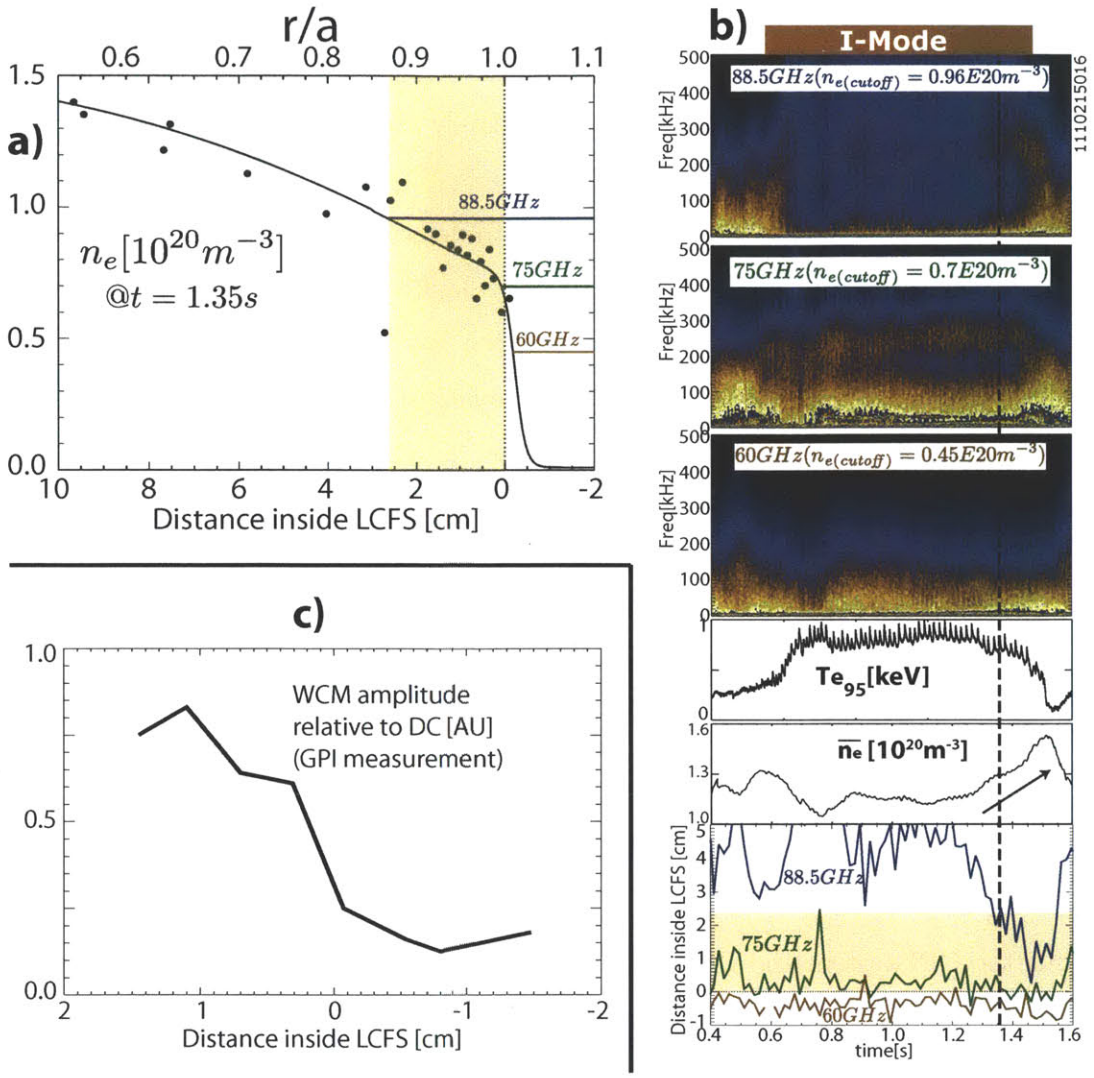

Figure 3-13: a)Using the n_e profiles, the radial positions of the cutoff layers for the reflectometry system can be determined. If a given channel observes the WCM, the mode's radial position can, then, be deduced. b) The evolving location of the WCM throughout an I-mode period can be estimated by observing the presence of the mode in the autospectra. In this example, the mode is seen in the 75GHz channel throughout the whole I-mode, whereas it can only be seen by the 88.5GHz channel at the end of the I-mode period, when the density increases, moving the cutoff layer from the core to the edge. In this case, the WCM is observed at approximately 2cm inside the LCFS, that is at $r/a \sim 0.9$. c) The GPI system has also been used to radially localize the WCM to within the outer 1 to 2 cm of the confined plasma. The *rollover* position, determining the peak of the mode, is not always observed within the first $\sim 1.5\ cm$ inside the LCFS (the radial range of the system), yet, in the example shown, the signal is observed to peak at $\sim 1\ cm$ inside the plasma.

and in each case, the WCM is observed to be strongest in the electron diamagnetic drift direction, that is, in the $-(\vec{B} \times \nabla B)$ direction.

In contrast, in the Quasi-coherent mode (QCM), the signature of the EDA H-mode, a poloidal asymmetry is not seen. In fact, the magnetic field coil and PCI measurements for the QCM are vertically symmetric around the outboard side midplane. This suggests a qualitative difference between the QCM and the WCM, a topic which will be expanded on in Section 3.4.

Spectral characteristics of the WCM

Utilizing the 2D measurement capability of the GPI system, a spatial Fourier transform of the measured signals at the midplane in the vertical direction has been used to measure the lab frame poloidal wavenumber, k_θ, of the WCM, as described in Section 2.3.1. Shown in Figure 3-15a, the f *vs* k_θ plot is shown for a typical unfavorable drift direction I-mode. In the figure, the WCM can be observed in the 200kHz-270kHz frequency range with a k_θ range of $1.5 - 2.5\ cm^{-1}$ in the EDD direction[1], which has been seen as the typical wavenumber and lab frame direction of propagation of the WCM for all I-modes analyzed[3][4][22].

PCI measurements have confirmed the $k_\theta \approx 2cm^{-1}$ from GPI by using the k_θ projections from k_R at the position of the vertical chords' intersections with the edge of the plasma.

A range for the poloidal phase velocity of the mode in the lab frame can then be calculated by taking into account the frequency and wavenumber range of the WCM:

$$v_{ph,\theta,lab} = \frac{2\pi}{100}\frac{f[kHz]}{k_\theta[cm^{-1}]}[km/s] = \frac{2\pi}{100}\frac{(150-300)}{(1.5-2.5)}[km/s] \approx (4-12)\,[km/s]. \quad (3.1)$$

The plasma frame velocity of the mode can be estimated by measuring the $v_{E\times B}$ at the edge and doing a newtonian lab frame transformation. The results of this analysis are in Section 3.4, where comparisons with the EDA H-mode QCM are highlighted.

Toroidally separated magnetic field coil measurements show that the WCM propa-

[1]The *ion diamagnetic drift* direction, or IDD, is the same as the *grad B drift* direction or $\vec{B}\times\nabla B$. The *electron diamagnetic drift* direction, or EDD, is, therefore, the $-\vec{B} \times \nabla B$ direction.

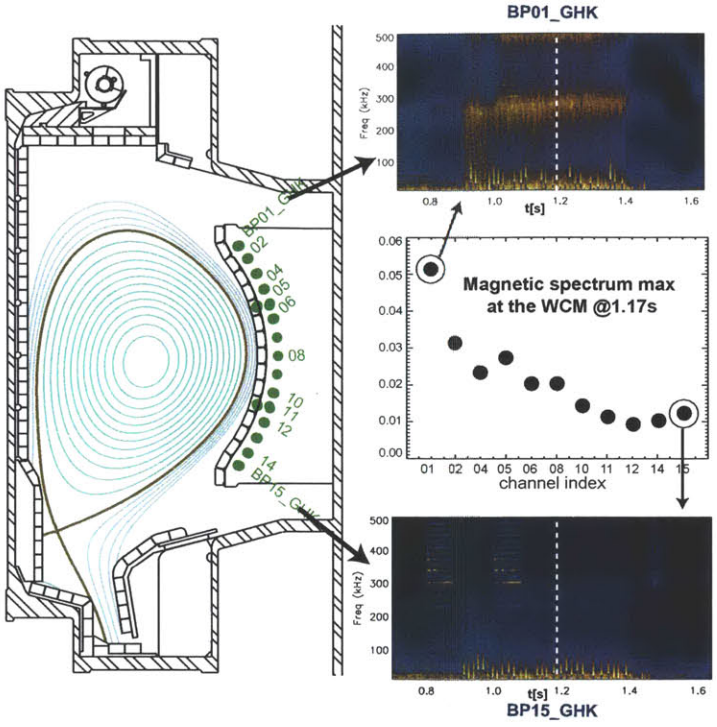

(a)

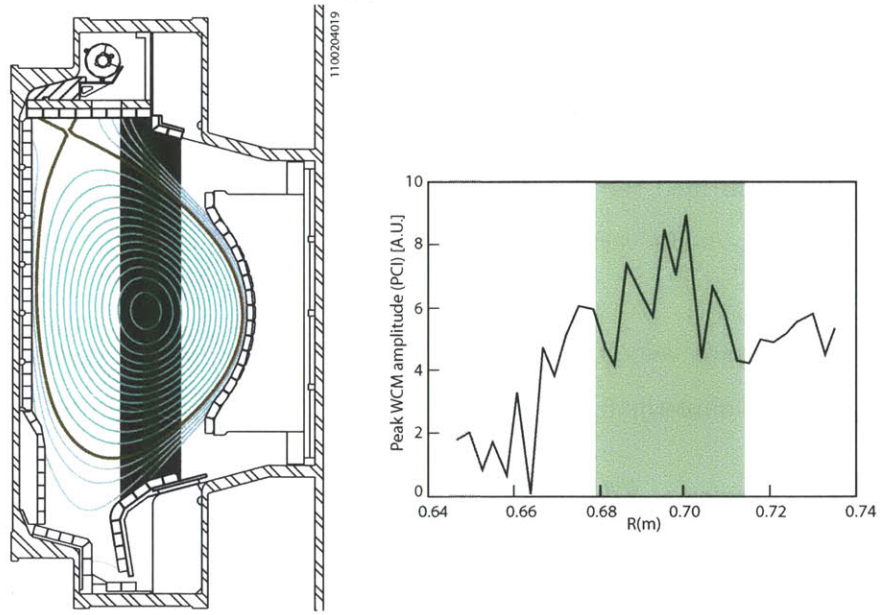

(b)

Figure 3-14: a)The fast magnetic field coils are poloidally separated and have observed a poloidal variation of the amplitude of the WCM. In this case, the I-mode is in favorable drift direction. b)The PCI signal observes line integrated density fluctuations and has shown a peak of the WCM away from the outboard midplane. In this case, the I-mode is in the unfavorable drift direction and the green shading indicates the region of the WCM amplitude peak in this example. Figure is adapted from [20]

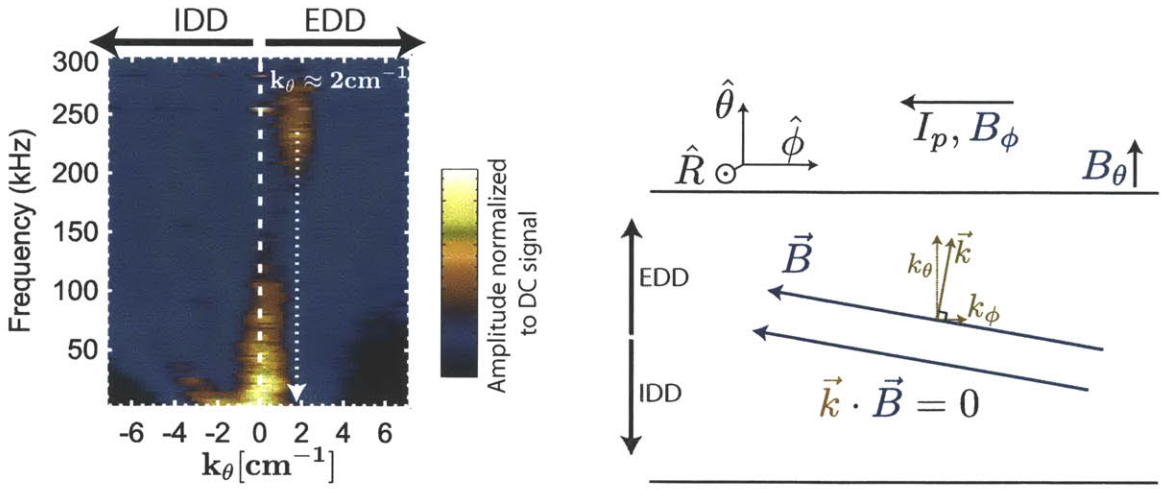

(a) (b)

Figure 3-15: a) By using GPI and PCI, the k_θ of the WCM has been estimated to be approximately $2cm^{-1}$ in the EDD. b) Magnetic field coil measurements show a k_ϕ in the countercurrent direction. This is consistent with the WCM being a field aligned mode ($\vec{k} \cdot \vec{B} = 0$). The schematic shows a midplane view of the plasma from the outboard midplane.

gates in the countercurrent direction, hence k_ϕ is countercurrent and, since the direction of poloidal propagation is the EDD, the WCM appears to satisfy the $\vec{k} \cdot \vec{B} = 0$, field-aligned mode condition. A schematic of this is shown in Figure 3-15b.

By using both poloidally and toroidally separated magnetic field coils, the m/n ratio has been estimated. Since $k_\theta \approx 2cm^{-1}$ independently of q_{95},which, as shown in Figure 3-7, has a range of approximately 2.5-5, the m/n ratio varies from $m/n \approx 6$ for high q_{95} and $m/n \approx 3$ for low q_{95}[3].

Density and temperature fluctuation components of the WCM

As mentioned previously, the GPI, PCI and reflectometer are sensitive to the density fluctuating component of the WCM.

The amplitude of the WCM has been estimated from the 2D GPI array measurements by comparing GPI normalized brightness profiles between the EDA QC-Mode and the WCM. As will be discussed in Section 3.4, the mode amplitude of the QCM has been measured directly, $\tilde{n}_e/n_e \approx 35\%$, and the QCM amplitude has been measured to be

approximately 3 times bigger than the WCM. The current estimated range for the density fluctuation amplitude is: $\tilde{n}_e/n_e \approx 6\% - 16\%$[21][22].

The T_e fluctuation amplitude of the WCM has been studied using the high resolution ECE radiometer (see Section 2.3.3)[21]. As seen in Figure 3-16a, the WCM was observed in the autospectrum at $r/a \approx 0.95$ (within 1cm of the LCFS), with an amplitude equivalent to $\tilde{T}_e/T_e \approx 1.6\%$, assuming large optical depth.

One of the complications of this measurement is that the ECE radiometer is not only sensitive to T_e fluctuations, but it can also acquire contributions from fluctuations in optical depth, τ, which depends on the local density and temperature. $\tilde{n}_e/n_e$ contributions to the signal depend on the value of τ. In Figure 3-16a the thermal contribution to the signal is plotted as a function of τ for different levels of $\tilde{n}_e/n_e$ at the measured location. While there is a level of uncertainty of the value of τ, at the 1cm location where the WCM is measured, $\tau \geq 4$, which is highlighted in Figure 3-16b. Since the density fluctuation amplitude of the WCM is estimated to be $6\% < \tilde{n}_e/n_e < 16\%$, the temperature fluctuation component of the WCM is, from the data in Figure 3-16b, in the range: $1\% < \tilde{T}_e/T_e < 2\%$[21]. The temperature fluctuation component of the WCM is, therefore, one order of magnitude smaller than the density fluctuation.

3.4 The WCM and the QCM: A comparison

As discussed in Section A.3.2, the EDA H-Mode is accompanied by enhanced density, temperature and magnetic fluctuations in the $50-150kHz$ range, the Quasi-Coherent Mode, or QCM.

The general characteristics of the QCM are, in many ways, similar to those of the WCM. In fact, the name *Weakly Coherent Mode* is derived from that of the QCM, but highlighting the wider spectral width of the WCM compared to the QCM.

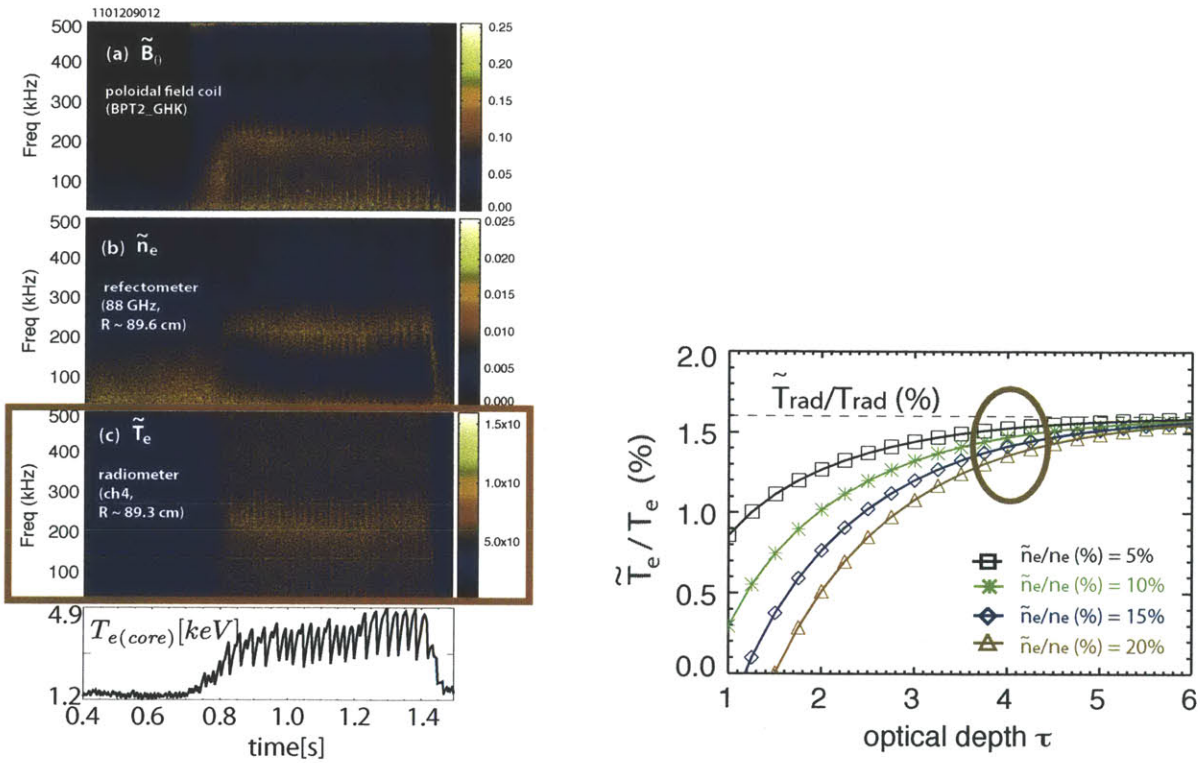

(a) (b)

Figure 3-16: a)In addition to being detected by magnetic pick up coils at the wall and by the O-mode reflectometer, the WCM is observed using the fast ECE radiometer. In this example, the detected signal is within 1cm of the LCFS, at $r/a \sim 0.95$. b) While the ECE signal is sensitive to $\tilde{T}_e/T_e$, it also responds to $\tilde{n}_e/n_e$, if the plasma is optically thin. Here it is shown that the optical thickness of the plasma is high enough ($\tau \geq 4$) at the edge of the plasma that the main contribution of the ECE signal is from thermal fluctuations. Both figures are adapted from [21].

3.4.1 Spatial location

The radial location of the QCM is, similar to the WCM, close to the steep temperature gradient region at the edge of the plasma. As shown in Figure 3-9, the edge regions of both EDA H-mode and I-mode feature the presence of an E_r well which is believed to be connected to the enhanced energy confinement (relative to L-mode) of both regimes (and in the case of the EDA H-mode, the enhanced particle confinement, as well). The steep gradients in this radial region can account for the free energy necessary to excite both modes.

In Section 3.3.2, the poloidal location of the WCM was shown to be poloidally shifted toward the electron diamagnetic direction (EDD). Similar analysis[20] of the QCM shows that, unlike the WCM, there is no evidence of a poloidal shift in the location of the QCM.

3.4.2 Amplitude of $\tilde{n}_e/n_e$ component

The amplitude of the $\tilde{n}_e/n_e$ component of the QCM has been measured directly through a variety of diagnostics. Initial measurements were performed using a scanning probe which gave direct density fluctuation amplitude measurements at the QCM location of $\tilde{n}_e/n_e = 30\%$[89]. By using the GPI diagnostic, comparisons of the locations and the magnitudes of the WCM and the QCM have been made. In the example shown in Figure 3-17a, both modes are seen localized close to the top of the temperature pedestals slightly inside the steep gradient region (from Figure 3-17b). For both the WCM and the QCM, the radial location has also been observed to extend further towards the LCFS (see Figure 3-13 for the WCM and [90] and [91] for the QCM) and sometimes surpassing it. In the example shown in Figure 3-17a, the density fluctuation component of the QCM agrees with the probe measurements of $\approx 30\%$, while the WCM is about 1/3 that size, at $\tilde{n}_e/n_e \approx 10\%$[22].

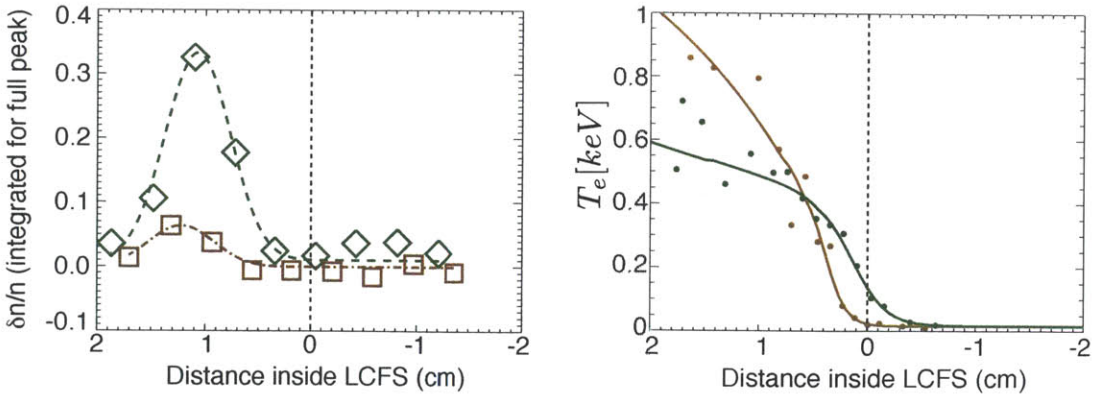

(a) (b)

Figure 3-17: a)GPI measurements show the QCM (green) and the WCM (red) localized close to the top of the temperature pedestals, right inside the steep gradient regions (shown in (b)). Note that, for other examples, the radial positions of both modes have also been measured closer the the LCFS. The value of $\tilde{n}_e/n_e$ is measured by integrating the WCM contribution to the $f-k$ spectra at a given radial position (e.g. Figure 3-18). The $\tilde{n}_e/n_e$ of the QCM is confirmed to be approximately 30%, whereas the density fluctuation component of the WCM is measured to be approximately 10%. Figure (a) is from [22].

3.4.3 Spectral comparison of WCM and QCM

Since both modes are localized close to the LCFS, the GPI system (see Section 2.3.1) can be used to compare the poloidal wavenumbers of the two modes. In Figure 3-18, the $k-f$ plots for an I-mode and an EDA H-Mode are compared, with the WCM and QCM highlighted. As seen, while the frequencies of the two modes are substantially different, the k_θ values of both modes are similar, approximately 2cm^{-1}. There is also the similarity that the direction of k_θ for both modes is consistently in the EDD, as shown in the figure.

As mentioned above, the frequency of the two modes, measured in the lab frame, is typically very different, as well as the frequency width of the modes. The peak frequency of the QCM is usually restricted to $f_{QCM} = 50 - 100kHz$, whereas that of the WCM is typically about three times that, $f_{WCM} = 150 - 300kHz$. Seen in Figure 3-19 are time traces of the stored energy during an EDA H-mode (a) and an I-Mode (b) . For the I-mode, the autospectrum from the 88.5GHz reflectometer channel

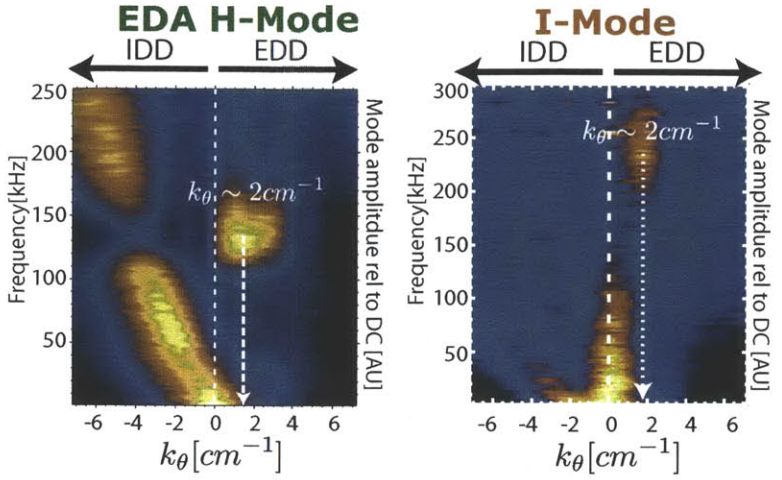

Figure 3-18: The $k - f$ plots at the edge of the plasma for an EDA H-mode and an I-Mode show the presence of the QCM and the WCM respectively. While the frequency of the WCM is considerably higher (centered at $\sim 250KHz$) than that of the QCM (centered at $\sim 70kHz$), the k_θ values of both are relatively similar, at approximately 2cm^{-1}. Figures adapted from [23].

($n_{e(cutoff)} = 0.97 \times 10^{20} m^{-3}$) is shown, where the WCM is prominent. For the EDA H-Mode, an autospectrum of a PCI channel is shown, where the QCM appears during the H-mode phases. As stated, the frequency of the QCM is consistently lower than that of the WCM. Moreover, the evolution of the two modes is substantially different. As the stored energy increases during the I-mode, the WCM appears from the broadband fluctuations and grows in frequency concomitantly. For the EDA H-Mode, there is a delay approximately 15ms after the transition to the H-mode (characterized by the decrease in broadband fluctuations as well as global changes, not shown), before the onset of the QCM. During the subsequent evolution, the QCM frequency decreases as stored energy increases, and then increases again as stored energy falls.

3.4.4 Lab frame vs. plasma frame velocity

As discussed, both the WCM as well as the QCM are radially localized in the region of steep gradients, which is also where the E_r wells are located. In addition to playing a central role in the changes in confinement, the $v_{E\times B}$ from the E_r also doppler

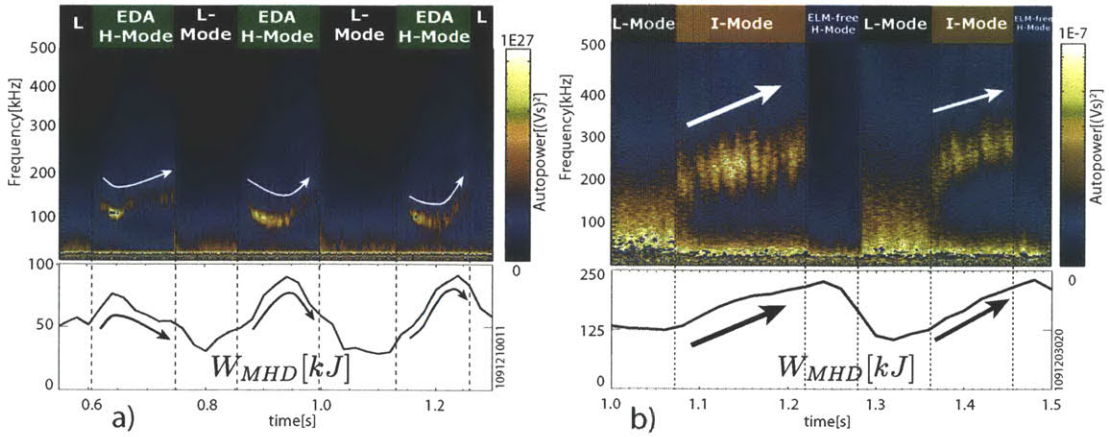

Figure 3-19: One of the most clear differences between the QCM and the WCM is the mode dependencies on the stored energy. For the QCM, the changes in center frequency of the mode are inversely proportional to changes in the stored energy of the EDA H-mode. In contrast, the center frequency of the WCM varies proportional to the stored energy.

shifts the frequency of the modes from the *plasma frame*, to the *lab frame* where the measurements are taken. Since $\vec{B}$ is primarily in the $\hat{\phi}$ direction, $v_{E\times B}$ can be assumed to be mainly in the $\hat{\theta}$ direction. Therefore, Newtonian frame transformations can be imposed on the phase velocities of the mode,

$$\vec{v}_{ph,\theta,lab} = \vec{v}_{ph,\theta,plasma} + \vec{v}_{E\times B} \tag{3.2}$$

$\vec{v}_{ph,\theta,lab}$ for both modes is in the EDD (as seen in Figure 3-18) with speeds of about $8km/s$ for the WCM and $3km/s$ for the QCM. The measured E_r at the well, where the modes reside, is in the $-\hat{r}$ for the EDA H-modes and in the $+\hat{r}$ direction in the I-modes. In the example shown in Figure 3-9, the radial electric fields at the well for the EDA H-mode and the I-mode are approximately -25kV/m and +10keV respectively. This results in a strong $\vec{v}_{E\times B}$ pointing in the EDD for the EDA H-mode and a weak $\vec{v}_{E\times B}$ in the IDD for the I-mode. An initial study of this was conducted[92], using the E_r measurements from [2], shown in Figure 3-9, but fluctuation data from different I-mode and EDA H-mode discharges. The plasma frame phase velocities were found to be:

- $\vec{v}_{ph,\theta,plasma} \approx 10km/s$ in the EDD for the WCM
- $\vec{v}_{ph,\theta,plasma} \approx 2km/s$ in the IDD for the QCM when using the E_r value at the bottom of the well.

More recent experiments have measured E_r and fluctuation data for the same discharges[22] and yield similar results:

- $4.5km/s \leq \vec{v}_{ph,\theta,plasma} \leq 14.5km/s$ in the EDD for the WCM
- $4.5km/s \leq \vec{v}_{ph,\theta,plasma} \leq 13.5km/s$ in the IDD for the QCM

The QCM propagates in the opposite direction in the lab frame than in the plasma frame, whereas the WCM has little shift from the $\vec{v}_{E\times B}$ because the value of E_r in the well of the I-mode is very small as opposed to that of the EDA H-mode.

3.4.5 Collisionality regime and q_{95} comparison between I-mode and EDA H-mode

From the previous sections it is clear that, while there are many similarities between the WCM and the QCM, including the k_θ range and radial localization, there are also some clear differences, including direction of propagation in the plasma frame, coherency and poloidal displacement of the peaks.

There are also fundamental differences between the range of operation for the two confinement regimes: I-mode exists in high I_p, low q_{95} plasmas, while the EDA H-mode occurs predominantly in low I_p, high q_{95} regimes. This is seen in Figure 3-7(a). Additionally, and perhaps more importantly in terms of excitation of fluctuations, the collisionality at the edge of the plasma for the regimes is very different. Since the I-mode features high temperatures and low densities at the edge, the collisionality at the edge is very low. For the EDA H-mode, while the temperatures are H-mode like at the edge, the presence of a density pedestal results in an increased collisionality. As shown in Figure 3-7(b), for most I-modes, $\nu^*_{ped} \leq 1$, whereas for typical EDA H-Modes, $\nu^*_{ped} \geq 1$.

3.4.6 Theoretical models of the QCM and the WCM

As initially discussed in Section A.3.2, there is evidence[93] that the model that best describes the physics of the QCM is that of a *Resistive Ballooning mode*[94], particularly that of the Resistive X-point mode[95]. There are several properties of the QCM that are compatible with that of a Resistive Ballooning mode: the mode has an electromagnetic component directly measured by magnetic probes[89] and it has a ballooning nature, being observed at the outboard midplane and not at the inboard side of the plasma[91]. It also resides close to the pedestal region in a high ν^*_{ped} regime. A study using the edge fluid code *BOUT*[96][97][98] was conducted in [93] to ascertain the nature of the mode. By using a 3D nonlocal electromagnetic model, which solves the fluid equations at the boundary of a divertor plasma, *BOUT* is capable of including the effects of many possible instabilities on the equilibrium density, temperature and magnetic field. It was found in the study that the most unstable mode was that of the Resistive X-point mode, which is driven by pressure gradients at the outboard midplane and which becomes electrostatic close to the X-point. It was shown that both the magnetic fluctuation and density fluctuation levels measured for the QCM were consistent with those predicted by *BOUT* for this type of instability.

For the WCM, the ballooning nature of the mode is also present. While there is evidence of a poloidal variation of the intensity of the mode (as discussed in Section 3.3.2), it is clear that for most cases, there is a strong presence of the mode at the outboard midplane, since the two diagnostics that are most sensitive to the mode, GPI and reflectometry, have views that are localized in this region. While an exhaustive study has yet to be conducted, there is currently no evidence of the presence of the mode at the inboard side.

The presence of a magnetic component of the mode, as evidenced by the measured magnetic fluctuations by the fast magnetic coils, shows that the WCM is electromagnetic in nature.

One possible candidate that satisfies these characteristics is the Kinetic Ballooning mode, which is predicted from extensions of the ideal-MHD ballooning mode theory

by incorporating important kinetic effects derived for low collisionality plasmas[99]. Another possible candidate for the mode is a Heavy Particle mode[100][101]. This is a collective mode which arises in the presence of heavy impurities in a hydrogenic plasma. The heavy impurity mode reproduces several of the empirical observations of the WCM well: the outward ejection of impurities, the presence of density, temperature and magnetic fluctuating field components, and propagation in the electron diamagnetic direction for the poloidal phase velocity of the mode in the plasma frame. The main drive for this mode is the ion temperature gradient at the edge of the plasma. Since several of the mode characteristics described by the Heavy Particle mode, such as the mode frequency and velocity in the plasma frame, depend on the atomic number of the main impurity in the plasma, a possible experimental way of testing for this mode is to systematically change the type of injected impurity in, otherwise, identical discharges, and measuring changes in the mode.

The drive of the Kinetic Ballooning mode is the pressure gradient at the edge of the plasma which, for the I-mode, is dominated by the edge temperature gradient. Nevertheless, this is also a drive for the Heavy Particle mode, therefore testing for the Kinetic Ballooning mode experimentally could be challenging.

While the present work does not attempt to determine the physical mechanism behind the WCM, one of the ultimate goals in the study of these fluctuations should be tests of the theoretical models against the empirical observations of the mode. This should be done both by controlled experimental studies focused on discerning the primary dependencies of the models, as discussed above, as well as through the use of benchmarked codes (similar to *BOUT*) which incorporate the relevant physics necessary to describe the edge of I-mode plasma, including, the low collisionality at the pedestal. This will be discussed further in Section 6.3.

3.4.7 QCM and particle transport across the LCFS of the EDA H-Mode

It is clear is that both the I-mode and the EDA H-mode are steady state regimes that feature high energy confinement, yet typically lack ELMs. It is reasonable to conjecture that the presence of WCM and QCM fluctuations, respectively, can be linked to the impurity ejection that is essential to the steady state nature of each regime.

Since its discovery, the QCM has been seen to always accompany the EDA H-mode confinement regime[5][89][93]. This, and the fact that the QCM is radially localized near the edge of the plasma, where it could flush impurities from the plasma, led to the hypothesis that the QCM was responsible for the reduction in impurity accumulation. In order to make a more direct comparison between the particle transport across the LCFS and the amplitude of the QCM, a study was conducted[102][91][25] wherein the particle flux was measured across the LCFS of the EDA H-mode plasma and the effective diffusivity was evaluated, with $D_{eff} \equiv |\Gamma_{LCFS}/\nabla n_e|$, and the ∇n_e term is evaluated at the LCFS. The D_{eff} was then compared with the amplitude of the QCM to determine its dependence on the fluctuation.

To estimate the magnitude of the particle flux across the LCFS, a particle transport model, developed in detail in [103], uses a particle conservation equation inside the LCFS. The particle source is estimated from Lyman α measurements from an array (shown in Figure 3-20a) and the changes in density were measured to be negligibly small for the discharges studied.

The amplitude of the QCM is measured from the autopower of the PCI diagnostic signals.

As the amplitude of the QCM varies throughout the EDA H-mode, the measured D_{eff} is observed to vary proportional to it, as seen in Figure 3-20b. This finding solidifies the argument that the QCM is, in fact, responsible for the particle transport regulation across the LCFS, maintaining the EDA H-mode in steady state.

The natural question that follows is does, in fact, the WCM play a similar role in

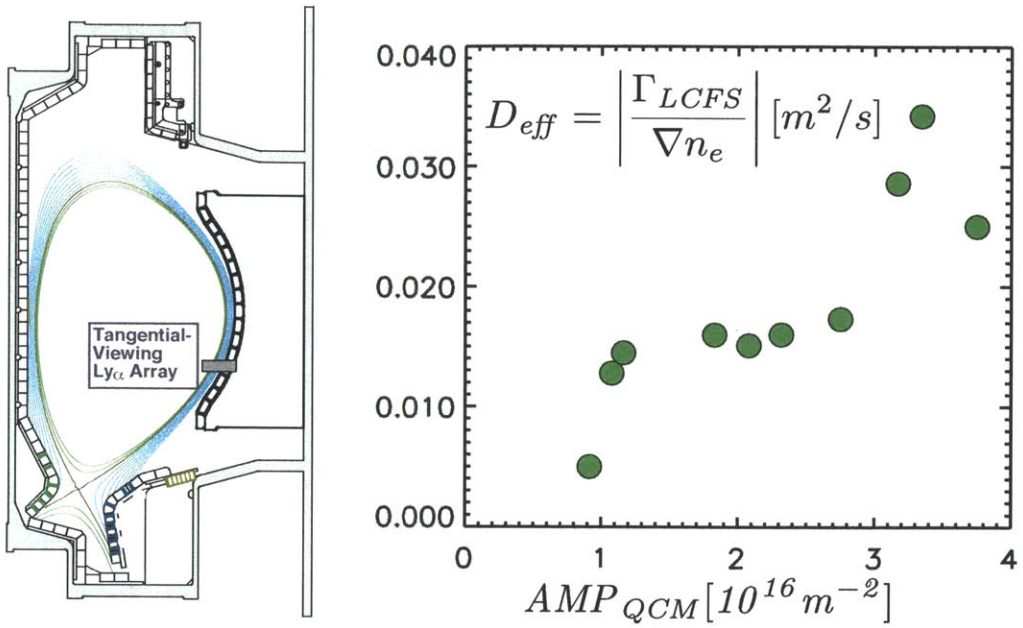

(a) (b)

Figure 3-20: a)In order to estimate the particle transport across the LCFS for the EDA H-mode, a Lyman α array was used to measure the ionization rate and, through a local particle conservation model, estimate Γ_{LCFS}. b) By comparing the effective diffusivity at the edge of the plasma, as defined in the figure, and the amplitude of the QCM, a strong correlation is found, which supports the causal relationship between the QCM and the particle regulation in the EDA H-mode.

the particle transport for the I-Mode? With a few exceptions, the WCM is also a signature of the I-mode and its radial location is also limited to the steep temperature pedestal region of the plasma. The last piece of the puzzle, analogous to the QCM, is to find a relationship between the particle flux across the LCFS and the strength of the WCM. The results of experiments and models to explore this question are detailed in Chapters 4, 5 and 6.

3.5 Modeling the fluctuation spectra

The characteristic edge fluctuation phenomena of the I-mode are clearly measured with the O-mode reflectometer. In particular, the presence of the WCM is observed in the reflectometry autopower, and hence, autospectrum, as seen in Figure 3-19. The

autopower, $\zeta(f)$, of the complex electric field signal, is the Fourier transform of the complex $I(t) + iQ(t)$ signal, described in Section 2.2.3, and can be rewritten as:

$$\zeta(f) = \left| \frac{T}{N} \sum_{j=0}^{N} (I_j(t) + iQ_j(t)) e^{-2\pi ijf/N} \right|^2 \tag{3.3}$$

where f is the spectral frequency, T is the period during which the autopower is taken, and N is the number of data points used to derive the autopower. In this study, the autopower is calculated at $T = 1$ms intervals, and therefore $N = 2000$. As discussed in Sections 2.2.2 and 2.2.3, the autopower of the complex signal qualitatively reproduces the effects of density fluctuations close to the cutoff layer of the reflectometry channel better than the simpler $\tilde{\phi}$ signal, since the 2D effects and the large $\tilde{n}_e/n_e \gg 1\%$ of the WCM break the assumptions of the simplified 1D models that rely on the phase fluctuation measurements alone.

As shown in Figure 3-21, during the I-mode, the autopower features a broadband component of the fluctuations (albeit reduced by the midrange fluctuation reduction discussed in Section 3.3.1), and the WCM. Since, in this experiment, we want to compare the WCM intensity with global particle transport in the I-mode, it is important to distinguish between the broadband fluctuation components and the WCM. To this end, we have developed method to isolate the WCM component within $\zeta(f)$.

We find that $\zeta(f)$ in I-mode can be well parametrized by using the following empirical model:

$$\zeta(f) = Ae^{-\frac{f}{f_1}} + Be^{-\frac{f}{f_2}} + Ce^{-\frac{(f-f_{WCM})^2}{w^2}} \tag{3.4}$$

In this model, the broadband component of the fluctuations can be reproduced using the two linearly independent exponential decay terms, $Ae^{-\frac{f}{f_1}}$ and $Be^{-\frac{f}{f_2}}$. The WCM component is represented by the Gaussian term, $Ce^{-\frac{(f-f_{WCM})^2}{w^2}}$. All variables: A, B, C, f_1, f_2, f_{WCM} and w are free parameters. In order to find a suitable set, a fitting routine based on the Levenberg-Marquardt algorithm[104] has been developed, which minimizes the χ^2 error in the fit of an autopower signal taken during a 1ms time interval (2000 samples).

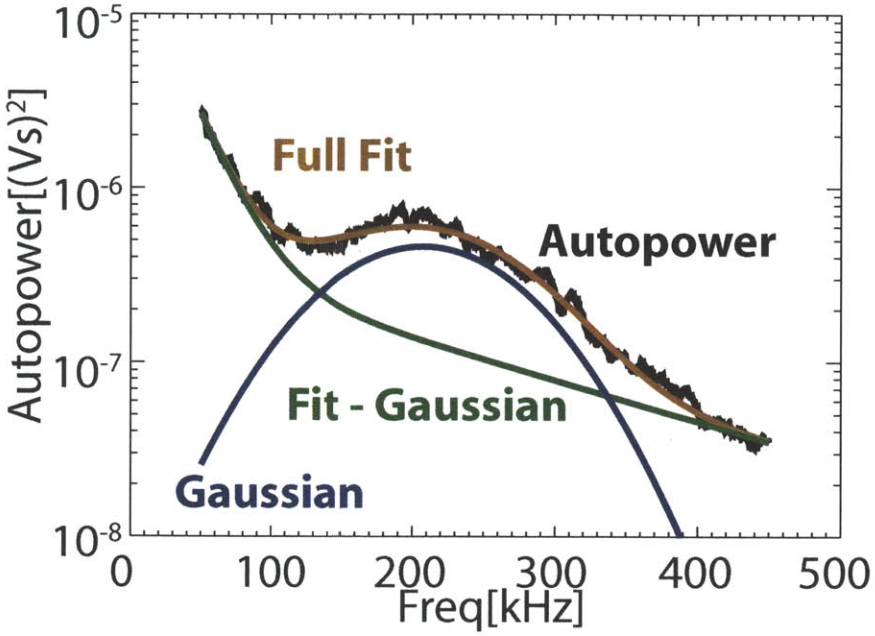

Figure 3-21: a) The autopower of the complex signal, $I + iQ$ (in solid black), during the I-mode can be modeled as a sum of two exponential decays (in green) describing the broadband fluctuations and a Gaussian component (in blue) describing the WCM at $\sim 200kHz$. The full fit is plotted in red.

A typical example is shown in Figure 3-21, in which the broadband $Ae^{-\frac{f}{f_1}} + Be^{-\frac{f}{f_2}}$ components of $\zeta(f)$ can be seen in the green line, and the Gaussian, $Ce^{-\frac{(f-f_{WCM})^2}{w^2}}$ is shown in blue. The total fit is shown in red, which is seen to fit well the total autopower.

This procedure can be followed for the whole shot, and the full autospectrum can be reconstructed. An example is shown in Figure 3-22, which displays the full reconstruction in the top plot, only the exponential decay terms in the middle plot and only the Gaussian component in the bottom plot. As expected, the middle plot, which contains the broadband component only, clearly shows the midrange fluctuation reduction when transitioning from L- to I-mode (at t=1.14s) and then, a further reduction when transitioning to the H-mode (t=1.23s).

The need for two exponential decay components to describe the broadband comes

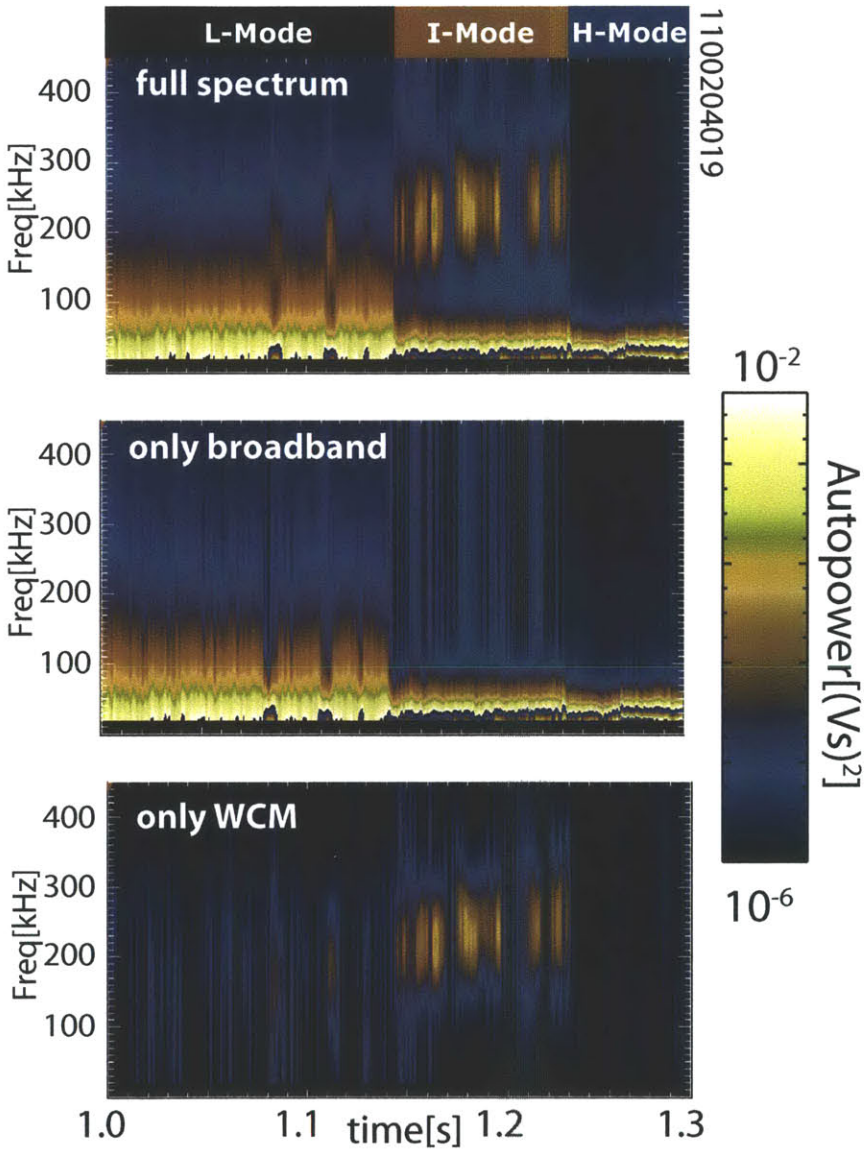

Figure 3-22: The autospectra reconstruction of a shot during L-Mode, I-Mode and ELM-free H-mode plasmas based on the parametrization described. The first plot shows the full spectrum, the second plot shows only the broadband components, the third plot shows only the WCM/Gaussian term.

from a comparison with a model where the simplified assumption is used:

$$\zeta(f) = Ae^{-\frac{f}{f_1}} + Ce^{-\frac{(f-f_{WCM})^2}{w^2}} \tag{3.5}$$

A comparison between fits of the autopower signals using both, the single exponential decay model, as well as one with 2 exponential decays, is shown in Figure 3-23.

As for Figure 3-21, the red traces in the plots are the fits to the autopower signals (black), the green traces indicate the exponential decay terms, and the blue Gaussian describes the WCM components. For the top row of plots, the full 2 exponential decay model (Equation 3.4) is used for the fit, whereas for the bottom row, the single decay model (Equation 3.5) is used.

While the single exponential decay model describes the L-mode broadband appropriately, during the I-mode, there is a significant discrepancy between the modeled fit and the autopower, especially at the frequencies where the strength of the WCM starts to become of the same order of the broadband (at $\sim f_{WCM}/2$). The two bottom-middle plots, for example, show a discrepancy between the fit and the signal at around 100kHz.

By calculating the reconstructed autospectra, as in Figure 3-22, the individual components of the fit can be isolated for each of the two models. This is done for the same discharge as in Figure 3-23, and is plotted in Figure 3-24. While the two models do a reasonably good job reconstructing the discharge, especially during the L-mode, the single exponential model (bottom row) shows the expected discrepancies in the broadband during the I-mode seen in Figure 3-23. The single decay model typically overestimates the level of broadband fluctuation and misses changes, like the increase in broadband signal at $\sim 1.2s$ which is reproduced by the full model (top row). The WCM-extracted autospectra reflect these discrepancies. For example, while the full model shows the strong WCM at $t \sim 0.8s$ seen from the signal, the simpler model doesn't show the WCM as strongly. In general, the strength of the WCM is underestimated by the single decay model.

While the differences between the two models are subtle, and in most cases they're

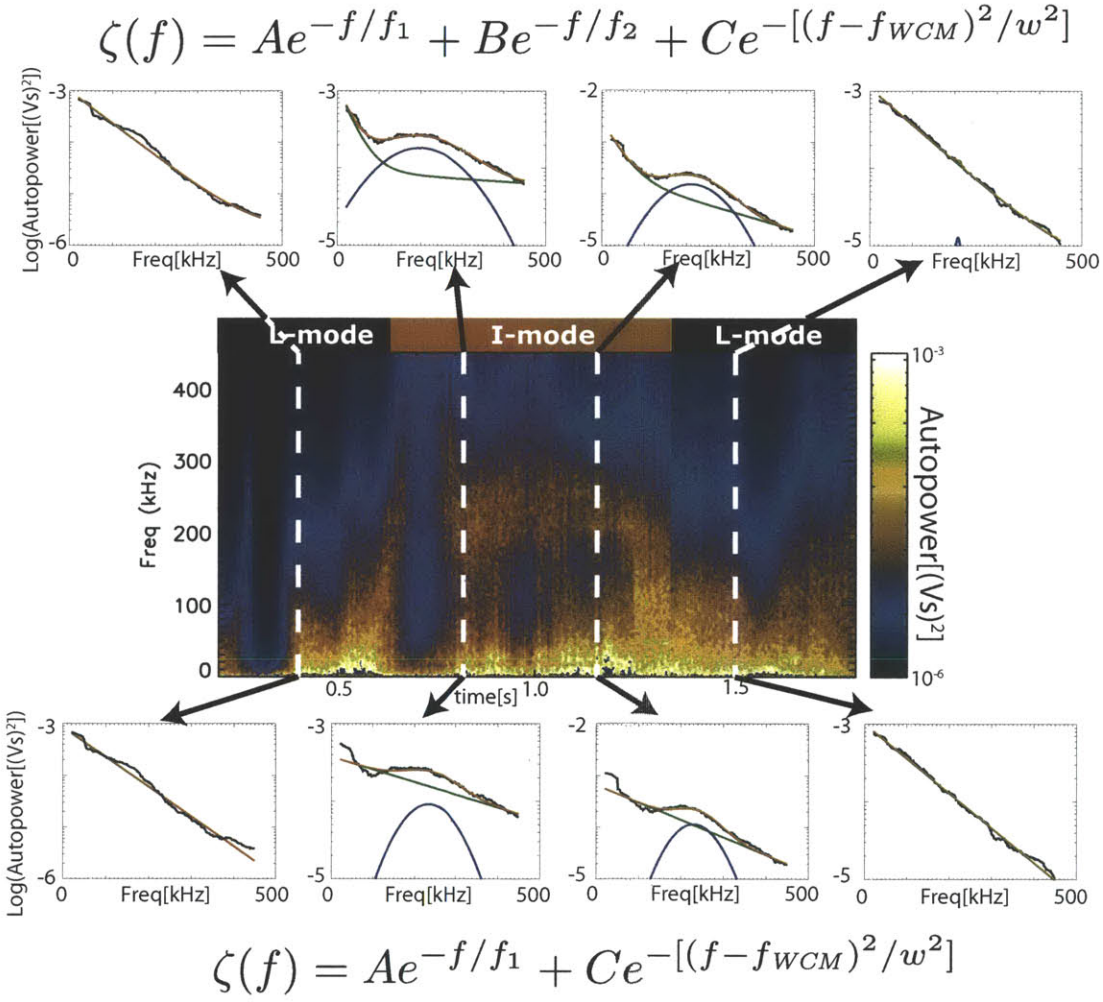

Figure 3-23: Two models, one with 2 exponential decay terms (top row) and the second with 1 exponential decay term (bottom row), are used to fit the autopower signal. The black trace is the original signal, the red trace is the model fit. Using only one exponential decay term, the fit reproduces the features of L-mode spectra well (as in the leftmost and rightmost plots), but fails to describe well the autopower during the I-mode, especially for low frequencies of the autopower (around 100kHz). Using two decay terms, as is done for the top plots, the model fits well to the full autopower in both the L-mode and the I-mode regimes.

interchangeable, it is important to try to optimize the method for extracting the WCM, since in many cases the WCM is a subtle phenomenon. From this point on, the only model used is the one with 2 exponential decays.

By focusing on the Gaussian term, the WCM contribution of the fit can be isolated. To take into account the full spectral contribution of the WCM, we define the WCM intensity as:

$$\mathrm{I}_{WCM}(t) = \int_{f_0}^{f_1} Ce^{-\frac{(f-f_{WCM})^2}{w^2}} df \tag{3.6}$$

where $f_0 = 10kHz$ and $f_1 = 500kHz$ is the range over which the autopower is analyzed, and which encompasses the WCM, which peaks at $\sim 250kHz$. $\mathrm{I}_{WCM}(\mathrm{t})$ is used as a relative estimate for the local density fluctuation component, $\tilde{n}_e$, at the cutoff location, and is analogous to the AMP_{QCM} used in Section 3.4.7.

It is important to note that in the case of the I-mode, as opposed to the EDA H-Mode, the WCM component in the autopower signals has a much lower signal to noise within the rest of the autopower trace than is typical for the QCM. This is the reason that the spectral modeling of the autopower signal is necessary for the WCM study, since the signal has to be extracted from the background fluctuations present during the I-mode.

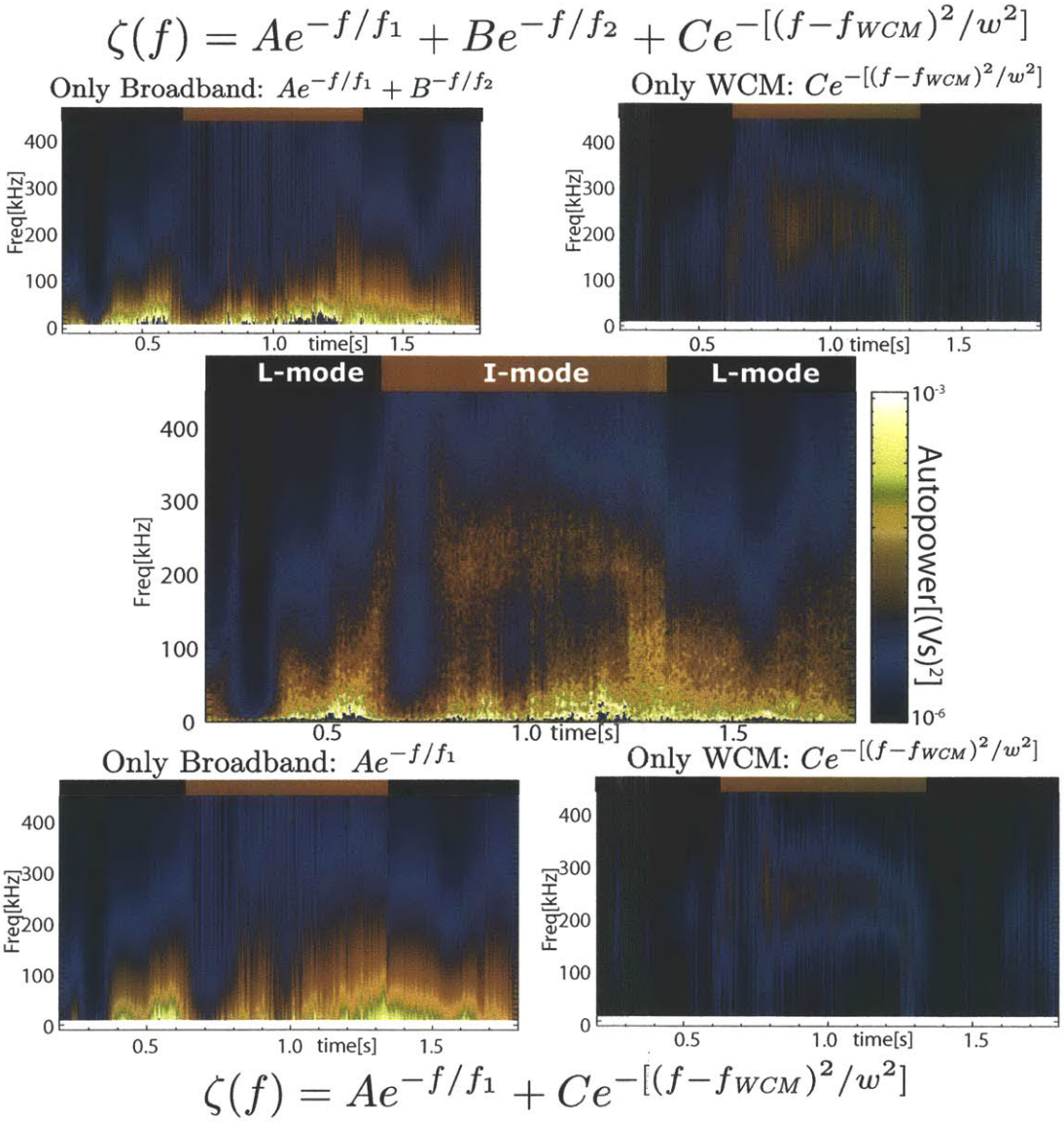

Figure 3-24: By doing individual fits to the autopower of the complex signal, $I+iQ$, for 1ms intervals during the whole discharge, the reconstructed autospectra are obtained. As for Figure 3-23, two models, one with one exponential decay and one with two exponential decays are compared. As expected from Figure 3-23, the broadband component of the autospectrum is not well reconstructed by the single exponential decay for the I-mode period (bottom-left plot), leading to a bad reconstruction of the WCM part (bottom-right). The two decay model (top right) does a much better job than the one decay model (bottom right) of reconstructing the spectra during the I-mode phase ($t \sim 0.85s$). Note, the same range is used for the color scales in all plots.

Chapter 4

Particle Transport

4.1 Discussion on particle transport measurements across the LCFS

The measurement of the intensity of the WCM has been defined in Section 3.5. In order to compare the WCM amplitude with the particle transport across the LCFS, the latter has also to be measured along with the WCM.

Particle transport at the edge of the plasma is important for understanding the physical mechanism of equilibration between the hot, dense environment of the core plasma and the cold, neutral scrape off layer (SOL) and vessel walls and divertors, as well as for predicting the particle and energy flux expected on plasma facing components (PFCs) in future machines[105][103][106].

A steady state model of the particle transport in Alcator C-Mod was developed in [103], which assumes a steady state equilibrium ($dn/dt = 0$), and estimates divertor effects as $\nabla_{\|} \cdot \vec{\Gamma}_{\|}$ terms in a particle conservation equation of the form:

$$\vec{\Gamma}_{\perp}(\rho) = \int_{\rho_{min}}^{\rho} [S_{ion} - \nabla_{\|} \cdot \vec{\Gamma}_{\|}] d\rho' \tag{4.1}$$

where S_{ion} is measured from Lyman α measurements (to be discussed), ρ is a radial variable inside the LCFS, and ρ_{min} is the minimum radial location where the Lyman

α radiation goes to zero. Since the ionization source is measured at the Lyman α array location (see Figure 3-20b(a)), the flux measurement is a local one.
As will be discussed later in this chapter (Section 4.2.2), a modified model which uses some of the elements developed in [103], while incorporating others (such as relaxing the steady state assumption), has been used for the present study. Nonetheless, as in [103], the particle flux, Γ, is derived from the local particle conservation equation:

$$\nabla \cdot \Gamma + \frac{\partial n}{\partial t} = S. \tag{4.2}$$

If the particles of interest are the deuterium ions in the plasma, the source term, S, refers to the ionization density that occurs in the first few millimeters inside the LCFS. As the neutral atoms enter the hot dense plasma region, ionization occurs. In the following section, the details of the ionization source measurements are explained, as is the full model used to estimate the cross-field particle transport across the LCFS.

4.2 Description of D_α measurements and particle transport model

4.2.1 Experimental description of D_α measurements

As the neutral deuterium atoms encounter the plasma, the atoms become excited and ionized. As described in [107], an equilibrium is reached between the excited states, the ground state and the ionized state of the deuterium atoms and, for high enough temperatures (satisfied at the plasma edge), the ionization rate of the deuterium atom is approximately proportional to the density of any occupied state[107]:

$$\textit{Ionization rate} \approx n(p)\left(\frac{n_e S n_E(1)}{r_1(p) n_E(p)}\right) \tag{4.3}$$

where p is the excited state, S and $r_1(p)$ are two of the Johnson-Hinnov coefficients, which have been derived empirically and can be found in [107], or, indirectly in the

ADAS databases[1], and $n_E(p)$ is the Saha equilibrium occupation density of the p^{th} excitation level:

$$n_E(p) = n_{(D^+)} n_e p^2 \left[\frac{h^2}{2\pi m k T_e}\right]^{3/2} e^{E_{i,p}/kT_e} \tag{4.4}$$

where $n_{(D^+)}$ refers to the density of the ionized deuterium, h and k are the Planck and Boltzmann constants, and $E_{i,p}$ is the ionization potential of the p^{th} state. The Saha equilibrium occupation describes, in effect, a Maxwell-Boltzmann equilibrium between the p^{th} state and the fully ionized state. Note that S, $r_1(p)$ and $n_E(p)$ are all functions of the local T_e and n_e.

The final piece of the puzzle comes from the *spontaneous emission* rate for transitions from $a \rightarrow b$. The rate at which an atom in an excited state ,"a", decays by radiation to a lower state, "b", is proportional to the population in the excited state, as: $dn(a)/dt|_b = -A_{ab}n(a)$, where $dn(a)/dt|_b$ is the change in density in the excited state "a" due to $a \rightarrow b$ transitions, and A_{ab} is the Einstein coefficient (which depends only on the type of atom and the transition states). Since every transition emits a photon with energy $\hbar\omega$, the emission at the spectral line of wavelength $\lambda = 2\pi c/\omega$ can be selectively detected and the number of $a \rightarrow b$ transitions can be deduced.

By measuring light around $\lambda = 656nm$, the light emitted in the Balmer $3 \rightarrow 2$ transition (or D_α light for deuterium) can be detected and, by using the $A_{3,2}$ coefficient, and Equation 4.3, the ionization source rate density (in $[m^{-3}s^{-1}]$) can be deduced from the local light emissivity (in $[Wm^{-3}]$) of the D_α light.

To measure the D_α light, a fast visible spectrum camera is used with a magnetic field aligned field of view, as shown in Figure 4-1. The camera uses an interference filter centered at $\lambda = 656nm$ with a bandwidth of $\Delta\lambda = \pm 5nm$ to image the D_α radiation. While the system shares much of the geometry (and hardware) with the GPI system described in Section 2.3.1 and shown in Figure 2-21, there are some important differences. While the GPI has a 9×10 viewing array, the visible camera has a 64×64 array, suitable for detailed profile measurements across the LCFS. For the camera, the lines of sight are inclined by 10 degrees from the horizontal which makes them

[1]Which, at present can be found here: http://www.adas.ac.uk/manual.php

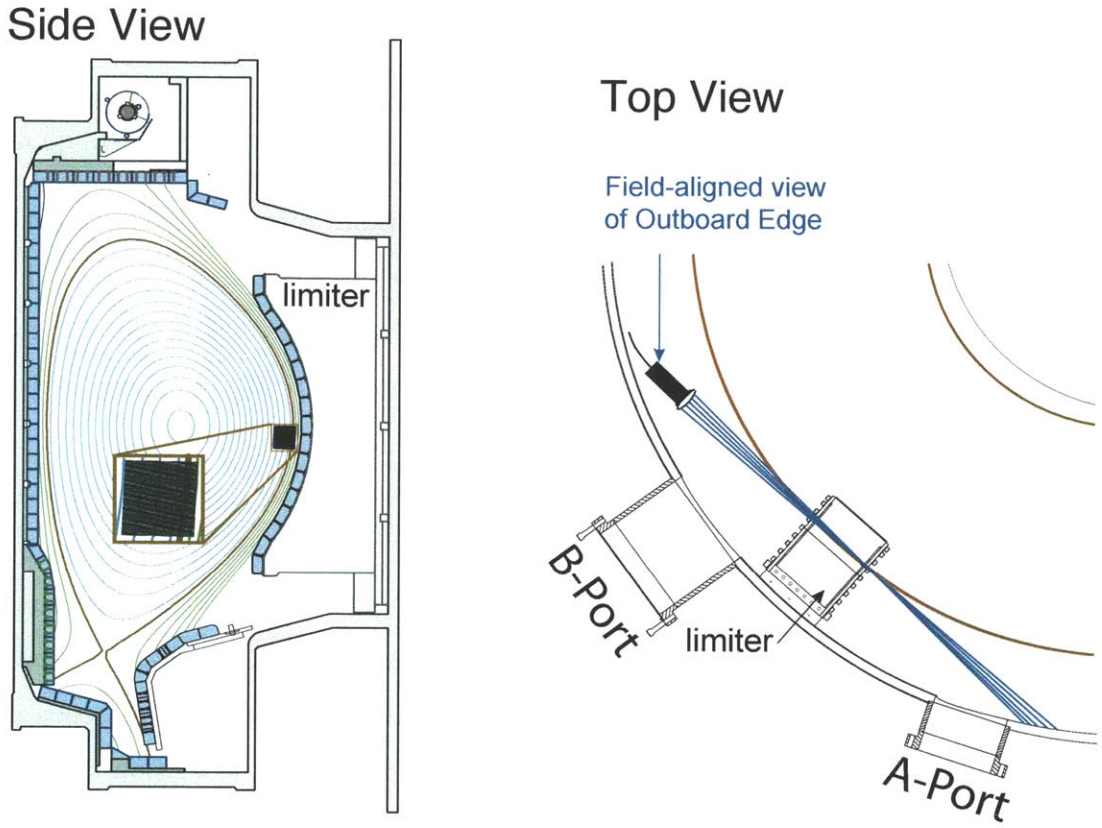

Figure 4-1: The fast visible spectrum camera has a 64×64 viewing array, straddling the LCFS at the outboard midplane. The lines of sight are parallel to the local magnetic field at $I_p \approx 1MA$ and measure the line integrated brightness. Since no deuterium gas puffing is used, the background emissivity profiles at a given spectral line (D_α filtering is used for the work presented), can be obtained.

aligned with the total magnetic field at the radial position of the viewing array for plasmas with $q_{95} \approx 4$. This is a minor change from the GPI system which is aligned in the toroidal ($\hat{\phi}$) direction.

The most important distinction is that, as shown in Figure 4-1, in order to acquire radial profile data, no D_2 gas puffing is used. As described in Section 2.3.1, for GPI, the gas puff is used to localize the line integrated brightness measurements to the puff region. The measured brightness can then be assumed to be due to emissivity which is toroidally localized at the puff. For the camera, the line integrated brightness measurements are due to the emissivity along the whole line of sight. In practice, at each

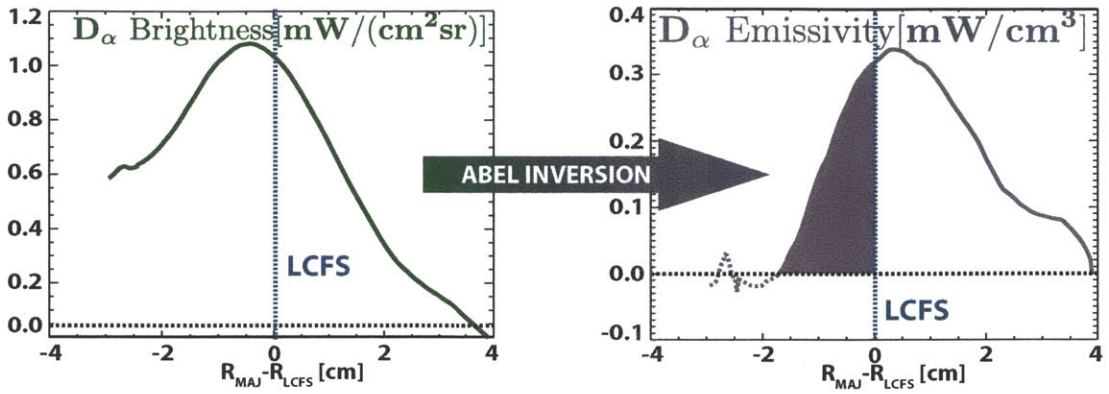

Figure 4-2: Since there is no local deuterium puffing along the lines of sight during these plasma discharges, the brightness profiles obtained by the fast visible camera can be Abel inverted to measure the D_α emissivity radial profiles. These can then be used to infer the local ionization source density.

radial location, 35 chords, poloidally spanning approximately 3.5cm, are averaged to obtain a single brightness measurement at the specific radial location. By then measuring a radial brightness profile up to, and across the LCFS, the D_α emissivity can be deduced by applying an Abel inversion on the brightness profile, as shown in Figure 4-2. This requires that there be no local sources of emissivity along the line of sight; hence the requirement that D_2 not be puffed during the time of data acquisition. Note that, in order to apply the Abel inversion, the brightness measurements at the outermost radii must be much lower than the maximum measured brightness values. Empirically this is done by ensuring that the $Bri(max)/Bri(edge) \geq 4$ for every time slice, which is satisfied for the discharges studied.

After the Abel inversion, the result is a radial emissivity profile, which can be used to measure the local deuterium ionization source rate density, S (Equation 4.2) by using the Johnson-Hinnov coefficients, as discussed above. Since these coefficients depend on the local n_e and T_e values, density and temperature profiles measured with Thomson scattering are used for this step in the analysis.

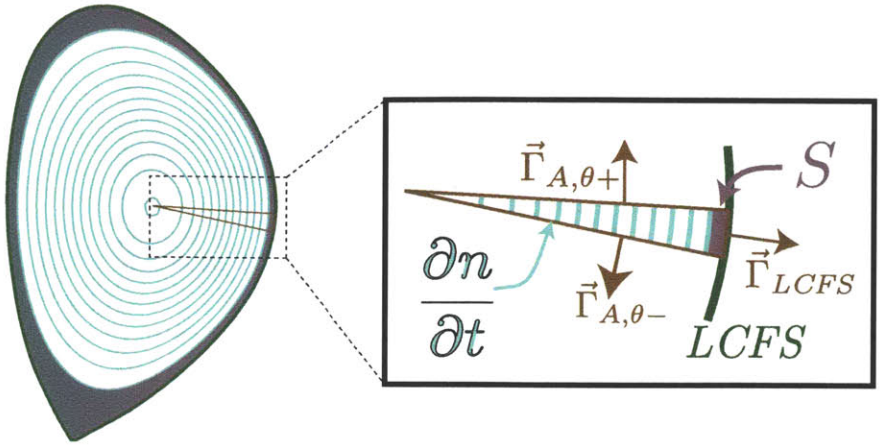

Figure 4-3: The local particle continuity equation is applied to individual *wedge* differential elements. The source density is restricted to the neutral-plasma interaction zone within the LCFS (shown in purple), the $\partial n/\partial t$ term comes from contributions throughout the whole wedge elements and the flux can be divided into Γ_{LCFS}, across the LCFS and $\Gamma_{A,\theta+}$ and $\Gamma_{A,\theta-}$ of flux crossing to the poloidally adjacent wedge element above and below respectively. As the wedges are added to create an integrated particle flux equation, all the $\Gamma_{A,\theta+}$ contributions cancel out with the $\Gamma_{A,\theta-}$ term from the element poloidally above.

4.2.2 Slab Model used for global transport measurements

The particle transport equation in its differential form (Equation 4.2), can be used within a differential wedge element as shown in Figure 4-3 extending from the plasma center to the LCFS[108]. Note that the elements extend in the $\hat{\phi}$ direction, forming toroidal wedge-like rings. Nonetheless, due to axisymmetry, this dimension can be ignored in the discussion.

If the differential elements are taken as described, the individual components from Equation 4.2 can be identified. The flux components can be divided into the Γ_{LCFS} component, describing flux across the LCFS, and the Γ_A components, describing particle flowing from wedge to wedge. The $\partial n/\partial t$ term comes from particle contributions throughout the whole wedge element, and as will be discussed later, plays an important role in the overall flux measurements. Finally, since Alcator C-Mod has no core fueling mechanism (such as NBI), the source density term, S, is restricted to the neutral-plasma interaction region, within the first few centimeters inside the LCFS.

As shown in the sample emissivity plot in Figure 4-2, after approximately 1.5cm inside the LCFS (shown in solid purple), the D_α emissivity goes to zero. The ionization region is shown in purple in Figure 4-3.

Having defined the infinitesimal elements, the total particle transport across the LCFS can be derived by adding the individual wedge elements poloidally, integrating Equation 4.2:

$$\int (\nabla \cdot \Gamma) dV = \int S dV - \int (\frac{\partial n}{\partial t}) dV \tag{4.5}$$

$$\oint_{LCFS} \Gamma \cdot dA = \int S dV - \frac{\partial \langle n \rangle V}{\partial t} \tag{4.6}$$

$$\Gamma_{LCFS} = \frac{\int S dV}{A} - \frac{V}{A} \frac{\partial \langle n \rangle}{\partial t} \tag{4.7}$$

where $\langle n \rangle$ is the volume average density, Γ_{LCFS} is now the average particle flux across the LCFS (where positive is pointing out of the confined plasma) and V and A are the volume enclosed by, and the surface area of, the LCFS, respectively.

The $\Gamma_{A,\theta+}$ term from an individual wedge cancels out with the $\Gamma_{A,\theta-}$ term from the adjacent wedge poloidally above, occurring for all differential elements in the integrated model, therefore, the only flux term remaining is that across the LCFS. This intuitively makes sense, since the only flux path in or out of the main plasma is through the LCFS.

The source term in Equation 4.7 is a function of the poloidal and toroidal location and is not measured everywhere in these experiments. In order to get an estimate of this term, we measure the source density at the midplane LFS using the visible D_α camera:

$$\frac{\int S dV}{A} = \sigma \int_{\Delta r} S_{obs} dr \tag{4.8}$$

where the integral on the RHS is taken radially across the ionization region inside the LCFS (shown in purple both, in the emissivity plot in Figure 4-2, and in the plasma cross-section in Figure 4-3) and S_{obs} is the ion source density measured at the camera view location.

The ion source density term, S_{obs}, is a measurement of hydrogenic ion sources, hence,

it is of the main deuterium and of hydrogen. The main impurity in the shots used in this study is Neon, which was used as seeding to control radiated power[109] and to limit disruptions. During the I-mode, the Ne fraction is about 1.5%, hence, approximately 15% of the electron density is from Ne ($Z_{Ne} = 10$)[110]. Therefore, while the source term is not taking into account the electrons contributed by the main impurities, their contribution is a small fraction of the overall electrons and will be disregarded in the present study.

We introduce a weight factor, σ in Equation 4.8, which is, for now, a free parameter indicating the asymmetry between the measured local source density and the average source density across the whole poloidal and toroidal extent.

An intuitive idea of σ can be attained by analyzing certain limiting values: If the source density were toroidally and poloidally uniform, S_{obs} would equal the average source density and, hence, $\sigma = 1$. If the source density in the camera view were lower than the average source, σ would then be less than 1. Analogously, if the source density in the camera view is higher than the average source density, the σ value would be larger than 1. In Figure 4-4, a schematic of three limiting cases is shown.

Using a time independent value of σ assumes that, throughout the individual analyzed shots, the source distribution is maintained spatially constant. The validity of this assumption, as well as an estimate of the value of σ, will be discussed in Chapter 5.

The final form of the global electron flux equation that is used in the experimental analysis is obtained by substituting the source term from Equation 4.8 into Equation 4.7:

$$\Gamma_{LCFS} = \sigma \int_{\Delta r} S_{obs} dr - \frac{V}{A} \frac{\partial \langle n \rangle}{\partial t} \tag{4.9}$$

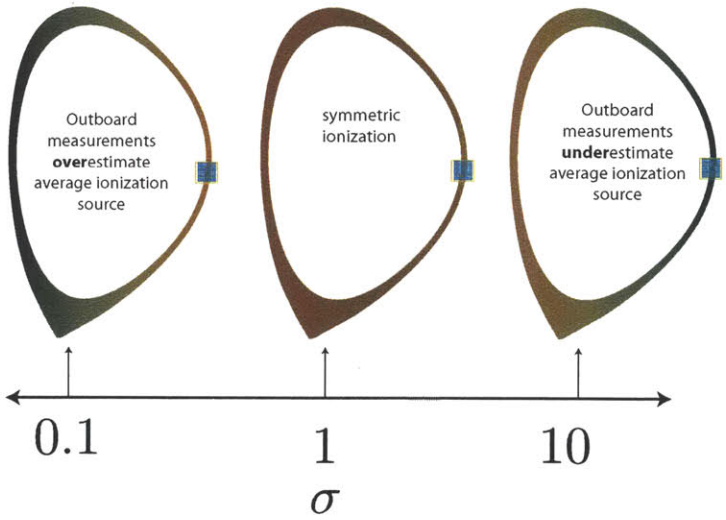

Figure 4-4: To advance from a differential, local particle transport equation to an integrated form which takes into account all of the source contributions to the plasma, it is necessary to introduce a weighing factor, σ, to take into account source density asymmetries around the poloidal cross-section. For $\sigma < 1$, the S_{obs} measured at the fast camera location (shown in the figures), overestimates the average sources in the plasma. For $\sigma > 1$ the measured signal underestimates the average sources. The symmetric case, wherein the measured source density is the same as the average source density, is that of $\sigma = 1$.

Chapter 5

Experiments and results

5.1 Estimate of particle flux from analysis of I-mode to H-mode transitions

The final form of the integrated particle continuity equation in the previous chapter, Equation 4.9, contains the free parameter, σ, which relates the localized source density term, S_{obs}, and the average source density across the whole cross section. By calculating the outward particle flux across the LCFS, Γ_{LCFS}, using I-mode to H-mode transitions, we can impose a constraint on the typical values of Γ_{LCFS} during I-modes and, from this information, evaluate σ. In this section, the methodology used to estimate Γ_{LCFS} is discussed and its value will be used in the next section to constrain σ.

When I-modes, in the unfavorable drift direction topology, (as in Figures 3-3a and 3-3c) transition to H-mode, it is typically an ELM-free H-mode which, as has been discussed in Section A.3.1, is very efficient at containing particles, including impurities, typically leading to subsequent radiative H-mode to L-mode back transitions or disruptions. We will, therefore, assume that in I-mode the net outward particle flux, $\Gamma_{LCFS}(I)$, is much larger than that of the H-mode, $\Gamma_{LCFS}(H)$, which we approximate to zero.

In Figure 5-1, the time trace across an I-mode to H-mode transition is plotted, where

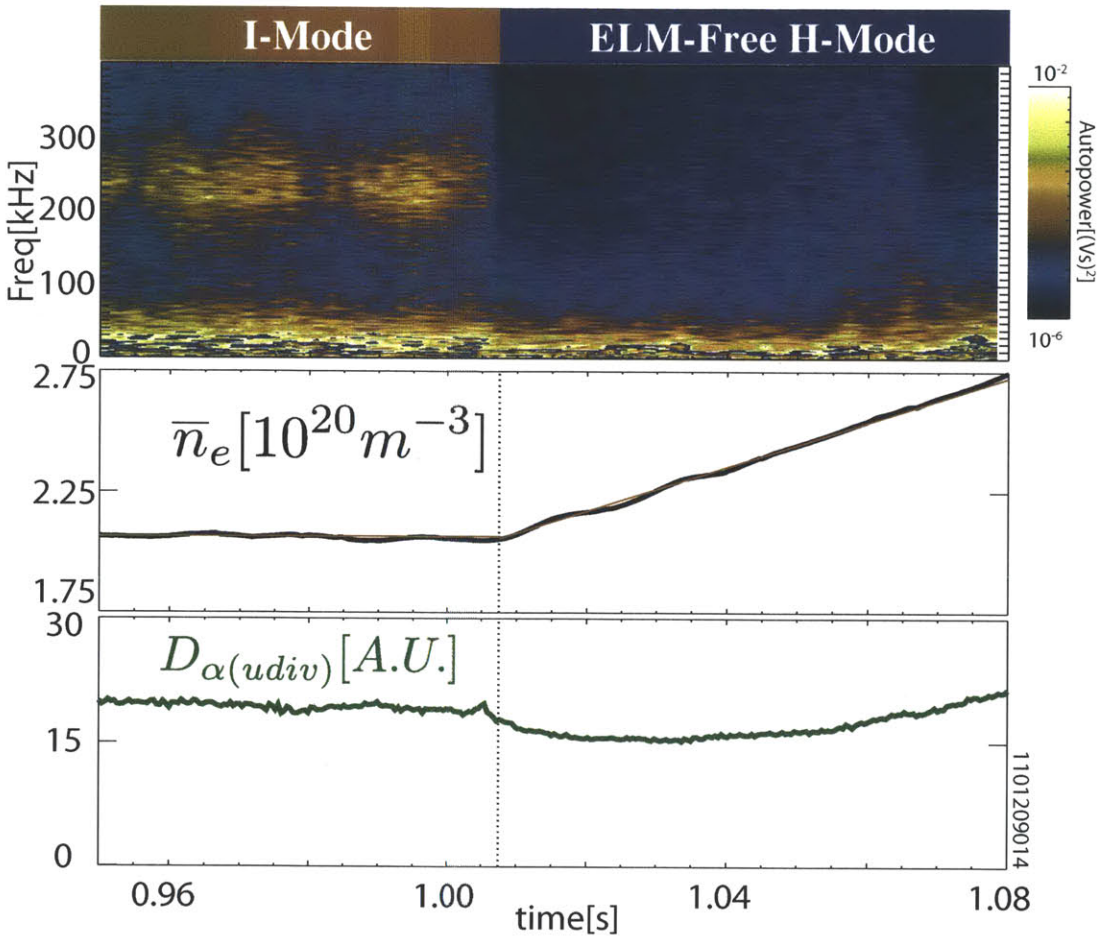

Figure 5-1: A typical I-mode to ELM-free H-mode transition shows a sudden suppression of the WCM accompanied by a break in slope of the average electron density, while the D_α trace, which serves as a proxy for the particle source, stays fairly constant. For this example, the plasma current is 1.2MA and the plasma is in the normal field, USN configuration.

Shot	$\Gamma_{LCFS}(I)[10^{20}m^{-2}s^{-1}]$	$I_p[MA]$	USN/LSN
1091016033	1.5	1.2	USN
1100204019@0.91s	1.6	1.3	USN
1100204019@1.15s	1.1	1.3	USN
1101209014@1s	1.4	1.2	USN
1101209014@1.27s	1.2	1.2	USN
1100827029	0.87	1	LSN

Table 5.1: Γ_{LCFS}(I) deduced from Equation 5.2, using I-H transitions in the normal field configuration.

we observe the suppression of the WCM at the transition to H-mode ($t \approx 1.015s$). This particular discharge has a plasma current of $I_p = 1.2MA$ and was obtained in normal field, USN configuration. $\overline{n}_e$ is constant in time during the I-mode, but after the transition to the ELM-free H-mode, $\overline{n}_e$ linearly increases at a rate of $\sim 10^{21}m^{-3}s^{-1}$. Also observed in Figure 5-1, the D_α brightness time trace for a chord through the top divertor of the tokamak, which serves as a proxy for the ionization source rate, stays fairly constant (changing by no more than $\sim$10%) across the transition. We can therefore use the particle continuity equation, Equation 4.9, from both the I-mode and the H-mode periods, to find an estimate of $\Gamma_{LCFS}(I)$ by equating the source terms:

$$\Gamma_{LCFS}(I) + \frac{V}{A}\frac{\partial \langle n \rangle}{\partial t}(I) = \Gamma_{LCFS}(H) + \frac{V}{A}\frac{\partial \langle n \rangle}{\partial t}(H) \tag{5.1}$$

$$\Gamma_{LCFS}(I) \approx \frac{V}{A}\frac{\partial \langle n \rangle}{\partial t}(H) \approx 1.4 \times 10^{20}m^{-2}s^{-1} \tag{5.2}$$

A similar analysis was done for several high current USN shots in normal field configuration, and a 1MA LSN shot with favorable drift direction. The results are summarized in Table 5.1.

The experiments discussed in Section 5.2, in which the results of the particle transport and WCM analysis are described, and which rely on the estimate of σ, are done in reverse field LSN at plasma currents of 1MA and 1.1MA. Therefore, it is desirable to find I-H transitions in similar configurations. While the vast majority of the

Shot	$\Gamma_{LCFS}(I)[10^{20}m^{-2}s^{-1}]$	$I_p[MA]$
1110316019	0.61	1
1110316020	0.42	1

Table 5.2: Γ_{LCFS}(I) deduced from Equation 5.3, using I-H transitions in the reverse field, LSN configuration.

I-modes, especially those with I-H transitions, have been obtained in USN, normal field, a 1MA reverse field, LSN discharge for which an I-H transition occurs, is shown in Figure 5-2. For this discharge, we have outboard midplane visible camera measurements, which are used to infer the source term, of the form $\int_{\Delta r} S_{obs} dr$, along with $D_{\alpha(udiv)}$ measurements from the upper divertor (which serve as the source proxy for the data in Figure 5-1).

While the density is not strictly constant in time during the I-mode phase, there is a marked change in time derivative when the plasma transitions to H-mode. A modified version of Equation 5.2 can be used to estimate $\Gamma_{LCFS}(I)$:

$$\Gamma_{LCFS}(I) \approx \frac{V}{A}\left[\frac{\partial \langle n \rangle}{\partial t}(H) - \frac{\partial \langle n \rangle}{\partial t}(I)\right] \approx 0.61 \times 10^{20} m^{-2} s^{-1} \tag{5.3}$$

Note that the fact that the $\int_{\Delta r} S_{obs} dr$ term and the $D\alpha_{udiv}$ term have different behaviors at the transition is an indication that, there may be a change in the asymmetry factor, σ, across the transition. Nonetheless, the difference between the measurements is of order 20%, and the current analysis is meant to obtain an *order of magnitude* estimate of Γ_{LCFS}(I).

Two shots featuring I-mode to H-mode transitions in reverse field LSN configuration were analyzed, and the results are presented in Table 5.2.

From the previous analysis, an effective $\Gamma_{LCFS}(I)$ can be estimated for the two currents of interest: for 1MA, $\Gamma_{LCFS}(I) = 0.5 \times 10^{20} m^{-2} s^{-1}$, obtained from the reverse field LSN cases, is used; for 1.1MA, a value of $\Gamma_{LCFS}(I) = 10^{20} m^{-2} s^{-1}$ is used, based on the results from Table 5.1. By using these values, the σ for each current will be estimated in the next section.

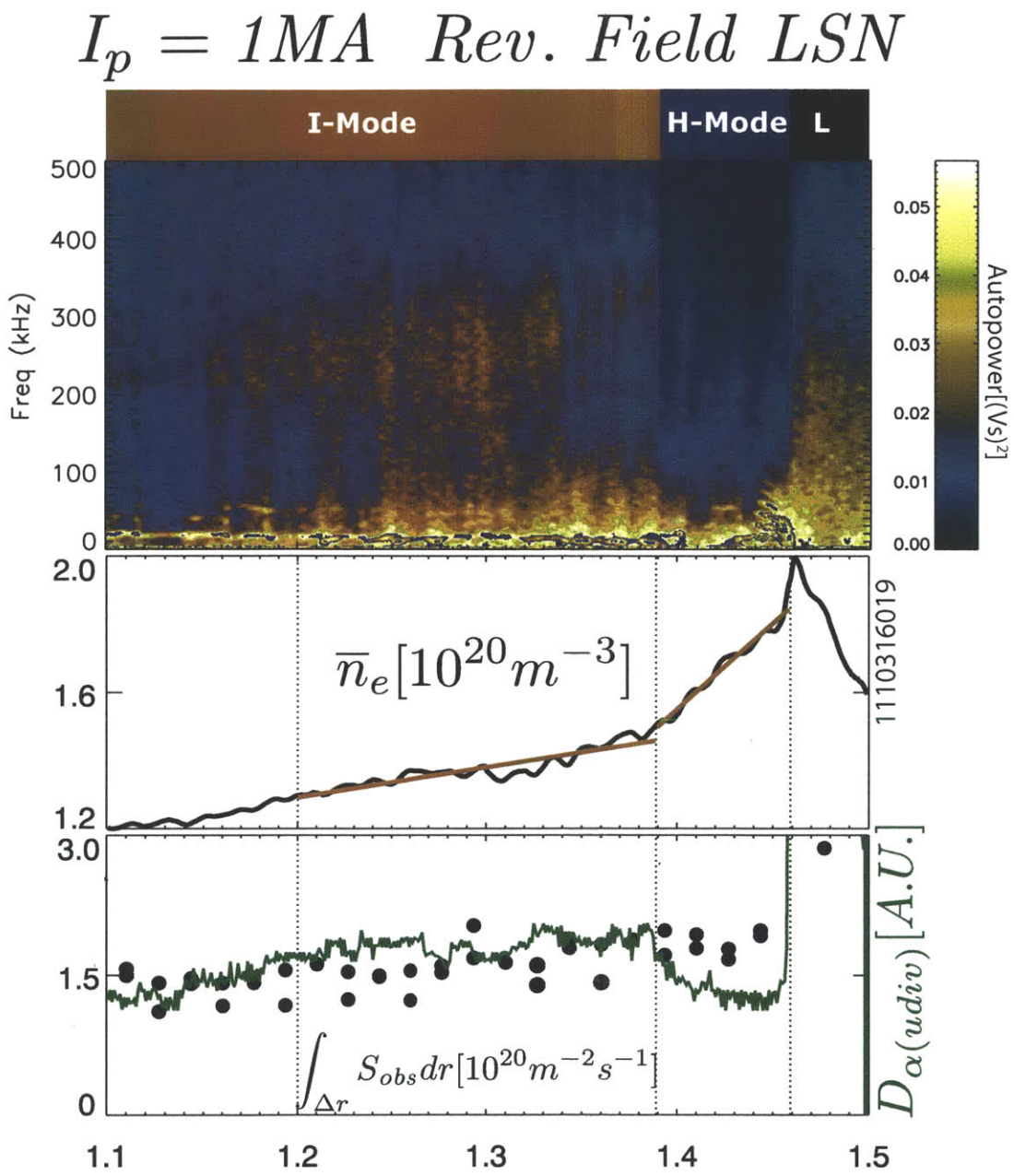

Figure 5-2: An I-mode to H-mode transition in a 1MA plasma, in reverse field LSN configuration, is shown. For this case, the source term from the visible camera D_α array, $\int S_{obs}dr$, is directly measured and is seen to stay constant through the I-H transition. The $D_{\alpha(udiv)}$ measurement decreases by ~20% during the transition. Note that the apparent amplitude decrease of the WCM at the end of the I-mode phase is a consequence of the shift of the cutoff layer of the reflectometry channel (87.5GHz) outside of the region of the WCM.

5.2 Experimental plan

Having defined I_{WCM} from the autopower of the complex reflectometry signal, and derived a model to deduce the net outward plasma particle transport across the LCFS, Γ_{LCFS}, a controlled experiment was conducted to test the relationship between the two variables.

The experimental objective was to create steady state I-modes during which the Γ_{LCFS} and the I_{WCM} were sampled over a wide range of values so as to acquire enough statistically significant data throughout individual shots to look for correlations.

As observed in Figures 3-13 and 5-2, if the reflection layer of any reflectometer channel moves radially away from the steep pedestal region of the I-mode, that channel will no longer detect the peak of the WCM. In order to make sure that changes in the detected signals are due to intrinsic changes in the mode and not from movement of the cutoff layer away from the WCM region, the line averaged density throughout the shot is kept as constant as possible; this sometimes requires the use of external gas puffing, which is a topic that will be dealt with later in this chapter.

As discussed in Chapter 3, the main plasma parameter on which the WCM has been observed to be dependent, is the stored energy, W. The stored energy can be varied by changing the plasma current, I_p, or the input power, P_{tot} (see Figure 3-5). As shown in Figure 5-3, as the plasma current is raised, the coherence of the WCM, defined as $f_{cent}/\Delta f$, increases. Similarly, the intensity of the WCM is larger for the high current cases.

The initial experimental approach included setting different I_p values for a given line averaged density, $\overline{n}_e$. It was found that as the current is raised, the density at which the I-mode is accessible is increased, and, for a given $\overline{n}_e$, there was at most one I_p value for which steady state I-modes were accessed.

The second approach to varying the stored energy is by changing the auxiliary power supplied to the plasma, that is, by varying the P_{ICRF}. This is a natural approach since the L-mode to I-mode transition has historically been accessed by varying the auxiliary power to the plasma. For fixed I_p, as the P_{ICRF} is increased, the stored

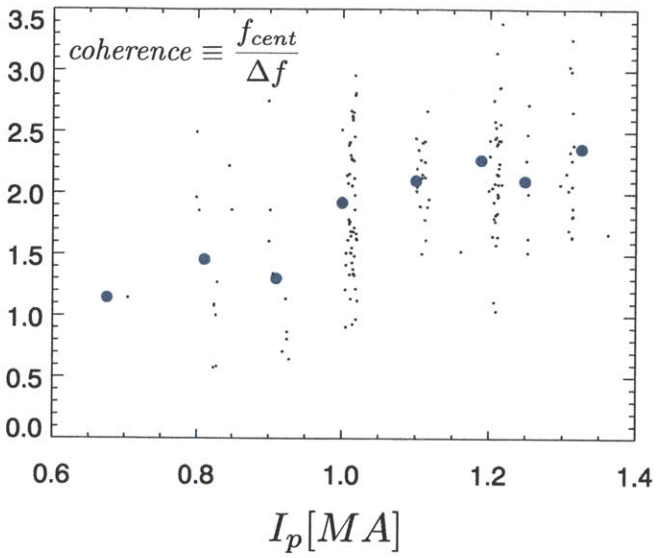

Figure 5-3: The coherence of the WCM signal, defined as $f_{cent}/\Delta f$, measured by reflectometry, shows increases as the plasma current, I_p. The large blue dots are the binned averages of the coherence from individual measurements (small black dots).

energy increases almost linearly (as shown in Figure 3-5), while $\overline{n}_e$ remains fairly unchanged.

In the experiment, the P_{ICRF} was stepped throughout the shot in $100ms$ intervals within a power range where the regime stayed in I-mode. Typical scans ranged from about $2MW$ to $4MW$, as shown in Figure 5-4.

In Figure 5-4, time traces of a discharge used in the experiment are shown. The I-mode is maintained for approximately 550ms or $\sim 18\tau_E$, for a P_{ICRF} range of 1.8-3.8MW, during which the central temperature increases by approximately 45% on average. Meanwhile, the line averaged density stays within 5% of the L-mode density range. As discussed, the plasma current is kept constant throughout the shot, in this example at $I_p = 1MA$.

For this work, toroidal magnetic field of $B_T = 5.74T$ and plasma currents of $I_p = 1MA$ and $1.1MA$ were used, leading to edge safety factors of $q_{95} = 3.9$ and $q_{95} = 3.6$, respectively. These are well within the lower range of q_{95} for which I-modes have been accessed[3]. For those ranges, the average density in the I-mode was $\overline{n}_e = 1.18 \times 10^{20} m^{-3}$ and $\overline{n}_e = 1.41 \times 10^{20} m^{-3}$, and corresponding densities at the LCFS

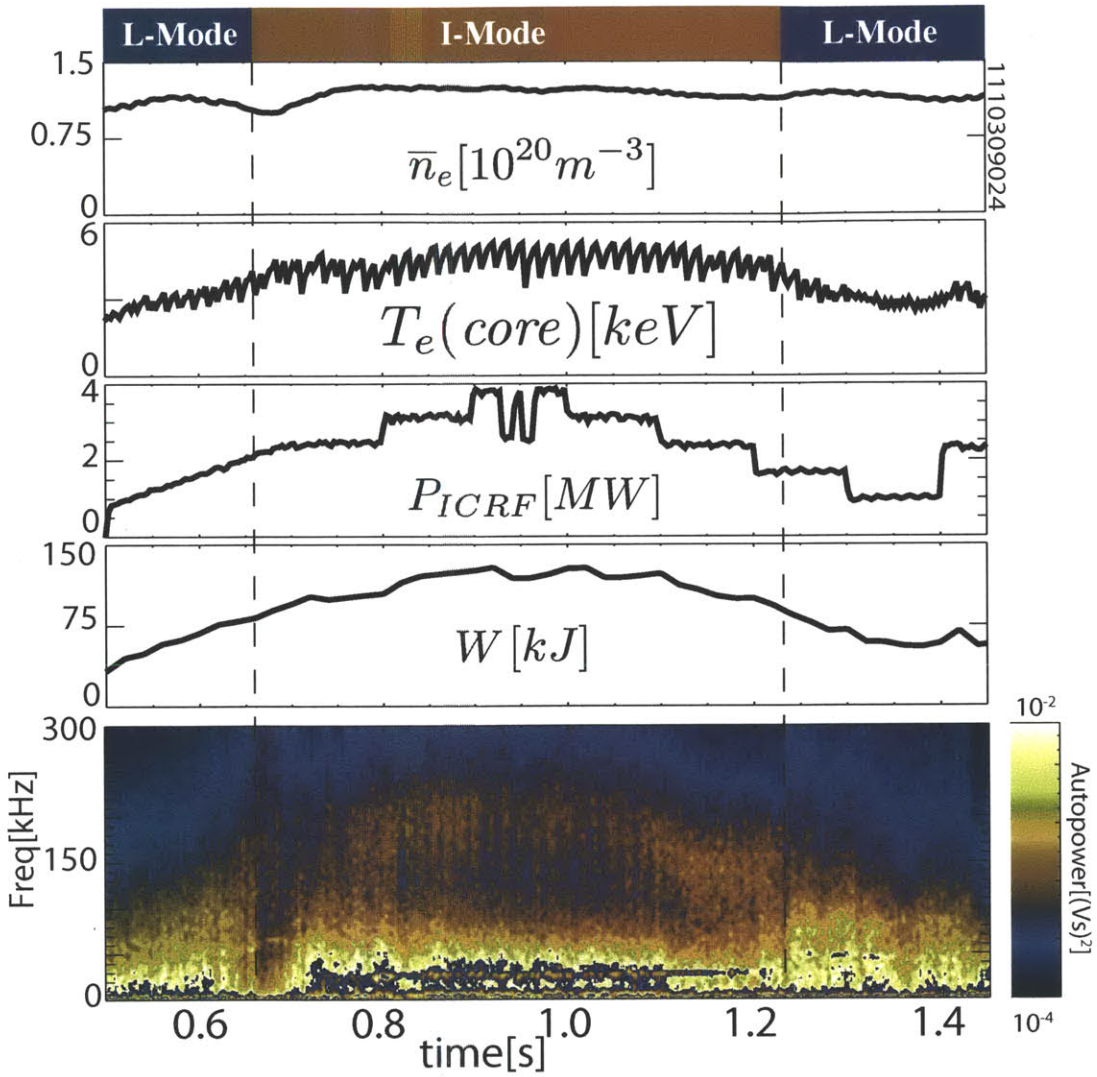

Figure 5-4: Time traces from a discharge used in the present study. The plasma current for this shot is maintained at $I_p = 1MA$ throughout the flattop, while the P_{ICRF} is changed in a stepwise manner in order to change the stored energy and edge temperature gradients during the I-mode phase. The autospectrum of the 75GHz reflectometry channel is shown; the time varying WCM is clearly observed ($f_{cent} \approx 150kHz$ to $250kHz$).

were $\sim 0.7 \times 10^{20} m^{-3}$ and $\sim 1 \times 10^{20} m^{-3}$, which led to the 75GHz and the 87.5GHz reflectometry channels reflecting from the WCM region, respectively. These were, therefore, the channels used to analyze the WCM at those two currents.

The magnetic topology chosen for the experiment was the reverse I_p and B_ϕ configuration, in LSN, as shown in Figure 3-3c. The main initial reason for using this configuration was the desire to have good T_e and n_e profiles from edge Thomson scattering, needed for the ionization source density estimation (see Section 4.2.1). As seen in Figure 2-16, when in LSN, the edge TS system scattering volumes (near the top of the plasma) are away from the X-point, and can be more easily mapped to the midplane than in the USN configuration.

After initial operation in the reverse field, LSN configuration, it was also found that, for this topology, the P_{ICRF} window of operation in I-mode is significantly larger than for normal field, USN. This is useful for scanning a wide range of P_{tot}, on which the WCM characteristics depend.

5.3 Additional comments on data analysis

There were several data analysis caveats and precautions that had to be taken to properly analyze the data in order to maintain the assumptions outlined in the previous sections. These reduce the available data for the analysis significantly.

5.3.1 Time resolution of data measurements

The relevant time resolutions for the data used in this experiment were:

- 1ms time windows were used for each autopower spectrum computed to determine the I_{WCM}
- 5kHz acquisition rate, therefore a 0.2ms time resolution, for the acquisition of the brightness profiles from the visible spectrum camera, hence the $D\alpha$ emissivity profiles used.

- 16.7ms time step between TS measurements, needed for the ionization source measurement.

The coarsest time step in the data acquisition is that of the Thomson scattering, hence, all data are averaged around each TS measurement. This is done, as opposed to interpolating TS measurements in finer time steps to avoid adding data points which are not independent of each other. This is a necessary precaution when dealing with the quantification of the correlation between Γ_{LCFS} and I_{WCM}, as will be discussed later in this section.

5.3.2 External gas puffing

For several shots, there are time intervals within the I-mode phase during which there is external gas puffing into the plasma at discrete poloidal and toroidal locations. As discussed earlier in this section, these are required in order to keep the average density of the plasma constant enough to use the same reflectometry channel to study the WCM.

In Figure 5-5, full time traces of one of the 1MA discharges used in the experiments is shown, including the autospectra of the WCM, extracted from the 75GHz reflectometer channel. The black points are the source term, $\int_{\Delta r} S_{obs} dr$, as a function of time through the shot. The external gas puffing, shown in red, injects D_2 into the vessel from the outboard midplane at B-port, which is located 36° toroidally away from A-port, where the reflectometer is located. The camera line brightness measurements pass in front of B-port, as shown in Figure 4-1.

These localized fueling events increase the source term as expected, since the neutral gas becomes ionized in the SOL and, also particularly, inside the LCFS all around the machine, including through the visible camera lines of sight. Note that there is a lag of approximately 50ms (shown in the figure as "τ") between the gas puffing and the changes in the source term measured with the camera.

This localized puffing creates a clear poloidal and toroidal asymmetry in the source density throughout the plasma and, therefore, the assumption made in Chapter 4, that

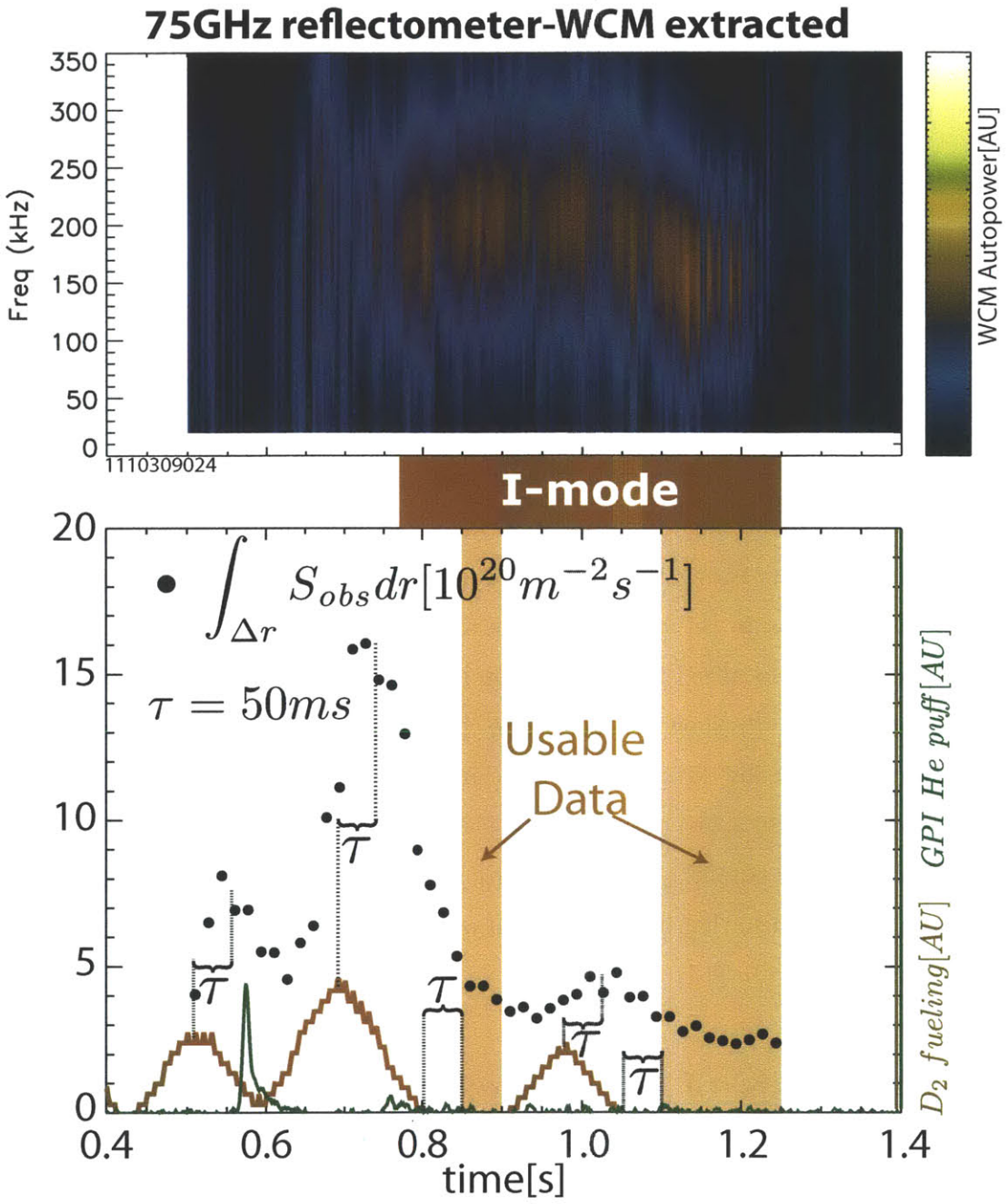

Figure 5-5: Time traces of a 1MA discharge are shown. The top autospectrum is only the Gaussian component extracted using the fitting procedure described in Section 3.5, of the reflectometry signal from the 75GHz channel, which, for the data points used, reflects off of the WCM region. The black points in the bottom plot are the $\int_{\Delta r} S_{obs} dr$ data measured directly from the $D\alpha$ camera, the red trace is the main deuterium fueling and the green is the GPI He puffing. As shown, there is approximately a $\sim 50ms$ lag between the fueling curve and the $\int_{\Delta r} S_{obs} dr$ term, hence, at least a $50ms$ post-puff before the data is used. Note that in cases in which, after $50ms$, there is still a sharp decrease in the $\int_{\Delta r} S_{obs} dr$ signal, the $50ms$ is extended.

the asymmetry factor, σ, remains constant throughout the shot, is broken. Therefore, the time segments during which the gas puff is active, plus 50ms of equilibration time, post-puff , are removed from the analysis. In cases of strong puffing, where it is clear that the $\int_{\Delta r} S_{obs} dr$ measurement is still observing the direct gas puffing effects at 50ms, the post-puff wait time is extended to as long as 70ms.
As shown in Figure 5-5, this results in the exclusion of the I-mode data before $t = 0.85s$ and from $t = 0.9s$ to $t = 1.1s$.

5.3.3 Localized measurements of the WCM

As discussed in Section 5.2, the density must stay constant enough during the analyzed time slices so that the same reflectometry channel detects the WCM throughout. In cases of large density changes, a decrease or increase in the I_{WCM} could otherwise be misinterpreted as an intrinsic change of the mode when, in fact, it could be that the WCM is no longer localized in the reflection layer of a given reflectometry channel.
An example of this was shown earlier in the chapter, in Figure 5-2, where the density increases monotonically during the I-mode, and the WCM, which is observed clearly before approximately 1.35s, decreases in the 87.5GHz channel.
The position of the cutoff layer, deduced from the Thomson scattering diagnostic, is therefore monitored so that it is maintained within the first 2cm of the plasma inside the LCFS ($\sim 0.9 \leq r/a \leq 1$).

5.4 Analysis of the correlation between net outward plasma flux and WCM intensity

5.4.1 Estimation of σ and correlation results

Due to the restrictions described in the previous section, as well as run day difficulties acquiring steady I-modes in the reverse field configuration, the number of shots with enough time slices to make a statistically significant analysis are one for $I_p = 1MA$ and one for $I_p = 1.1MA$.

By using the values $\Gamma_{LCFS}(I) = 0.5 \times 10^{20} m^{-2} s^{-1}$ for 1MA and $\Gamma_{LCFS}(I) = 1.0 \times 10^{20} m^{-2} s^{-1}$ for 1.1MA, the value of sigma can be estimated for each shot by making the assumption that throughout the acquired data window , the average Γ_{LCFS}, given by Equation 4.9, repeated below, is equal to the estimated values respectively (labeled "Γ_{I-H}" from this point on), hence:

$$\Gamma_{I-H} = \overline{\Gamma_{LCFS}} = \overline{\sigma \int_{\Delta r} S_{obs} dr - \frac{V}{A} \frac{d \langle n_e \rangle}{dt}} \tag{5.4}$$

$$\sigma = \frac{\Gamma_{I-H} + \overline{\frac{V}{A} \frac{d\langle n_e \rangle}{dt}}}{\overline{\int_{\Delta r} S_{obs} dr}} \tag{5.5}$$

where the overline refers to the average of the N available time slices for each shot[1]. The resulting σ values for the two currents (from the two shots) are: $\sigma = 0.19$ for the 1MA shot and $\sigma = 0.32$ for the 1.1MA shot. Using these values, the Γ_{LCFS} vs I_{WCM} (normalized to the maximum value within each time series), has been plotted for each one of the shots and is shown in Figure 5-6.

As defined, the σs used in the shots are such that the mean Γ_{LCFS} is equal to Γ_{I-H}. For each shot, the correlation $\rho_{(WCM,\Gamma)}$ between the I_{WCM} and the Γ_{LCFS} is calculated using[111]:

$$\rho_{(WCM,\Gamma)} \equiv \frac{cov_{(WCM,\Gamma)}}{SD_{(WCM)} SD_{(\Gamma)}} \tag{5.6}$$

$$cov_{(WCM,\Gamma)} \equiv \frac{1}{N-1} \sum_{j}^{N} \left[\left(\mathrm{I}_{WCM}(j) - \overline{\mathrm{I}_{WCM}} \right) \left(\Gamma_{LCFS}(j) - \overline{\Gamma_{LCFS}} \right) \right] \tag{5.7}$$

$$SD_{(x)} \equiv \sqrt{\frac{1}{N-1} \sum_{j}^{N} (x(j) - \overline{x})^2} \tag{5.8}$$

where $cov_{(WCM,\Gamma)}$ is the covariance between I_{WCM} and Γ_{LCFS}, and $SD_{(WCM)}$ and $SD_{(\Gamma)}$ are the standard deviations of each variable. $\rho_{(WCM,\Gamma)} = 1$ when there is a perfect correlation between the two variables and $\rho_{(WCM,\Gamma)} = 0$ when there is none.

[1]Not to be confused with *line averaged* for which it was previously used, and only appears when referring to *line averaged density*, $\overline{n}_e$.

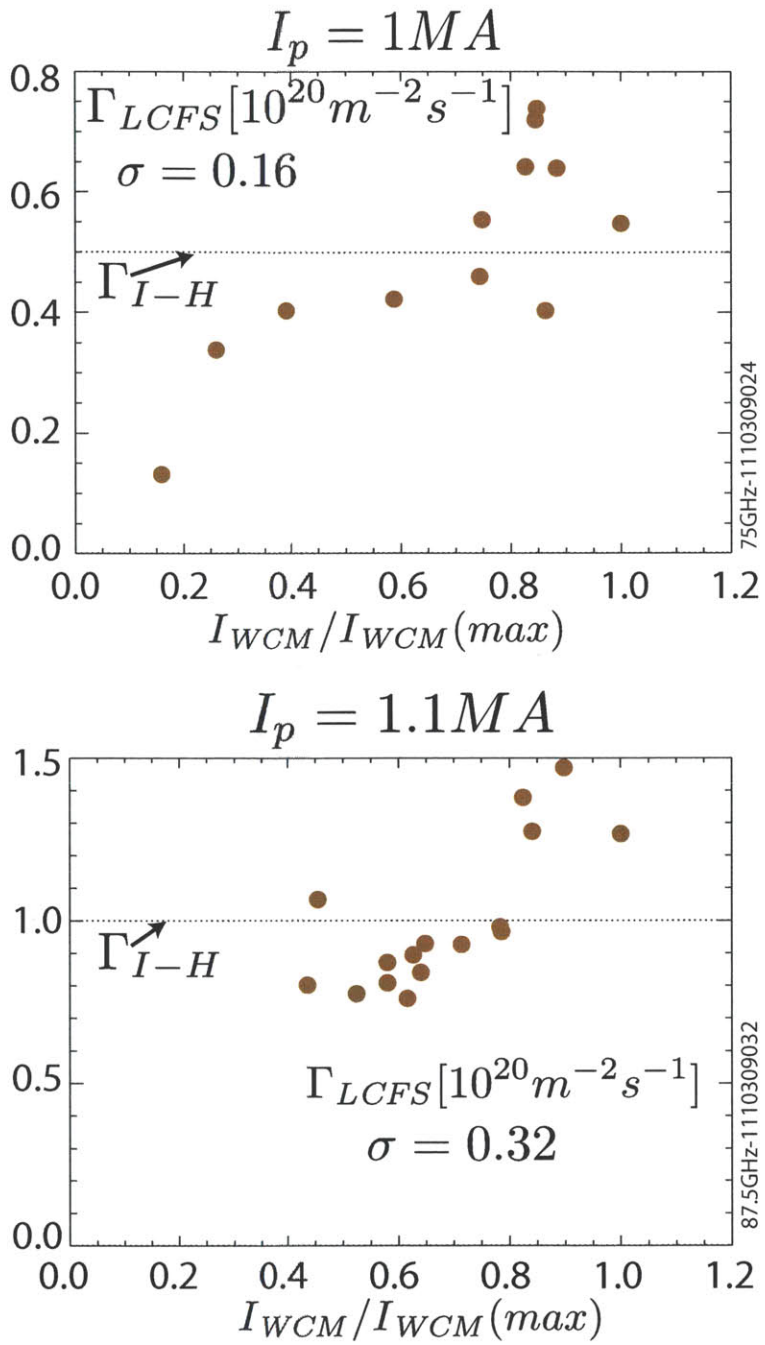

Figure 5-6: The two discharges for which the criteria are satisfied in enough data points to make a statistical argument about the trend, are shown above. The $\Gamma_{I-H} = \overline{\Gamma_{LCFS}}$ constraint is used to deduce a σ value for each current. For 1MA and 1.1MA, the correlation coefficients found between the plotted variables are $\rho_{(WCM,\Gamma)} = 0.81$ and $\rho_{(WCM,\Gamma)} = 0.76$ respectively.

For the two cases, the correlation coefficients are $\rho_{(WCM,\Gamma)} = 0.81$ for 1MA and $\rho_{(WCM,\Gamma)} = 0.76$ for 1.1MA. The significance of this measured correlation can be quantified using a *confidence interval* analysis[111], wherein the null hypothesis is considered, and the acceptance region for a 95% certainty is calculated (this is also known as the 95% confidence interval (C.I.) around the null hypothesis)[2]. For 1MA, if there is NO correlation, there is a 5% chance of obtaining a $\rho_{(WCM,\Gamma)}$ outside the range $-0.57 < \rho_{(WCM,\Gamma)}(0) < 0.57$, whereas for the 1.1MA case, the interval is: $-0.50 < \rho_{(WCM,\Gamma)}(0) < 0.50$. Hence, for both cases, the null hypothesis is rejected, with greater than 95% confidence.

5.4.2 σ dependence of the results

Since the particle flux measurements depend on the asymmetry factor, σ, a valid question to ask is: how sensitive are these results to uncertainty in σ?
Since the estimation of σ comes from the $\Gamma_{LCFS}(I)$ deduced from the I-H transition analysis in Section 5.1 (Γ_{I-H}), a range of possible σs can be used, based on the range of $\Gamma_{LCFS}(I)$ from Tables 5.1 and 5.2. The range of σ deduced from those $\Gamma_{LCFS}(I)$ measurements, using Equation 5.5, is approximately $0.1 < \sigma < 0.5$.

Figure 5-7 shows the same 2 analyzed shots, where the Γ_{LCFS} values at the extremes of this range have been overplotted. Note that the Γ_{LCFS} values have been normalized to the maximum value, in order to show the trends. As observed, the positive correlation is sustained for both cases.

5.4.3 D_2 puffing and data set extension

While the correlation between Γ_{LCFS} and I_{WCM} is clear in the two discharges available, it is desired to extend the data set in order to make a stronger case for the observed behavior. In this section, an approach is described used to estimate particle transport measurements from shots previously omitted from the analysis.

[2]The size of the interval is a function of the sample size N: the more data points there are, the smaller the range for which the null hypothesis is accepted

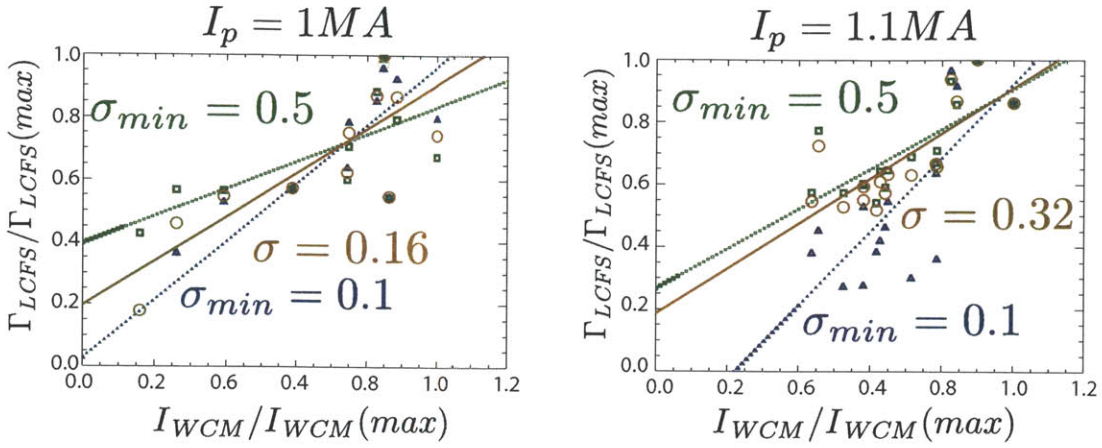

Figure 5-7: Using the maximum and minimum $\Gamma_{LCFS}(I)$ (Γ_{I-H}) from Tables 5.1 and 5.2, the σ range is estimated, to test the robustness of the correlation. As observed, the correlation is sustained for the two extremes. Note that the Γ_{LCFS} axis is normalized to the maximum for each σ used in order to study the trends, independent of the actual magnitude.

Deuterium puffing in the line of sight of the visible camera

Some shots in the experimental run day used small amounts of deuterium puffing within the same lines of sight as the D_α camera for purposes which are outside the scope of this study. The fact that the puffing occurs within the line of sight of the $D\alpha$ camera makes the Abel inversion symmetry assumption invalid.

In order to estimate the particle source term for those shots, it was observed that throughout the day there was a linear response between S_{obs} and the neutral pressure measured at the upper divertor of the tokamak, P_{udiv}. This occurrence is not entirely surprising since the amount of $D\alpha$ light emitted is proportional to the local neutral density[107][112], which is connected to the neutral density in the SOL through the overall neutral particle distribution around the plasma. As changes occur within the neutral "cloud", they communicate through the rest of the neutral distribution at approximately the sound speed (of order ms time scales), hence, changes in the mid-plane neutral density close to the LCFS are correlated with the distribution in the upper divertor[113][108]. Nonetheless, this phenomenon is presented as an empirical observation for this run day and a strict physical model explaining it is not attempted

in the present work.

For each shot using deuterium puffing, the $\int_{\Delta r} S_{obs} dr$ term was estimated using the previous shot with similar plasma parameters, where deuterium puffing was not used, by characterizing the linear relation between $\int_{\Delta r} S_{obs} dr$ and the divertor neutral pressure as: $\int_{\Delta r} S_{obs} dr = a + b(P_{udiv})$. The same parametric fit was then used in the deuterium puffed shot to estimate the $\int_{\Delta r} S_{obs} dr$ of the shots wherein D_2 occurs.

In Figure 5-8, the two shots presented in the previous section for $I_p = 1MA$ and $I_p = 1.1MA$ are shown in the top row. They are labeled by their discharge number "1110309024" and "1110309032", respectively. The black dots are the measured source term ($\int_{\Delta r} S_{obs} dr$) time histories for the shots. As in Figure 5-5, the "usable data" region is labeled and the time traces of D_2 fueling and GPI He puffs are shown. The blue solid line is a time trace of the function: $a + b \times P_{udiv}$, where a and b are fitting parameters, chosen so that the line matches the $\int_{\Delta r} S_{obs} dr$ time trace. While the fit is not perfect, it is clear that the P_{udiv} describes the source term behavior well. For the two He puff cases, the parameters $a_{(24)}, b_{(24)}, a_{(32)}$ and $b_{(32)}$ are determined and then used in D_2 puffed shots to estimate the source term from the P_{udiv} time trace. $a_{(24)}$ and $b_{(24)}$ were used for the 1MA shots, "1110309025" and "1110309026", while $a_{(32)}$ and $b_{(32)}$ were used for the 1.1MA shot, "1110309034".

The general characteristics followed by the $\int_{\Delta r} S_{obs} dr$ term in the He puffed shots, including the strong dependence on the D_2 gas fueling, as well as the $\sim 50ms$ time lag between the fueling and the source term, are seen for all shots. This, plus the fact that the deduced pressure source term in the D_2 shots is within the same approximate range as that of the He puffed shots, suggests that this method is applicable. There is, of course, still an increased level of uncertainty, since there is no direct measurement of the source term for these discharges.

Correlation results from the expanded data set

In Figure 5-9, the Γ_{LCFS} versus I_{WCM} plots for all shots shown in Figure 5-8, including the original He puffed shots shown previously in Figure 5-6, are presented. Whereas, in the He puffed shots, the Γ_{I-H} is a *constraint* from which the σ is deduced (via

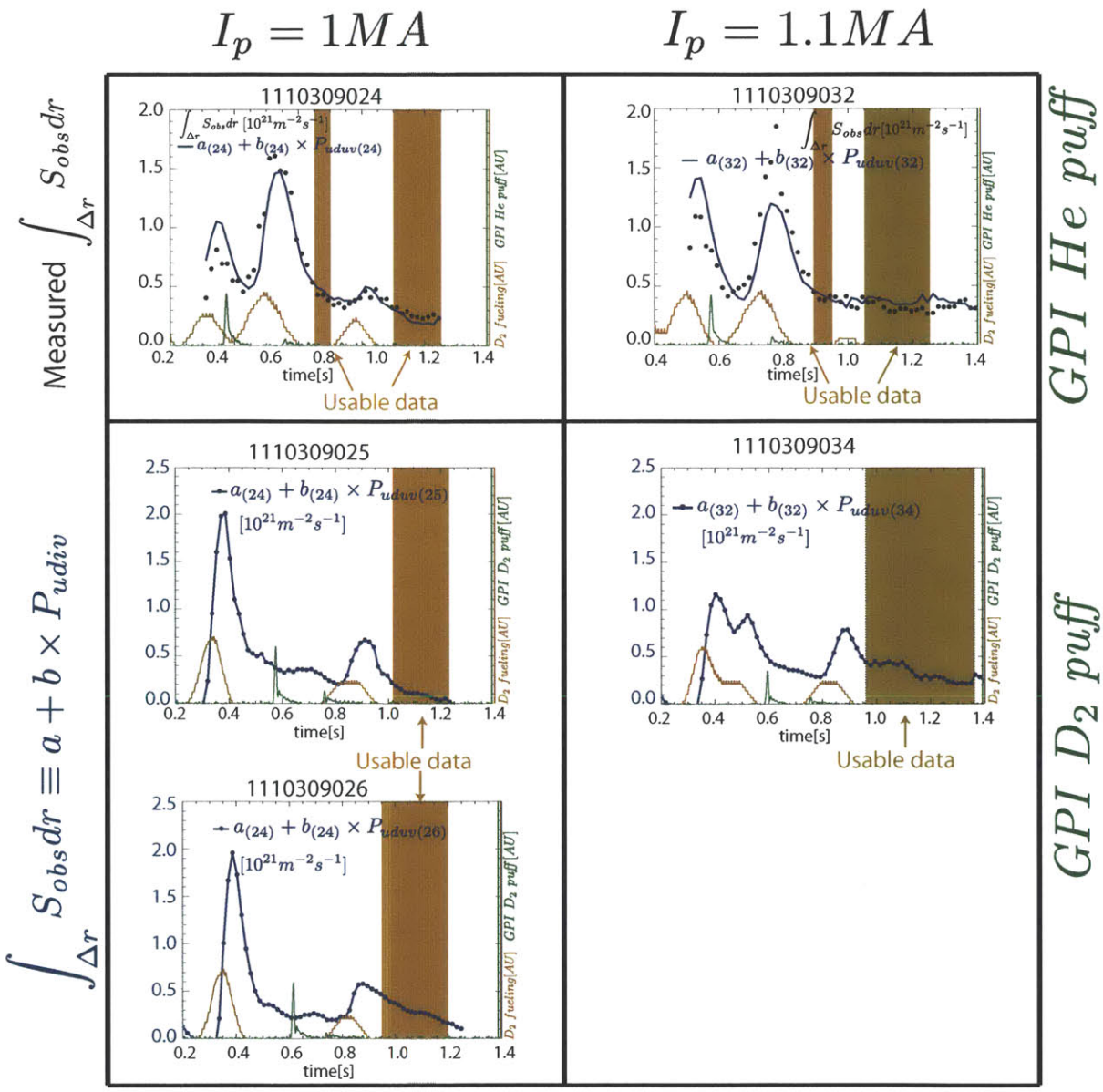

Figure 5-8: The He puffed discharges are suitable for direct measurement of the $\int_{\Delta r} S_{obs} dr$ term, since the requirements for Abel inversion are satisfied. For the top two shots plotted (those with He puffing), the measured source term is shown (black dots). As stated, throughout the run day, an empirical linearity was observed between the measured pressure at the upper diverter, P_{udiv}, and the directly measured source term, $\int_{\Delta r} S_{obs} dr$. Using linear fits between P_{udiv} and $\int_{\Delta r} S_{obs} dr$, for the cases where both are measured (the top two shots), the $\int_{\Delta r} S_{obs} dr$ term is deduced for the D_2 puffed cases.

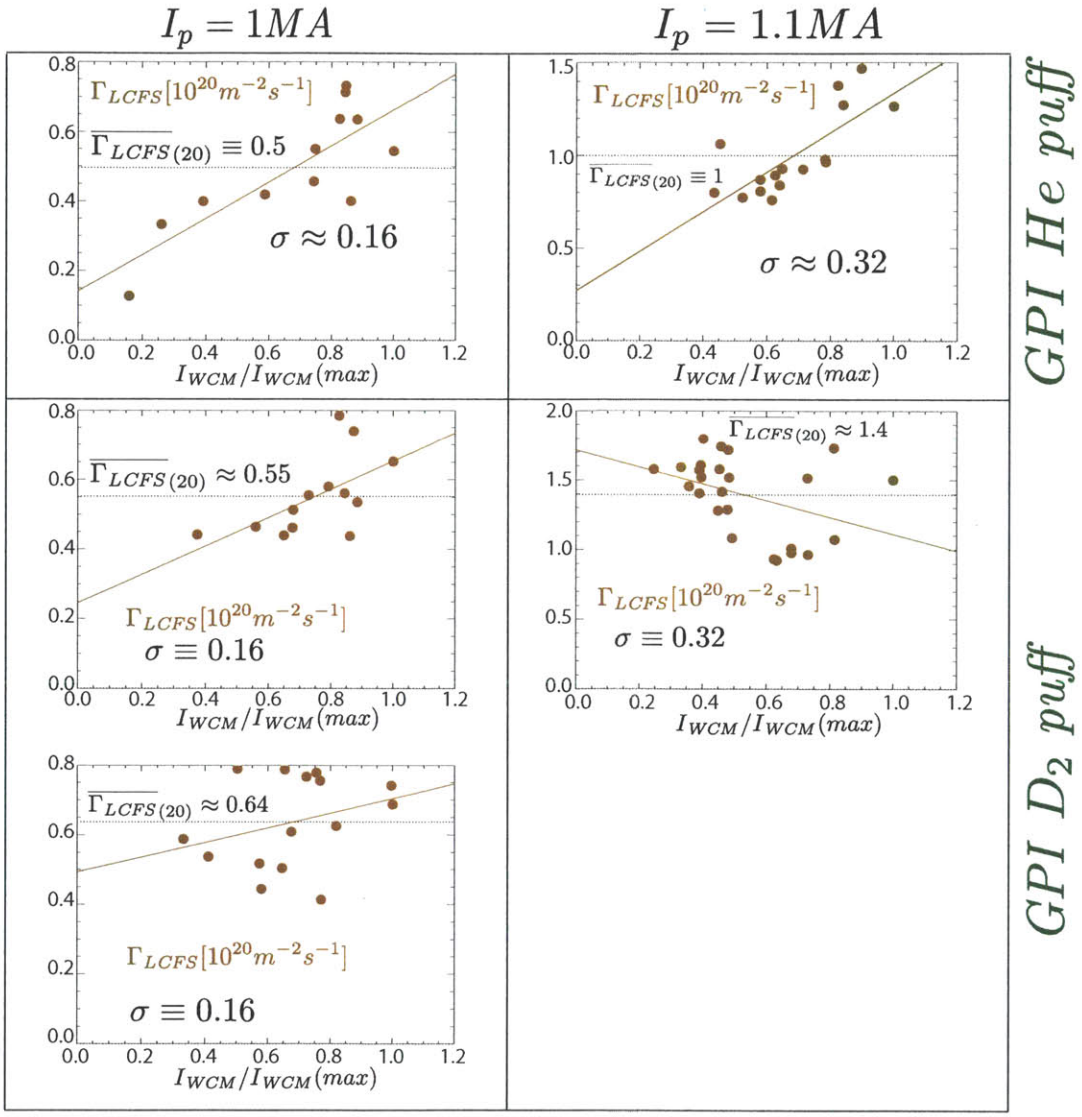

Figure 5-9: Using the $\int_{\Delta r} S_{obs} dr$ deduced from the measured P_{udiv}, the Γ_{LCFS} can be compared to the I_{WCM}. In the He puffed shots, for which the $\int_{\Delta r} S_{obs} dr$ is measured directly, the $\Gamma_{I-H} = \overline{\Gamma_{LCFS}}$ constraint is used to deduce σ, whereas for the D_2 puffed shots, the σ is set from the He case (with equal I_p) and the $\overline{\Gamma_{LCFS}}$ is calculated. For the D_2 puffed shots, the point scatter is much larger than for the He puffed shots, and the correlation is weaker.

Shot	$I_p[MA]$	$\rho_{(WCM,\Gamma)}$	95% C.I. around $\rho_{(WCM,\Gamma)} = 0$	GPI gas puffed
1110309024	1.0	0.81	$-0.57 < \rho_{(WCM,\Gamma)} < 0.57$	He
1110309032	1.1	0.76	$-0.50 < \rho_{(WCM,\Gamma)} < 0.50$	He
1110309025	1.0	0.59	$-0.55 < \rho_{(WCM,\Gamma)} < 0.55$	D_2
1110309026	1.0	0.30	$-0.51 < \rho_{(WCM,\Gamma)} < 0.51$	D_2
1110309034	1.1	-0.39	$-0.40 < \rho_{(WCM,\Gamma)} < 0.40$	D_2

Table 5.3: The shot number, plasma current, correlation coefficient, 95% confidence interval of the null hypothesis and type of GPI gas puffed for all of the shots used in the study, are shown.

Equation 5.5), for the D_2 puffed cases, the σ is held as the constraint ($\sigma = 0.16$ for $I_p = 1MA$ and $\sigma = 0.32$ for $I_p = 1.1MA$), and the average Γ_{LCFS}, $\overline{\Gamma_{LCFS}}$ is computed so as to compare with the H_2 puffed cases (as a sanity check). The values obtained for $\overline{\Gamma_{LCFS}}$ are, in fact, within a factor of 2 of the Γ_{I-H} found from the $I-H$ transition analysis.

As can be observed, the correlation between Γ_{LCFS} and I_{WCM} is weaker for these cases than for the original He puffed shots. The correlation coefficients, as well as the 95% confidence interval of the null hypothesis, for all shots studied, are summarized in Table 5.3.

The conclusions from this study, as well as a discussion of the results, will be presented in the next chapter.

Chapter 6

Discussion, Summary and Future Work

6.1 Discussion of results from Γ_{LCFS} versus I_{WCM} study

6.1.1 The σ factor and its implications

One of the essential qualities of the particle transport model presented in this work, is the attempt to estimate the global, volume integrated particle transport across the LCFS from an inherently local source density measurement. The localized source measurements done with the D_α camera can give an accurate assessment of the ionization source fueling the plasma, but it will not be a complete picture of the ionization dynamics around the whole toroidal shell wherein ionization occurs.

By introducing the asymmetry factor, σ, the source density anisotropies are accounted for, to first order. Inferring the surface area averaged, volume integrated source, $(1/A)\int SdV$, from the local source per unit area measured by the camera, $\int_{\Delta r} S_{obs} dr$, described in Equation 4.8, relies on the assumption that a linear relationship holds between the two quantities. Precautions were made to maintain the validity of this assumption during the experiment, including the exclusion of data from times with

strong gas puffing.

In Section 5.1, the transition between I-mode and H-mode plasmas serves as a point of comparison wherein the magnitude of the global outward particle flux in I-modes, Γ_{LCFS}, can be estimated from a 0 D model, by using measurements from two significantly different regimes: the I-mode, with a small density rise; and the ELM-free H-mode, with very little net outward particle flux. Using the magnitude of the total flux, and the measured ionization at the D_α position, and taking into account the changes in density (which, for the integrated model, can be done by measuring the line average density), the local source measurement ($\int_{\Delta r} S_{obs} dr$) can be compared with the global transport (Γ_{LCFS}) to get an estimate of the poloidal asymmetry factor, σ. For the analyzed cases, σ is substantially smaller than 1. The fact that $\sigma < 1$ implies that the average ionization source density around the periphery of the plasma is lower than the source density measured by the camera at the outboard midplane of the plasma. This result is, perhaps, not so surprising. It has been previously observed on C-Mod[105][103] that main chamber recycling plays a major role in the particle fueling of the main plasma, and, in fact, can dominate over that from recycling in the divertor.

Additionally, there is evidence that, when the LCFS is not close to the inner limiter, the recycling from the outer wall may be larger than from the inner wall, due to ballooning effects of the plasma. The estimated $\sigma = 0.16 - 0.32$, presented in this work, suggests that, at least in the I-mode regime, the ionization at the outer midplane dominates relative to the rest of the poloidal cross section.

Finally, the camera lines of sight are located close to the A-B limiter, and there is expected to be more recycling occurring at the limiters than from the rest of the main chamber PFCs due to their proximity to the main plasma. Therefore, another factor leading to $\sigma < 1$ may be the toroidal location of the camera views near the A-B limiter.

6.1.2 Particle transport and the WCM in the I-mode

One of the main goals in studying the I-mode regime has been to gain an improved understanding of the physics behind the separation of the particle and energy channels. The formation of E_r wells at the edge of the plasma [114][4] may account for the increase in energy confinement, through the breaking of turbulent eddies by the $v_{E\times B}$ shearing. This is analogous to the mechanism behind H-mode edge barrier formation. To tackle the question of particle confinement, we can draw a parallel between the EDA H-mode and the QCM. In [25], the assessment that there is a causal connection between the transport regulation in the EDA H-mode and the presence of the QCM, is based on the following three points:

- The QCM is always present during the EDA H-mode.
- The QCM is radially localized at the steep gradient region.
- A correlation is observed between the amplitude of the QCM and the effective diffusivity, D_{eff} (as shown in Section 3.4.7, Figure 3-20b).

How does the analogy between the QCM/EDA H-mode and the WCM/I-mode hold up based in these criteria? With the exception of a few low I_p cases which will be discussed in the next section, the WCM is a signature of the I-mode, present in the overwhelming majority of I-mode cases. The radial localization measurements from the reflectometer, GPI and ECE diagnostics, show that the WCM lives within the steep temperature gradient region. This is consistent with a mode that is helping to regulate the particle transport in the edge region.

The final criterion is the observed correlation between the mode and the transport. The study presented here is the first quantitative work focused on measuring this correlation. Due to the need to ensure that various assumptions and measurement constraints are satisfied, including those for, I_{WCM}, the T_e and n_e profiles, etc., the amount of experimental data for analysis is limited. Nevertheless, there is clear correlation between the Γ_{LCFS} and the I_{WCM} for the cases where the $\int_{\Delta r} S_{obs} dr$ term is measured directly. There is also somewhat weaker, yet still statistically significant,

evidence that the correlation is also observed in the 1MA cases where the $\int_{\Delta r} S_{obs} dr$ measurement was indirectly measured.

At this point, and with the available data, we conclude there is a direct correlation between the particle transport and the WCM. However, there is a strong argument for additional measurements to strengthen the correlation, or to refute it. This will be discussed further in Section 6.3.

The WCM, therefore, satisfies the three causality criteria as applied to particle transport regulation in I-mode.

Empirically, particularly in the high I_p cases, where the WCM is strongly coherent, and the broadband reduction in fluctuations is stronger (as in the case shown in Figure 5-1), the only observed change in density fluctuations following I-H transitions is suppression of the WCM. Therefore, the presence of the WCM is the only observed phenomenon that can be responsible for the higher particle flux across the LCFS ($\Gamma_{LCFS} = 1.4 \times 10^{20} m^{-2} s^{-1}$ in the example shown) which is suppressed in the ELM-free H-mode, resulting in particle (and impurity) accumulation.

Direct measurements of particle transport caused by the WCM, however, would require flux averaged phase measurements between the density fluctuations and the fluctuating electric potential, $\langle \tilde{n}\tilde{\varphi} \rangle$. Considering the high temperature of the I-mode pedestal region, which procludes the use of Langmuir probes at the WCM location, direct measurements of $\langle \tilde{n}\tilde{\varphi} \rangle$ in this scenario are currently unattainable with the diagnostics available on C-Mod.

6.1.3 WCM-free I-modes

Recent experiments have found cases where the global characteristics of the I-mode are satisfied (formation of the edge temperature gradient, leading to peaked core temperatures, while maintaining L-mode-like densities) but without the detected presence of the WCM or reduction of broadband fluctuations. These are generally shots with low plasma current ($I_p \leq 800kA$, $q_{95} > 4.5$).

Figure 5-3 provides a possible explanation for this phenomenon: at low I_p, the co-

herence of the WCM decreases substantially, to the point that the width of the mode is well within the broadband. It is possible that the WCM is then diagnostically indistinguishable for these cases.

Another possibility comes from the observed poloidal shift of the peak location of the mode, that has been previously observed by the magnetic coils and PCI (Section 3.3.2). If the peak of the mode has substantially shifted poloidally away from the outboard midplane, then it would not be detected by the edge fluctuation diagnostics, since they are mostly localized at the outboard midplane. PCI is the exception, since its vertical chords are radially localized close to the center of the plasma. PCI doesn't detect the presence of the WCM either, but this is not very conclusive since this diagnostic is generally sensitive to the WCM only in cases where the mode is very strong (high I_p cases).

Ultimately, these could be a completely different type of I-mode, with similar global characteristics but different fluctuation phenomena[115]. This would be analogous to the ELMy and EDA H-mode, which have, broadly speaking, similar global characteristics but different regulation mechanisms.

What is clear is that high current cases have well defined WCM and strong broadband reduction, whereas for the low current cases, even those where the WCM is detected, the broadband is not reduced as strongly. From this perspective, it is possible that for high current cases, the WCM is primarily responsible for supplying the particle transport that keeps the density profiles L-mode-like and the impurity accumulation regulated, but for low current cases, the broadband fluctuations are not substantially suppressed and provide strong particle transport.

6.2 Summary

The work presented in this dissertation has contributed to the study of fluctuations, primarily at the edge of the plasma, as well as to the detection, characterization and understanding of the I-mode and, particularly to the WCM.

6.2.1 Diagnostic upgrades to the reflectometry system

After the initial upgrade of the reflectometry system, it was observed that the edge phenomena, including the QCM, can be much better detected by the use of a baseband fluctuation reflectometry system, as opposed to an AM reflectometer. Based on this assessment, a full baseband reflectometry upgrade was undertaken for the whole set of low frequency reflectometry channels: 50GHz, 60GHz, 75GHz and 110GHz, as well as the implementation, in collaboration with PPPL, of the 140GHz and the variable frequency channels.

This upgrade is a full suite of baseband reflectometry channels spanning the $n_e = [0.3 - 2.43] \times 10^{20} m^{-3}$ density range, which can be (and has been) used to detect edge fluctuation phenomena, including the WCM and QCM, as well as to probe more deeply into the core of L-mode, I-mode and peaked H-mode plasmas.

The data acquisition upgrade, described in Section 2.2.3, has enabled the acquisition of fluctuation data at increased Nyquist frequency (1MHz), for the whole length of the discharges. This has ensured that fluctuating phenomena are not "missed" due to limited time windows or insufficient frequency response.

6.2.2 Detection and characterization of the I-Mode

The measurements of edge fluctuations during I-modes have been critical for detecting and characterizing the regime. While all edge fluctuation diagnostics discussed in Section 2.3 have detected the WCM, the reflectometry system is the most sensitive to it and it is routinely able to detect the mode for cases where it is difficult to detect on other diagnostics.

This sensitivity to the density fluctuation is, in part, provided by the baseband upgrade of the system[5][6][7]. As observed in Figure 2-12, the sensitivity of the $88 \pm 0.5GHz$ baseband channels to the QCM is much stronger that of the 88GHz AM channel. Unlike the QCM, the WCM is typically "hidden" in the broadband, and it can be difficult to isolate. If the sensitivity is reduced by subtracting coherent fluctuations, as is done in the AM system, the detection of the WCM would be greatly

hindered.

The reflectometer has been used to reveal many important properties of edge density fluctuations in I-mode:

- The broadband reduction in fluctuations, especially for high I_p discharges, has been observed and quantified using the reflectometer channels. The reduction correlates well with the effective thermal conductivity at the edge of the plasma[4].

- As discussed in Section 3.3.2, by using the array of fixed reflectometry channels, the radial position of the WCM has been localized to the edge of the plasma, at $\sim 0.9 < r/a < 1$.

- By studying the autospectrum of the signal, it was observed that the central frequency of the WCM varies proportionally to the stored energy and, possibly indirectly, to the plasma current, I_p.

- With the additional spectral information supplied by the GPI, and the E_r well measurements from the charge exchange spectroscopy diagnostic, the phase velocity of the mode in the lab frame is found to be $\sim 8 km/s$, in the electron diamagnetic direction, and, using the estimated values of E_r at the same radial position, the phase velocity in the plasma frame is estimated at $\sim 10 km/s$ in the same direction, with little doppler shift occurring for this mode.

6.2.3 Spectral modeling of edge fluctuations

Faced with the problem of extracting the WCM from the broadband fluctuations in the autopower of the complex signal of the reflectometer, a model has been developed and successfully implemented to fit the fluctuations as a composite of 2 independent exponential decays, representing the broadband fluctuations, plus one Gaussian component, representing the WCM.

It was shown that this is a robust model, that describes the I-mode fluctuations as well as the L-mode and H-mode autopower signals.

With this tool, the WCM component has been extracted from the broadband fluctuations and the spectrally integrated autopower amplitude of the mode (I_{WCM}) has been used during to quantify the WCM strength in I-mode discharges.

6.2.4 Particle transport model

A model has been proposed which extends the local particle continuity equation to an integrated equation bounded by the LCFS of the plasma.

This is done by using *wedge-shaped* differential volume elements (Figure 4-3), wherein the individual terms of the continuity equation, the ionization source, the particle flux at the wedge boundaries and the time evolving density, can be clearly identified and treated. The differential elements are then volume integrated, and the flux across the full LCFS is characterized.

In order to extend local source measurements to the whole LCFS boundary, it is necessary to incorporate in the model an *asymmetry factor*, σ, which accounts for differences between the locally measured ionization sources and the total, volume averaged source.

6.2.5 Measured asymmetry of the ionization source in the plasma

By analyzing the global particle transport in the I-mode and ELM-free H-mode regimes, the net outward particle transport across the LCFS in I-mode has been estimated to be:

- $\Gamma_{I-H} = 0.5 \times 10^{20} m^{-2} s^{-1}$ for $I_p = 1MA$ discharges.
- $\Gamma_{I-H} = 1.0 \times 10^{20} m^{-2} s^{-1}$ for $I_p = 1.1MA$ discharges.

By using the constraint, $\Gamma_{I-H} = \overline{\Gamma_{LCFS}}$, for a set of reverse field, LSN I-mode discharges, the asymmetry factors (σ, as defined in Equation 4.8) have been estimated to be:

- $\sigma \approx 0.16$ for $I_p = 1MA$.

- $\sigma \approx 0.32$ for $I_p = 1.1MA$.

By using the whole range of Γ_{I-H} deduced from the I-H transitions, a reasonable expected range of the asymmetry factor is: $0.1 < \sigma < 0.5$.
This implies an asymmetry in the ionization source density, with the measured source density at the outboard midplane being higher than the average source along the LCFS of the plasma.

6.2.6 Positive correlation between Γ_{LCFS} and I_{WCM}

For a set of I-mode discharges in reverse field, LSN magnetic configuration, the intensity of the WCM (I_{WCM}) has been compared to the net outward particle flux across the LCFS of I-mode plasmas (Γ_{LCFS}). The results from the correlation analysis of these data are summarized in Table 5.3.
From the data set, a positive correlation between the two variables has been observed, and is strongest for the cases in which the particle source term, $\int_{\Delta r} S_{obs} dr$, has been directly measured. While the relatively small data set suggests an extension of the work to include more discharges, the present work shows positive correlation between the WCM intensity and net outward particle flux.
Excluding the WCM-free, low I_p, I-modes discussed in Section 6.1.3, the three criteria implying a causal connection are satisfied:

1. The WCM is always present during the I-mode.
2. The WCM is radially localized at the steep temperature gradient region.
3. A correlation is observed between the intensity of the WCM (I_{WCM}) and the net outward particle transport (Γ_{LCFS}).

6.3 Future work

The results of this study can, and should, be extended. In this section, a number of possible directions for future work are described.

6.3.1 Variable frequency channel for $f = 60GHz - 112GHz$

A suggested upgrade to the current reflectometry system involves the installation of a variable frequency channel operating in the 60GHz-112GHz range, a range which spans the channels which have observed the WCM, and which could be used for a variety of purposes, including the study of I-mode plasmas:

- Within steady I-modes, a frequency scan can help better establish the radial position of the WCM, and the locations the broadband fluctuations are reduced.

- By using the 60GHz, 75GHz, 87.5GHz, 88.5GHz and 112GHz channels, in conjunction with the variable frequency channel, the radial correlation length of the WCM could be measured. The radial correlation lengths are proportional to the radial width of the turbulent eddies discussed in Section A.2. A measurement of their radial extent could shine light on the physics behind the WCM[49].

- In the experiment described in Section 5.2, steady density throughout the I-mode was required in order to maintain the radial position of the WCM within the cutoff location of a single reflectometry channel. If a variable frequency channel is varied in conjunction with the rise of the density (probably requiring active feedback), the same channel could be observing the evolution of the WCM during the density rise. This would open the space of operation significantly for analyses similar to those done in the present work.

6.3.2 Expansion of the spectral model

One of the major contributions of this work is the spectral decomposition model presented in Section 3.5.

While the model has, up to now, been used exclusively for the study of the complex reflectometry signal, its use could be extended for other reflectometry signals, such as the homodyne signal, and to other diagnostics.

One possible use is the analysis of GPI spectra, for both the temporal frequency and the spatial wavenumber spectra. This could be used to better characterize the

frequency as well as the wavenumber characteristics of the WCM.

Finally, even though the QCM signal is typically well above the broadband level, the same spectral modeling could be used to characterize and automate the analysis of the QCM and expand on the already comprehensive study of the QCM and its role in EDA H-Mode.

6.3.3 Constraints on the particle transport model

For this study, we have used ionization source measurements in a specific region near the outboard midplane, as a proxy for the ionization source throughout the whole plasma, with weighting by a derived asymmetry factor (σ).

The use of additional spatially distributed measurements (from D_α arrays or others), especially to incude the inboard midplane and the upper and lower divertors, could impose constraints on the model presented.

6.3.4 Extension of the data set

In this study, the restrictions imposed on the experimental setup, as well as on the data analysis, as described in Section 5.2, led to a relative dearth of shots for the analysis.

Two of the lessons learned from this work are that: it is desirable to minimize D_2 puffing both for fueling as well as for GPI, and to expand the data set. Since the correlation hypothesis is a statistical one, confidence in the results should also improve with additional data.

6.3.5 Advantages of other diagnostics for the study of the WCM

While this work focuses heavily on the use of reflectometry for the analysis of the WCM, all edge fluctuation diagnostics have observed it. These diagnostics each have their respective advantages which can be used to better understand the WCM.

GPI

There are several advantages to using GPI for further study of the relationship between the WCM and the particle transport in I-mode:

- The GPI lines of sight are very similar to those of the visible camera. Thus, the measurements of the WCM fluctuations are localized close to those of the ionization source.

- The relationship between the density and temperature and the brightness detected by the GPI is well quantified and characterized. Hence, a direct measurement of the density fluctuation, $\tilde{n}_e/n_e$, can be directly obtained from the brightness signals. This is in contrast with the case of reflectometry, where the $\tilde{n}_e/n_e$ quantification cannot be done directly. By using the GPI capability, direct relationships between the amplitude of the density fluctuations and the particle transport might be obtained.

- The detection of the WCM with the GPI, unlike with reflectometry, does not depend on maintaining constant density during the I-mode, as a result, the density restrictions on the experiment could be relaxed if the GPI were used to characterize the WCM in a particle transport study. For example, I-mode discharges could be produced in which D_2 fueling during the I-mode need not be used.

- A proposed GPI upgrade[116], would consist of the installation of a GPI array, similar to the existing one, at the inboard side of the plasma, close to the midplane. This upgrade would improve the coverage of edge fluctuations, particularly in a region where there is currently a lack of fluctuation diagnostics on C-Mod (other than Langmuir probes which can't access $r/a < 1$ in I-mode). While there is evidence of the ballooning nature of the WCM, particularly the strong presence of the mode on reflectometry and GPI, this array could discover an inboard component of the mode (currently undetected) and could be used

to detect WCM poloidal variations.

Correlation electron cyclotron emission diagnostic

A recent upgrade to Alcator C-Mod was the design and installation of a correlation ECE system[117]. The system's lines of sight have a small spot size determined by an in-vessel mirror which has been set to observe near the plasma edge ($0.75 \leq r/a \leq 1$). The improved temporal and spatial coverage of this system should enable better estimates of the magnitude of the temperature component of the WCM in cases where the optical depth (τ) is large enough that the $\tilde{T}_e$ nature of the fluctuations can be confidently assessed.

In conditions with lower optical depth (τ), this system could also provide additional estimates of the density fluctuation amplitudes, since τ is a known function of density. Nevertheless, these measurements would combine temperature and density fluctuating components, so additional efforts must be made to distinguish between the individual contributions.

Magnetic probes

One of the ways to detect the magnetic fluctuating component of the QCM is through the use of a magnetic pick up coil attached to a fast scanning probe[89]. Through the use of such a probe at the outboard midplane, a magnetic fluctuating component of the QCM at the LCFS was estimated to be $\tilde{B}_\theta \approx 5G$ by measuring an exponentially decaying amplitude of the magnetic fluctuations in the SOL region. Using this probe, the exponential decay length of the QCM was also measured to be $k_r \approx 1.5cm^{-1}$.

This tool has not been used to study the WCM, due to the very high temperatures at the pedestal of the I-mode (typically higher than those of the ohmic EDA H-modes in the previous study) which could easily damage the probes and leave them out of commission.

Nonetheless, there is enough interest in the characterization of the I-mode and the WCM that there are currently plans to proceed with measurements using this probe

in future I-mode runs[108].

6.3.6 Experimental and numerical testing of theoretical models of the WCM

The increasing body of observations regarding the characteristics of the WCM has led to initial proposed physical models to explain it.

One such model is the Heavy Particle mode[100][101] which, as discussed in Section 3.4.6, predicts the impurity ejection from the main plasma, as well as giving an order of magnitude estimate of the density, temperature and magnetic field components of the fluctuations.

Another possible candidate for the mode is the Kinetic Ballooning mode[99], which incorporates many of the qualities that the WCM shares with the QCM, such as its electromagnetic nature and ballooning characteristics, but is present in low collisionality regimes, found at the top of the I-mode pedestal.

One approach at identifying the nature of the WCM would to run controlled experiments focused on the particular dependencies of the modes. For example, an experiment can be proposed in which the type of impurity in the plasma can be varied while maintaining all other variables as constant as possible. A comparison can then be made between the type of injected impurity and the characteristics of the mode, such as its plasma frame velocity and frequency, which depend on the atomic mass of the impurity ion for the Heavy Particle mode[100].

Another approach at identifying the physics behind the WCM is through the use of computational codes that incorporate the relevant physics of the plasma edge of the I-mode. One such code is *BOUT++*[118], which, similar to the original *BOUT*[98], uses 3D fluid equations to simulate linear and non-linear instabilities at the edge of diverted plasmas.

While presently the fluid equations used in *BOUT* can incorporate effects from high collisionality regimes, like that of the EDA H-mode, (which sufficed for the QCM study where the resistive X-point mode was found to be consistent with the charac-

teristics of the mode[93]), kinetic effects are presently not available in the code. There is a planned upgrade to the capabilities of *BOUT++* to include a Gyro-Landau fluid model[119][120] extension of the code which would include kinetic effects which are more relevant to low collisionality conditions, such as those of the I-mode pedestal[1]. When these code upgrades come on-line, currently estimated to be in the spring of 2013[121], it should be possible to conduct a study similar to that done for the QCM, as described in [93], but focused instead on the WCM.

[1]Details can be found in the following URL: https://bout.llnl.gov/html/projects/LDRD/gyro-fluid/gyro-fluid.php

Appendix A

Confinement regimes on Alcator C-Mod

Since its commissioning, several plasma confinement regimes have been observed on the Alcator C-Mod tokamak. In this section I'll describe the history and general characteristics of each regime, including a schematic description of the physics behind each type of confinement.

A.1 Linear ohmic, saturated ohmic and L-Mode confinement

Early studies on Alcator C-Mod sought to recover linear ohmic confinement scaling (LOC) similar to that first observed on Alcator A[24], and later on Alcator C. This regime, observed in ohmic plasmas, is characterized by the linear dependence between energy confinement time, τ_E, and the plasma line average density $\overline{n}_e$. An empirical fit for τ_E taking into account the C-Mod data, was found to be:

$$\tau_E = 0.156\ \overline{n}_e^{0.95} a^{2.1} q_{95}^{1.2} \tag{A.1}$$

where $\overline{n}_e$ is the line averaged density in $10^{20} m^{-3}$, and q_{95} is the safety factor $q = (rB_\phi)/(R_0 B_\theta)$, evaluated at the 95% flux surface, where r is the minor radius and R_0

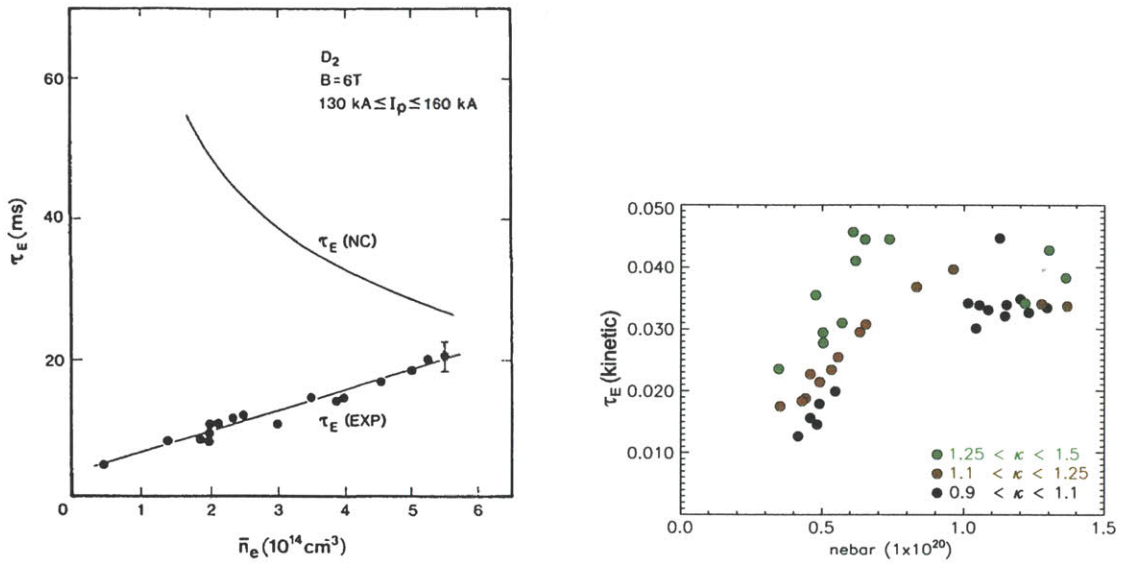

(a) (b)

Figure A-1: a) Alcator A results found a linear dependence between τ_E and $\overline{n}_e$. Which is, both, lower than the expected neoclassical estimates and with opposite density dependence. Figure from [24]. b) First observed on Alcator C and then on Alcator C-Mod, the linear regime was observed to saturate after a $n_e \sim 4/q_{95}$. This Figure is from [25])

the major radius at the center. Shown in Figure A-1a are data from Alcator A showing the linear relationship between the density and the energy confinement time. This is contrary to predictions from neoclassical theory in which the transport is dominated by ion thermal conduction and the thermal conductivity is proportional to the density, hence the confinement time would go as $1/n_e$. This linear confinement is believed to be dominated by anomalous electron transport while ion transport becomes secondary. A multi machine comparison led to the neo-Alcator scaling: $\tau_{Noel} = 0.066\overline{n}_e R^2 \kappa^{0.5} q_{95}$, where κ is the elongation of the plasma[122][24]. The LOC regime was good news for confinement because it would lead to a Lawson's coefficient, $n_e \tau_E \propto n_e^2 R^2 a$, all of which would increase with larger sized, denser machine. Nevertheless, this regime was limited to low τ_E plasmas.

It was seen on Alcator C, and then reproduced on Alcator C-Mod, that, as the density is increased beyond a threshold limit, the linearity begins to break down and the

confinement time saturates with respect to density. Figure A-1b shows results from Alcator C-Mod showing this saturation for different κ ranges. One of the possible explanations of this saturation is believed to be an onset of anomalous ion transport due to increased ion temperature peaking[25]. It was observed on Alcator C that, by using pellet injection, the peaking factor $\eta_i = (n_i \nabla T_i)/(T_i \nabla n_i)$ is reduced and the confinement time recovers the Neo-Alcator LOC scaling. The ohmic regime above the threshold density is called the saturated ohmic confinement regime, or SOC.

Ohmic heating on Alcator C-Mod reaches values of up to $\sim 1MW$, but with the use of auxiliary heating schemes, primary minority ion cyclotron heating, the total input power can reach values of up to $P_{tot} \sim 6MW$. As with other tokamaks[123], in Alcator C-Mod, as the input power is raised from the SOC regime by the auxiliary power, the confinement time is seen to degrade with P_{tot}. The confinement time in C-Mod of this regime, dubbed the L-Mode regime (as in Low confinement regime in comparison to the High confinement regime to be discussed), is well characterized by the inter-machine scaling parameter[124]:

$$\tau_{ITER89}[s] = 0.048 I_p[MA]^{0.85} \kappa^{0.5} R[m]^{1.2} a[m]^{0.3} \overline{n}_e[10^{20} m^{-3}]^{-0.1} M^{0.5} B_T[T]^{0.2} P_{tot}[MW]^{-0.5} \tag{A.2}$$

where M is the main ion mass in amu. Since in equilibrium $P_{loss} = P_{tot}$ and $\tau_E = W/P_{loss}$, the power degradation of τ_E is a consequence of $W \propto P_{tot}^{0.5}$, that is, the plasma energy is less than proportional to the input power. The measured stored energy is well fitted by $W_{ITER89} \equiv \tau_{ITER98} P_{tot}$ as can be observed in Figure A-2.

A.2 The effects of turbulence on transport

One of the main conclusions found in the early years of tokamak research was that the transport is not well predicted by neoclassical theory, which takes into account geometric effects from the toroidal configuration, as observed in Figure A-1a. The presence of turbulence in the plasma was identified as the culprit of the anomalously high energy and particle transport[125].

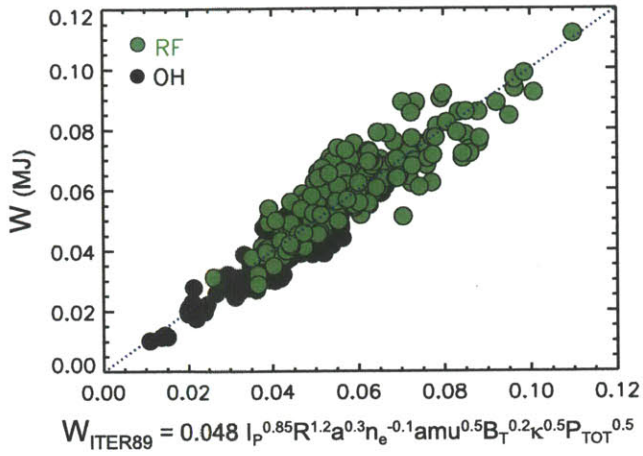

Figure A-2: The SOC regime and the L-Mode regime are well characterized by the ITER89 scaling law wherein the energy confinement time degrades with the input power as $P_{tot}^{-0.5}$ (Figure from [25])

A first approach to understanding the effects of turbulence in the plasma is to simplify the transport to a diffusion process of the form: $\Gamma = D_{eff} \nabla n$, where Γ is the particle flux and D_{eff} is an effective diffusivity. In this picture, the diffusivity $D_{eff} \sim \Delta^2 \nu$, where Δ is a characteristic step size and ν is the frequency at which the particles take the diffusive step. In the classical picture, the radial step size is dominated by the electron gyroradius: $\Delta = \rho_e$, whereas the time between collision is the electron-ion collision time, so $\nu = \nu_{ei}$ since particle transport involves only unlike particle collisions. In toroidal geometries, the transport increases due to the ∇B and curvature drift effects. Neoclassical transport takes these geometric dependencies into account. In neoclassical theory, the step size is determined by the drift away from flux surfaces due to banana orbits: $\Delta \sim \rho_e q (R/r)^{1/2}$ (note the enhancement due to the q and (R/r) factor). The time between collisions from one orbit to another is also reduced since there is a smaller volume in velocity space from which the particles must be removed in order to transition to another orbit: $\tau = \tau_{ei}(r/R) \rightarrow \nu = \nu_{ei}(R/r)$. Since not all particles are trapped[1], an extra $(r/R)^{0.5}$ factor from the trapped fraction must be

[1]Some particles have velocities primarily in the $\hat{b}_{\|}$ direction, hence they experience no magnetic mirror effect that make the particle bounce in the banana orbit

used, leading to:

$$D_{neo-eff} = q^2(R/r)^{2/3}(\rho_e^2\nu_{ei}) = q^2(R/r)^{2/3}D_{class-eff} \tag{A.3}$$

where $D_{class-eff} = \rho_e^2\nu_{ei}$ is the classical effective particle diffusivity. For C-Mod, $q^2(R/r)^{2/3} \approx 4-20$ depending on the safety factor. The effective thermal diffusivity, χ_{eff}, is related to the particle diffusion coefficient as $\chi_{eff} \approx D_{eff}(m_i/m_e)^{0.5}$ (the mass ratio is due to the thermal conduction being dominated by ions since, for the case of energy transfer, like-particle collisions conduct energy, and the dominant scale size is the ion gyroradius), therefore $\tau_E \approx a^2/\chi_{eff} \sim 1/D_{eff} \sim \tau_{ie} \sim 1/n_e$, hence the $1/n_e$ prediction in Figure A-1a.

As temperature and density gradients rise in the plasma, fluctuations are excited due to the free energy from the gradients. The wavenumber of the fluctuations is primarily in the k_θ direction and there are density perturbations associated with them which extend in the poloidal and radial direction for $\Delta \approx \pi/k_\theta$. A simple picture of the effect of these fluctuations on transport can be seen in Figure A-3. As the fluctuations propagate, density accumulation causes charge accumulation described by a Boltzmann response[26], leading to a fluctuating potential: $\delta\phi \sim (T\delta n_e)/(en_e)$, which in turn creates electric fields which create $E \times B$ eddies with $v_{E\times B} = (E \times B)/B^2$, that encircle the density perturbation. These eddies determine the step size and the time for each step. The typical width of these eddies is of order $\Delta \sim \rho_i$. The time between steps is determined by the transit time across the eddy, since, once the particles have migrated, the eddy moves too. This is contrary to what occurs in classical and neoclassical transport where the collisional frequency, not the transit frequency of the particles around the orbits (gyro frequency and bounce frequency respectively) determine the step time. We can assume: $\delta n_e \approx \nabla n/k_\theta = n_e/(k_\theta L_{ne})$ where $L_{ne} = -n_e/\nabla n_e$ since this is the amount of δn_e required to flatten the density profile, hence, removing the local free energy. Defining the eddy time:

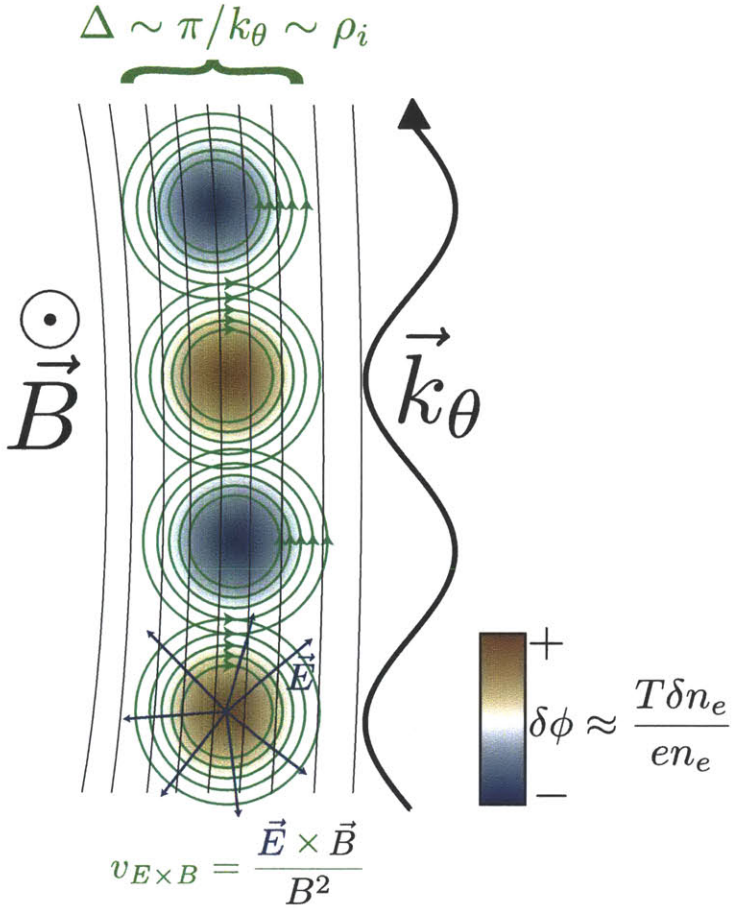

Figure A-3: Turbulent fluctuations in the plasma create potential perturbations that lead to turbulent eddies. These eddies determine the step size and step frequency in an anomalously dominated plasma. A similar figure showing an $E \times B$ eddy forming around a region of charge accumulation in a magnetized plasmas is shown in [26] (Figure 1).

$\tau_{eddy} \equiv \Delta / v_{E\times B}$, we can derive:

$$v_{E\times B} = \frac{E}{B} = \frac{k_\theta \delta\phi}{B} = \frac{k_\theta}{B}\frac{T\delta n_e}{e n_e} = \frac{k_\theta T}{eBk_\theta L_{ne}} = \frac{\rho_i}{L_{ne}} v_{i,th} \tag{A.4}$$

$$\tau_{eddy} = \frac{\Delta}{v_{E\times B}} \sim \frac{\rho_i}{\frac{\rho_i}{L_{ne}} v_{i,th}} = \frac{\lambda_{i,mfp}}{L_{ne}} \tau_{ei} \tag{A.5}$$

where $v_{i,th} = \sqrt{T/m_i}$ is the ion thermal velocity and $\lambda_{i,mfp} = v_{i,th}\tau_{ei}$ is the ion mean free path, that is, the distance it travels before it reaches an electron. For a low collisionality plasma, which is usually the case in tokamaks, the ratio: $\lambda_{i,mfp}/L_{ne} \ll 1$, hence, the confinement is significantly reduced.

While the explanation above is heuristic and a lot of the relevant transport physics is ignored, this description gives an intuitive picture of the problem that arises with turbulence. The turbulent eddies give the plasma a channel for the ejection of particles and energy which decrease confinement, even in cases where the collisionality is low.

A.3 H-Mode regime

The discovery of the high confinement regime, or H-Mode, on the ASDEX tokamak[126] opened a new potential pathway towards fusion. It was observed that, as auxiliary heating was increased beyond a threshold value (approximately 2MW of neutral beam heating in ADSEX), the volume averaged $\beta_\theta = (2\mu_0 nT)/(B_\theta^2)$ is spontaneously increased, leading to a doubling of τ_E. The H-mode has been reproduced in many diverted tokamaks with different types of auxiliary heating, as well as with only ohmic heating. This has led to inter-machine scalings of the threshold power, $P_{Loss} \equiv P_{tot} - dW/dt - P_{fi}$, where P_{fi} is the power lost to fast ions, to transition from L-mode to H-mode:

$$P_{L-H} = 2.15 \overline{n}_e^{0.78} B_\phi^{0.77} a^{0.98} R. \tag{A.6}$$

where $\overline{n}_e$, B_ϕ, a and R are in $10^{20} m^{-3}$, T, m and m respectively. Alcator C-Mod has contributed significantly to this scaling by filling the high density and high magnetic field points.

With few exceptions[127],[128], diverted plasmas are essential for reaching H-mode confinement. It is important to point out that the data set for which P_{L-H} in Equation A.6 is derived is limited to magnetic geometries for which the direction of $v_{\nabla B} = \frac{v_\perp^2}{2\Omega}\frac{\vec{B}\times\nabla B}{B^2}$ is towards the primary X-point in the plasma. For reasons that will be explained in Chapter 3, this configuration is called the *favorable drift direction.* The H-modes are characterized by the formation of pedestals at the edge of the plasma (close to the last closed flux surface, or LCFS), where T_e, T_i, n_e and n_i develop strong spatial gradients, $\nabla T_{i,e}$ and $\nabla n_{i,e}$, as compared to the gradients deeper towards the core of the plasma[129][130].

While the physics of the H-mode and L-H transitions is still a very active area of study, one of the principal theories regarding the transition to the H-mode regime is the turbulence suppression due to sheared flows close to the LCFS. As discussed in the previous section, turbulent-driven transport is believed to be responsible for the increase in particle and energy transport, as compared to neoclassical theory. The diffusive mechanism is dominated by turbulent eddies, as shown in Figure A-3. It has been shown on various tokamaks that, in H-mode, the radial electric field inside the plasma forms a *well* at the edge of the plasma, near the LCFS, as shown in Figure A-4a. The strong gradients in E_r in this region create a $v_{E\times B}$ that changes strongly as a function of radius. This velocity shear poloidaly elongates the turbulent eddies and, ultimately, due to instabilities within the eddies, tears them into smaller ones (See Figure A-4b). The smaller eddies then decrease the $D_{eff} = \Delta^2\nu$ in the region of E_r well. The theories behind the formation of the E_r well focus on the different components of $E_r \approx \frac{1}{en_e}\partial p_e/\partial r - V_{e\theta}B_\phi + V_{e\phi}B_\theta$, and encompass a whole field of tokamak research beyond the scope of this thesis[131][132][114].

Different types of H-modes have been found which maintain the general characteristics of increased particle and energy confinement while differing in specific details, such as its range of operation (e.g. collisionality, q_{95}, etc.), observed fluctuations and quality of confinement. On Alcator C-Mod, H-modes can be divided into three general categories: ELM-free , ELMy and EDA H-modes. Although, as will be discussed, there can be some overlap between them.

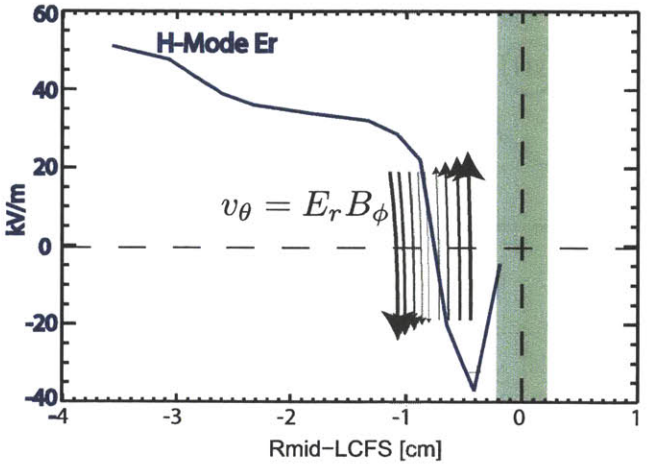

(a)

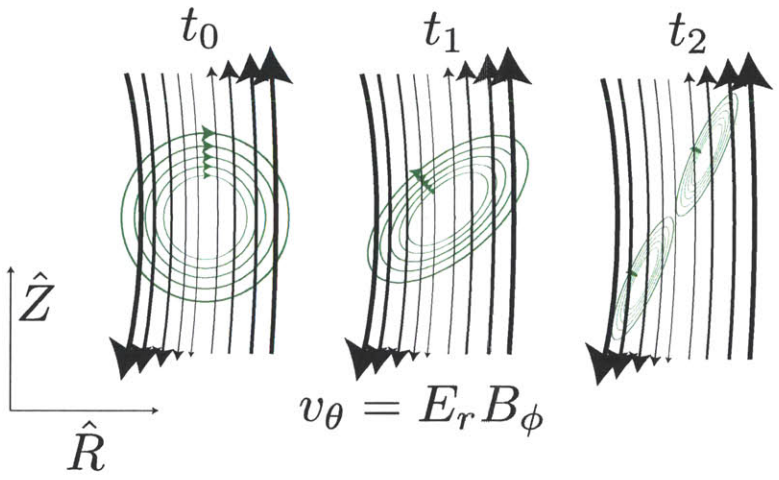

(b)

Figure A-4: a) E_r measurements at the edge of an H-Mode plasma on Alcator C-Mod. H-Modes show radial electric field wells forming close to the region of steep temperature and density gradients. These wells create shears in ExB velocities in the poloidal direction. b) The turbulent eddies which experience this velocity shear are first poloidally elongated (time t_1) and are subsequently torn (time t_2).

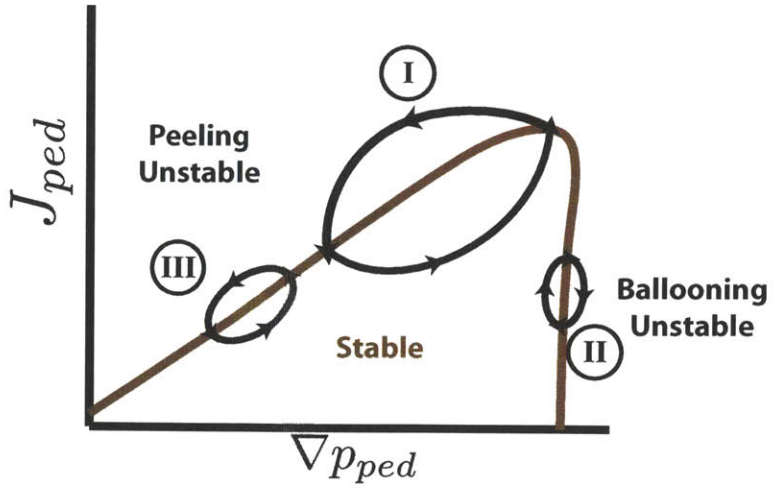

Figure A-5: When the peeling-ballooning modes become unstable, the pedestal is transiently destroyed until it cycles back into the stability region. The relaxation cycles of the three common ELM types are schematically shown in $J_{perd} - \nabla p_{ped}$ phase space. This figure is adapted from [27].

A.3.1 ELMy and ELM-free H-mode

Edge localized modes, or ELMs, have been observed during some H-mode regimes since the discovery of the H-mode on ASDEX[133]. They are typically characterized by strong D_α signals at the edge of the plasma and are categorized by their frequency and strength as well as their proposed relaxation mechanisms: type I ELMs are the strongest and appear when the pedestal pressure and gradient is high, type II ELMs, also known as *grassy* ELMs, have very high frequency but are not very perturbative. Finally, the type III ELMs are typically small amplitude, occur at low pedestal pressure, and are dominated by the pedestal current. These tend to lead to low confinement regimes. ELMs are consistent with the onset of peeling-ballooning and kinetic-balloning type MHD instabilities arising due to the high pressure gradients and pedestal current at the edge of the plasma[27]. The relaxation mechanism of the three common ELM types can be seen in Figure A-5.

On Alcator C-Mod, the first H-modes studied featured high frequency, type III ELMs (at around 1-5kHz). These H-modes had low pedestal temperatures, reaching low energy confinement[134][40].

After these initial H-mode results, boronization was implemented on C-Mod. For this technique, diboron gas is pumped into the chamber during electron cyclotron discharge cleaning, where it adheres to the Molybdenum tiles. This coating strongly reduces the amount of Mo that reaches the core plasma, reducing radiated power. Using this method and increased auxiliary power, the edge temperature of the H-Modes was increased and three new H-mode regimes were accessed: ELM-free, Type II ELMy and EDA H-modes, the latter of which will be discussed in Sections A.3.2 and 3.4.

During the L- to ELM-free H-mode transition, the D_α signal at the edge of the plasma is drastically decreased. In this regime, the confinement, characterized by the $H_{ITER89} \equiv \tau_E/\tau_{ITER89}$ reaches values of up to $H_{ITER89} \approx 2.8$. During the ELM-free H-mode, the core temperature and density grow uncontrollably since there is no *particle flushing* mechanism. This leads to impurity accumulation which, in turn, increases the radiated power and causes H-L back transitions. The ELM-free H-modes are, therefore, intrinsically transient.

At higher edge pressures, the EDA and type II ELMy H-modes appear. The ELMS in the latter regime arise in the upper pressure range of the EDA regime and, as the pressure rises, are sustained beyond the range of the EDA H-mode. Because of the high pedestal pressure during these ELMs and the fast ELM frequency ($\sim 600Hz$), they are well described by the type II ELM model[25]. While their presence is clear on the D_α light, these ELMs have little effect on the plasma density or on the stored energy[135].

By using stronger shaped plasmas, a larger ELM regime is accessed on Alcator C-Mod, as shown in Figure A-6[136][137]. These ELMs appear when operating at high lower triangularity $\delta_L > 0.78$ and low collisionality $\nu* = \nu_{ei}/\nu_{bounce} < 1$. Since the peak pedestal temperature is typically high for these ELMs, they seem to classify as type I ELMs, yet the fact that they appear with an oscillating precursor and that they do not destroy the pedestal during the event suggest that they might classify as a type III. These ELMs reduce the energy at the pedestal by $\sim 15\%$, while being very weakly perturbative to the core, changing it by $< 1\%$.

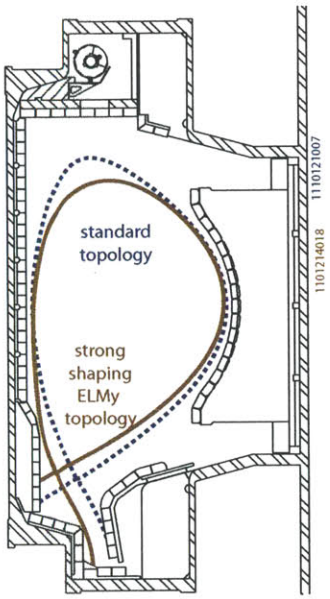

Figure A-6: A typical LSN C-Mod topology is shown in dotted blue. As the lower triangularity is increased and the upper triangularity lowered, a new ELmy regime is accessed.

The lack of long ($> 10\tau_E$) ELM-free H-modes is not surprising due to the high impurity accumulation in this regime. Hence the need of a cleansing mechanism in order to have the possibility of steady state operation. Currently, ITER operation is planned to use type I ELMs for getting rid of impurities, including He ash. A wide tokamak database has been collected in order to predict the Type I ELMy H-mode performance in ITER as well as other future next generation tokamaks. Using this database, a confinement time scaling law for ELMy H modes, analogous to the L-mode one shown in Equation A.2, is derived[138]:

$$\tau_{ITER98(y,2)}[s] = 0.056 I_p[MA]^{0.93} \kappa^{0.78} R[m]^{1.97} \epsilon^{0.58} \overline{n}_e[10^{20} m^{-3}]^{0.41} M^{0.19} B_T[T]^{0.15} P_{tot}[MW]^{-0.69} \tag{A.7}$$

where all the definitions are the same as in Equation A.2, except $\overline{n}_e$ which is in $10^{19} m^{-3}$ and $\epsilon \equiv a/R$. While this is currently the planned regime of operation for future devices, the amount of energy ejected from the plasma during a type I ELM on ITER is expected to be of the order of $70MJ$ within $500\mu s$ which can be detrimental

to the PFCs[139].

A.3.2 EDA H-Mode

On C-Mod, boronization and improved auxiliary heating led to H-modes with higher edge temperature than achieved without these new techniques. By operating at lower current than the ELM-free H-mode regime and with stronger shaping, a new type of H-mode arises, characterized by steady enhanced L-mode level D_α signals, and named The Enhanced D_α or EDA H-mode[134][140][89]. This regime features high energy confinement, up to 90% of the ELM-free τ_E, and is typically accessed at intermediate I_p values, with edge safety factor, $q_{95} > 3.7$ and relatively strong plasma shaping of $\delta > 3.5$ where δ is the average triangularity. The collisionality range of EDA H-Modes tends to be relatively high, $\nu* = \nu_{ei}/\nu_{bounce} > 1$, due to the high density of operation. Typical EDA H-modes last for many energy confinement times ($\geq 10\tau_E$) without the need for ELMs, although, as mentioned before, type II ELMs are routinely observed to coexist in this regime. The EDA regime tends to be within the peeling ballooning mode stability boundary and, as the pressure is raised, the boundary is reached, bringing the onset of the type II ELMs[25].

One of the signatures of the EDA H-mode is the presence of a quasi-coherent mode (QCM) in the 100-150kHz range, as seen in Figure A-7. The QCM is observed as fluctuations of density, electric potential and magnetic fields at the chamber, suggesting the presence of an electromagnetic component, and has been radially localized to the high pressure gradient, edge pedestal region of the plasma. Due to the high collisionality of the EDA pedestal, the QCM is believed to be related to the onset of resistive ballooning mode instabilities[12][93][141]. The QCM has been identified as the main mechanism responsible for controlling the impurity accumulation in the EDA H-mode, allowing sustained operation of the regime[25].

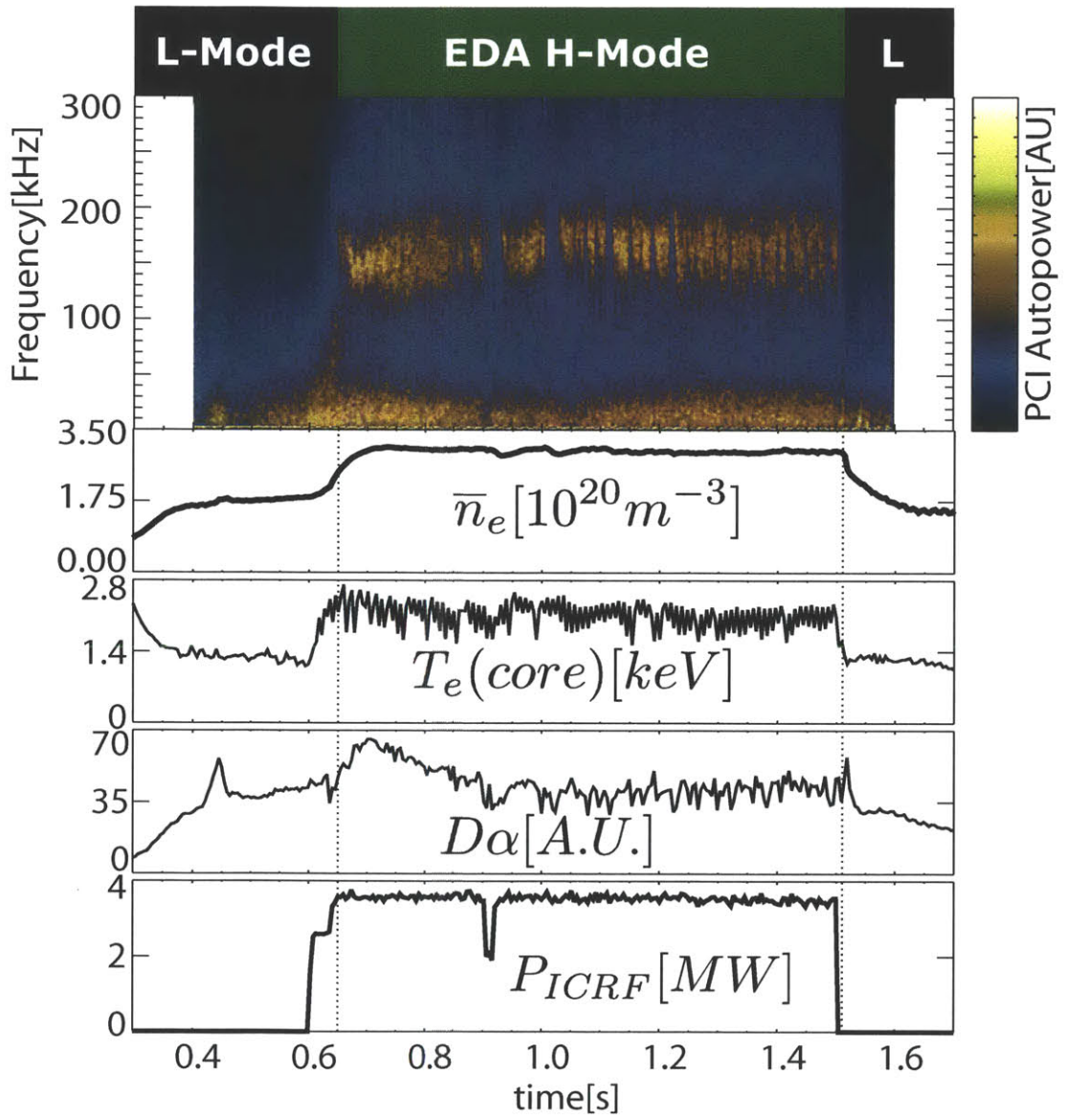

Figure A-7: The EDA H-mode, characterized by the enhanced D_α signal. has high particle and energy confinement and can be sustained for many τ_E. The Quasi-Coherent signature on the density fluctuations is shown, as measured from a phase contrast imaging diagnostic.

Bibliography

[1] A Hubbard and J Hughes and I Bespamyatnov..., Physics of ... (2007).

[2] R. M Mcdermott and B Lipschultz and J. W Hughes and P. J Catto and A. E Hubbard and I. H Hutchinson and R. S Granetz and M Greenwald and B LaBombard and K Marr and M. L Reinke and J. E Rice and D Whyte and ALCATOR C-MOD TEAM, Phys. Plasmas **16** (2009) 056103.

[3] DG Whyte and AE Hubbard and JW Hughes and B Lipschultz and JE Rice and ES Marmar and M Greenwald and I Cziegler and A Dominguez and T Golfinopoulos, Nuclear Fusion **50** (2010) 105005.

[4] AE Hubbard and DG Whyte and RM Churchill and I Cziegler and A Dominguez and T Golfinopoulos and JW Hughes and JE Rice and I Bespamyatnov and M Greenwald, Phys. Plasmas **18** (2011) 056115.

[5] Y Lin and J Irby and P Stek and I Hutchinson and J Snipes and R Nazikian and M McCarthy, Review of Scientific Instruments **70** (1999) 1078.

[6] A Dominguez and NP Basse and J Irby and Y Lin and ES Marmar and G J Kramer, APS-DPP Conference Presenatation (2005) 1.

[7] A Dominguez and I Cziegler and E EDLUND and L LIN and ES Marmar and M Porkolab and J Snipes and G.J Kramer and W.L Rowan, APS-DPP Conference Presenatation (2007).

[8] E Holzhauer and M Hirsch and T Grossmann and B Branas, Plasma Phys. Control. Fusion (1998).

[9] GD Conway, Review of Scientific Instruments **64** (1993) 2782.

[10] G Wang and W.A Peebles and T.L Rhodes and G.J Kramer and E.J Doyle and G.R Mckee and R Nazikian and N.A Crocker and X Nguyen and L Zeng and S Kubota and M.A Vanzeeland, Nucl. Fusion **46** (2006) S708.

[11] T Rhodes and W Peebles and E Doyle and P Pribyl, Plasma Phys. Control. Fusion (1998).

[12] Y Lin and M Institute of Technology, psfc.mit.edu (2001).

[13] J W Hughes, (2006) 1.

[14] Y Ma and J Hughes and D Ernst and Martin Greenwald and John Rice and Yuri Podpaly, APS-DPP Conference Presenatation (2009).

[15] M Greenwald and RL Boivin and F Bombarda and PT Bonoli and CL Fiore and D Garnier and JA Goetz and SN Golovato and MA Graf and RS Granetz, Nucl. Fusion **37** (1997) 793.

[16] F Ryter and W Suttrop and B Brüsehaber..., Plasma physics and ... (1998).

[17] A Loarte and M Becoulet and G Saibene and R Sartori and DJ Campbell and T Eich and A Herrmann and M Laux and W Suttrop and B Alper, Plasma physics and controlled fusion **44** (2002) 1815.

[18] AW Leonard and TH Osborne and JA Boedo and RJ Colchin and ME Fenstermacher and RJ Groebner and M Groth and CJ Lasnier and MA Mahdavi and TW Petrie and PB Snyder and JG Watkins and L Zeng, IAEA Fusion Energy Conference Preceding (2002) 1.

[19] JE Rice and JW Hughes and PH Diamond and Y Kosuga and YA Podpaly and ML Reinke and MJ Greenwald and ÖD Gürcan and TS Hahm and AE Hubbard, Phys. Rev. Lett. **106** (2011) 215001.

[20] D.G Whyte, C-Mod Science Meeting (4/19/2011) (2011) 1.

[21] AE White and P Phillips and DG Whyte and AE Hubbard and C Sung and JW Hughes and A Dominguez and J TERRY and I Cziegler, Nuclear Fusion **51** (2011) 113005.

[22] I Cziegler, MIT Doctoral Thesis (2011) 1.

[23] I Cziegler, Transport Task Force Presentation (2010) 1.

[24] R.R Parker and M Greenwald and SC Luckhardt and ES Marmar and M Porkolab and SM Wolfe, Nuclear Fusion **25** (1985) 1127.

[25] M Greenwald and N Basse and P Bonoli and R Bravenec and E EDLUND and D Ernst and C Fiore and R GRANETZ and A Hubbard and J Hughes, Fusion science and technology **51** (2007) 266.

[26] W Horton, Reviews of Modern Physics **71** (1999) 735.

[27] PB Snyder and HR Wilson and JR Ferron and LL Lao and AW Leonard and TH Osborne and AD Turnbull and D Mossessian and M Murakami and XQ Xu, Phys. Plasmas **9** (2002) 2037.

[28] W.H Zinn, (1955).

[29] M Abdou and D Sze and C Wong and M Sawan and A Ying and NB Morley and S Malang, Fusion Sci. Technol **47** (2005) 475.

[30] J Freidberg, (2007).

[31] J.D Lawson, Proceedings of the Physical Society. Section B **70** (1957) 6.

[32] PH Rebut and RJ Bickerton and BE Keen, Nuclear Fusion **25** (1985) 1011.

[33] D Meade, Nuclear Fusion **50** (2010) 014004.

[34] John D Lindl, (1998).

[35] S Atzeni and J Meyer-Ter-Vehn, (2004).

[36] E Moses, Journal of Physics: Conference Series (2008).

[37] T Boehly and D Brown and R Craxton and R Keck..., ... Communications (1997).

[38] L Spitzer Jr, International Summer Course in Plasma Physics (1960).

[39] I Hutchinson and R Boivin and P Bonoli and C Boswell, iaea.or.at .

[40] Y Takase and R Boivin and F Bombarda..., ... and controlled fusion (1996).

[41] J.L Luxon, Nuclear Fusion **42** (2002) 614.

[42] B Lipschultz and Y Lin and M L Reinke and A Hubbard, Phyiscs of Plasmas **13** (2006) 056117.

[43] G.D Conway, Nucl. Fusion **46** (2006) S665.

[44] T Stix.

[45] C Lau and Greg Hanson and John Wilgen and Yijun Lin and S Wukitch, Review of Scientific Instruments (2010) 10D918.

[46] JJ Sakurai.

[47] Abramowitz, Milton; Stegun, Irene A, Handbook of Mathematical Functions (1965).

[48] IH Hutchinson, Plasma Physics and Controlled Fusion **34** (1992) 1225.

[49] G Kramer and R Nazikian and E Valeo, Review of Scientific Instruments (2003).

[50] RN Bracewell, McGraw Hill (2000).

[51] P Stek, Thesis (PhD). MASSACHUSETTS INSTITUTE OF TECHNOLOGY (1997).

[52] E Mazzucato, Physical Review Letters **36** (1976) 792.

[53] Philip Hartman, (2002).

[54] N Bretz, Physics of Fluids B: Plasma Physics (1992).

[55] T.L Rhodes, Rev. Sci. Instrum. **63** (1992) 4599.

[56] EZ Gusakov and MA Tyntarev, Fusion engineering and design **34** (1997) 501.

[57] Y Lin and R Nazikian and J Irby and E Marmar, PLASMA PHYSICS AND CONTROLLED FUSION (2001).

[58] K Shinohara and K Syun'ichi Shiraiwa and Y Miura, Jpn. J. Appi. Phys. Vol (1997).

[59] B Branas and M Hirsch and J Sanchez and V Zhuravlev, Rev. Sci. Instrum **70** (1999) 1025.

[60] G Conway and J Undertaking, JOINT EUROPEAN TORUS-PUBLICATIONS-JET P (1999).

[61] E Mazzucato and R Nazikian, Phys. Rev. Lett. **71** (1993) 1840.

[62] R Nazikian and G Kramer and E Valeo, Phys. Plasmas (2001).

[63] E Mazzucato, Nucl. Fusion **41** (2001) 203.

[64] M Ignatenko and A Mase and L.G Bruskin and Y Kogi and H Hojo, Nucl. Fusion **46** (2006) S760.

[65] J Irby and M Institute of Technology, iop.org (1992).

[66] EJ Valeo and GJ Kramer and R Nazikian, Plasma physics and controlled fusion **44** (2002) L1.

[67] G J Kramer and R Nazikian and E J Valeo, Plasma Phys. Control. Fusion **46** (2004) 695.

[68] JH Irby and P Stek, Review of Scientific Instruments **61** (1990) 3052.

[69] I.H Hutchinson, **2nd Edition** (2002).

[70] C.A Balanis, (2009).

[71] J Hughes, psfc.mit.edu (2005).

[72] N. P Basse and E. M Edlund and D. R Ernst and C. L Fiore and M Greenwald and A. E Hubbard and J. W Hughes and J. H Irby and L Lin and Y Lin and E. S Marmar and D. A Mossessian and M Porkolab and J. E Rice and J. A Snipes and J. A Stillerman and J. L Terry and S. M Wolfe and S. J Wukitch and K Zhurovich and G. J Kramer and D. R Mikkelsen, Phys. Plasmas **12** (2005) 052512.

[73] A Mazurenko, PhD Thesis (2001).

[74] N Tsujii, PhD Thesis (2012) 1.

[75] T.C Hsu, PhD Thesis (1993) 1.

[76] N.P Basse and A Dominguez and EM Edlund and C.L Fiore and R.S Granetz and A.E Hubbard and J.W Hughes and I.H Hutchinson and J.H Irby and B LaBombard, Fusion science and technology **51** (2007) 476.

[77] JW Heard and C Watts and RF Gandy and PE Phillips and G Cima and R Chatterjee and A Blair and A Hubbard and CW Domier and NC Luhmann, Review of Scientific Instruments **70** (1999) 1011.

[78] J.A Sears, PhD Thesis (2010) 1.

[79] T. Golfinopoulos, Private Communication .

[80] T ASDEX, Nucl. Fusion (1989).

[81] RJ Groebner and TN Carlstrom, Plasma physics and controlled fusion **40** (1998) 673.

[82] AE Hubbard and IO Bespamyatnov and A Dominguez and A Graf and JW Hughes and A Ince-Cushman and B LaBombard and B Lipschultz and L LIN and K Marr and R McDermott and M Porkolab and M L Reinke and J E Rice and W L Rowan and J A SNIPES, 11th IAEA Technical Meeting on H-mode Physics and Transport Barriers (2007) 1.

[83] F Ryter and R McDermott and T Pütterich and J Vicente..., ocs.ciemat.es .

[84] B LaBombard and A Zhukovsky and J Zaks and R Vieira and P Titus and Y Rokman and S Pierson and N Mucic and S Marazita and R Leccacorvi and J Irby and D Gwinn and R Granetz and R Childs and J Bosco and B Beck, M.I.T. Plasma Science and Fusion Center report PSFC/RR-08-6 (2006).

[85] N T Howard and M Greenwald and J E Rice, Rev. Sci. Instrum. **82** (2011) 033512.

[86] E Surrey and A Benn and I Jenkins and M Porton..., Fusion Engineering and ... (2012).

[87] J.E Rice and PT Bonoli and JA Goetz and MJ Greenwald and IH Hutchinson and ES Marmar and M Porkolab and SM Wolfe and SJ Wukitch and CS Chang, Nuclear Fusion **39** (1999) 1175.

[88] D.G. Whyte, Private Communication .

[89] J.A Snipes and B LaBombard and M Greenwald and IH Hutchinson and J Irby and Y Lin and A Mazurenko and M Porkolab, Plasma physics and controlled fusion **43** (2001) L23.

[90] JL Terry and N Basse and MJ Greenwald and O Grulke and JW Hughes and D Mossessian and M Sampsell and B Veto, APS-DPP Conference Presentation (2003) 1.

[91] J Terry and N Basse and I Cziegler and M Greenwald..., Nuclear ... (2005).

[92] A Dominguez and I Cziegler and M Greenwald and N Howard and A E HUBBARD and JW Hughes and E Marmar and M Porkolab and JE Rice and DG Whyte, Transport Task Force Presentation (2010) 1.

[93] A Mazurenko and M Porkolab and D Mossessian and J Snipes, Phys. Rev. Lett. (2002).

[94] BN Rogers and JF Drake and A Zeiler, Physical review letters **81** (1998) 4396.

[95] JR Myra and DA D'Ippolito and XQ Xu and RH Cohen, Phys. Plasmas **7** (2000) 4622.

[96] XQ Xu and R.H Cohen, Contributions to Plasma Physics **38** (1998) 158.

[97] XQ Xu and RH Cohen and TD Rognlien and JR Myra, Phys. Plasmas **7** (2000) 1951.

[98] X Xue-qiao, Plasma Science and Technology **3** (2001) 959.

[99] WM Tang and JW Connor and RJ Hastie, Nuclear Fusion **20** (1980) 1439.

[100] B Coppi and T Zhou, Physics Letters A **375** (2011) 2916.

[101] B Coppi and T Zhou, Phys. Plasmas **19** (2012) 012302.

[102] M Greenwald and R L BOIVIN and R GRANETZ and A Hubbard and B LaBombard and Y Lin and A Mazurenko and D Mossessian and H YUH and W Dorland and B ROGERS, APS-DPP Conference Presenatation (2000) 1.

[103] B LaBombard and M Umansky and R Boivin..., Nuclear ... (2000).

[104] D.W Marquardt, Journal of the society for Industrial and Applied Mathematics **11** (1963) 431.

[105] M.V Umansky and S I Krasheninnikov and B LaBombard and J L Terry, Phyiscs of Plasmas **5** (1998) 3373.

[106] B LaBombard and J Rice and A Hubbard and J Hughes, Nucl. Fusion (2004).

[107] LC Johnson and E Hinnov, Journal of Quantitative Spectroscopy and Radiative Transfer **13** (1973) 333.

[108] B. LaBombard, Private Communication .

[109] M L Reinke and J W Hughes and A Loarte and D Brunner and I H HUTCHINSON and B LaBombard and J Payne and J L Terry, Journal of Nuclear Materials **415** (2011) S340.

[110] M.L. Reinke, Private Communication .

[111] JS Bendat and AG Piersol.

[112] S Zweben and D Manos and R Budny..., Journal of Nuclear ... (1987).

[113] R L BOIVIN and J A Goetz and A E HUBBARD and J W Hughes and I H HUTCHINSON and J H Irby and B LaBombard and E S Marmar and D Mossessian and C S Pitcher and J L Terry and B A Carreras and L W Owen, Phyiscs of Plasmas **7** (2000) 1919.

[114] R.M McDermott, PhD Thesis (2009) 1.

[115] A.E. White, Private Communication .

[116] J.L. Terry, Private Communication .

[117] A White and N Howard and D Mikkelsen..., Plasma Physics and ... (2011).

[118] B.D. Dudson and M.V. Umansky and X.Q. Xu and P.B. Snyder and H.R. Wilson, Computer Physics Communications **180** (2009) 1467 .

[119] RE Waltz and GM Staebler and W Dorland and GW Hammett and M Kotschenreuther and JA Konings, Phys. Plasmas **4** (1997) 2482.

[120] T.Y. Xia, X.Q. Xu et al, 24th IAEA Fusion Energy Conferenve, San Diego, CA (2012).

[121] E.M. Davis, Private Communication .

[122] R Goldston, Plasma Physics and Controlled Fusion (1984).

[123] GH Neilson and EA Lazarus and M Murakami and AJ Wootton and JL Dunlap and SC Bates and JD Bell and CE Bush and PH Edmonds and DP Hutchinson, Nuclear Fusion **23** (1983) 285.

[124] PN Yushmanov and T Takizuka and KS Riedel and O Kardaun and JG Cordey and SM Kaye and DE Post, Nuclear Fusion **30** (1990) 1999.

[125] AJ Wootton and ME Austin and RD Bengtson and JA Boedo and RV Bravenec and DL Brower and JY Chen and G Cima and PH Diamond and RD Durst, Plasma physics and controlled fusion **30** (1988) 1479.

[126] F Wagner and G Becker and K Behringer and D Campbell and A Eberhagen and W Engelhardt and G Fussmann and O Gehre and J Gernhardt and G Gierke, Phys. Rev. Lett. **49** (1982) 1408.

[127] S Sengoku and A Funahashi and M Hasegawa..., Phys. Rev. Lett. (1987).

[128] C Bush and R Goldston and S Scott and E Fredrickson..., Phys. Rev. Lett. (1990).

[129] M Kotschenreuther and W Dorland and M A Beer and G W Hammett, Phyiscs of Plasmas **2** (1995) 2381.

[130] GM Staebler, Plasma physics and controlled fusion **40** (1998) 569.

[131] K C Shaing, Physics of Fluids **31** (1988) 2249.

[132] H Biglari and PH Diamond and PW Terry, Physics of Fluids B Plasma Physics **2** (1990) 1.

[133] DN Hill, Journal of Nuclear Materials **241** (1997) 182.

[134] Y Takase and a R L Boivin and F Bombarda and b P T Bonoli and C Christensen and C Fiore and D Garnier and J A Goetz and S N Golovato and c R Granetz and M Greenwald and S F Horne and A Hubbard and I H HUTCHINSON and J Irby and B LaBombard and B Lipschultz and E Marmar and M May and d A Mazurenko and G McCracken and e P OShea and M Porkolab and J Reardon and J Rice and C Rost and J Schachter and J A SNIPES and P Stek and J Terry and R Watterson and B Welch and S Wolfe, Phys. Plasmas (1997) 1647.

[135] D A Mossessian and P Snyder and A Hubbard and J W Hughes and M Greenwald and B LaBombard and J A SNIPES and S Wolfe and B LaBombard and J A SNIPES and S Wolfe, Phys. Plasmas (2012) 1720.

[136] A Hubbard and K Kamiya and N Oyama..., ... and controlled fusion (2006).

[137] JL Terry and I Cziegler and AE Hubbard and JA Snipes and JW Hughes and MJ Greenwald and B LaBombard and Y Lin and P Phillips and S Wukitch, Journal of Nuclear Materials **363** (2007) 994.

[138] I.P.E.G.C Transport and I.P.E.G.C.M Database and I.P.B Editors, Nuclear Fusion **39** (1999) 2175.

[139] A Herrmann, Plasma physics and controlled fusion **44** (2002) 883.

[140] M Greenwald and R Boivin and P Bonoli and C Fiore and J Goetz and R GRANETZ and A Hubbard and I Hutchinson and J Irby and Y Lin, Plasma physics and controlled fusion **42** (2000) A263.

[141] R Hastie and J Ramos and F Porcelli..., Physics of ... (2003).